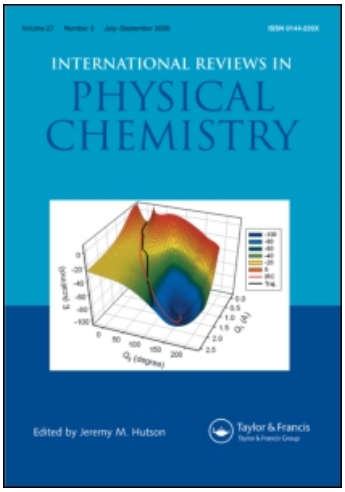

International Reviews in Physical Chemistry
Publication details, including instructions for authors and subscription information:
http://www.informaworld.com/smpp/title~content=t713724383

Coherent multidimensional vibrational spectroscopy

John C. Wright

Online publication date: 26 November 2010

To cite this Article Wright, John C.(2002) 'Coherent multidimensional vibrational spectroscopy', International Reviews in Physical Chemistry, 21: 2, 185 — 255
To link to this Article: DOI: 10.1080/01442350210124506
URL: http://dx.doi.org/10.1080/01442350210124506

INT. REVIEWS IN PHYSICAL CHEMISTRY, 2002
VOL. 21, NO. 2, 185–255

Coherent multidimensional vibrational spectroscopy

JOHN C. WRIGHT†
Department of Chemistry, University of Wisconsin, Madison, WI 53706, USA

Coherent multidimensional vibrational spectroscopy (CMDVS) is an emerging field that offers new oportunities to probe specifically intramolecular and intermolecular interactions in complex samples with the improved resolution and selectivity expected of a multidimensional method. In particular, it provides structural and dynamical information about correlations between modes. It provides this information on the picosecond time scales characteristic of vibrational dephasing. CMDVS is based on the perturbations that are induced in a mode when other coupled modes are excited. It is the vibrational analogue to multidimensional nucler magnetic resonance (NMR). In this review, we present the background that led to the development of CMDVS, a brief summary of the different methods of non-linear laser spectroscopy and how they can achieve CMDVS, the relationships between CMDVS and multidimensional NMR, and the theory necessary to understand the experimental results. The experimental approaches reviewed fall into three main classes: non-degenerate four-wave mixing which is doubly vibrationally enhanced, degenerate four-wave mixing which is triply vibrationally enhanced and six-wave mixing which has three Raman transitions. CMDVS has been implemented in both the time domain and the frequency domain. Finally, the review describes possible extensions of CMDVS and speculates on its future.

Contents

† E-mail: wright@chem.wisc.edu

International Reviews in Physical Chemistry ISSN 0144–235X print/ISSN 1366–591X online © 2002 Taylor & Francis Ltd
http://www.tandf.co.uk/journals
DOI: 10.1080/01442350210124506

1. Introduction

There is great interest in coherent multidimensional vibrational spectroscopy (CMDVS) because it may provide a second revolution for vibrational spectroscopy that would mirror the revolution of multidimensional nuclear magnetic resonance (NMR). There are several primary reasons for the interest. First, CMDVS provides improvements in resolution over one-dimensional (1D) spectroscopy because the information is spread over other spectral dimensions. Second, it provides selectivity because one can selectively enhance spectral features associated with specific modes, components, conformers, isotopomers and subsets of inhomogeneously broadened molecular environments. Most importantly, it provides structural and dynamical information about correlations between modes. Excitation of one vibrational mode will perturb other modes through intra- or intermolecular coupling so cross-peaks will appear in two-dimensional (2D) spectra between the two interacting modes. The cross-peaks therefore reflect the mode correlations and molecular interactions associated with the molecular structure. The selectivity and structural information is obtained as snap-shots on the time scale of vibrational dephasing times, typically picoseconds or less. In this way, it is complementary to NMR methods where structure is averaged over the spin dephasing times of milliseconds.

For this review, CMDVS includes those coherent methods that produce vibrational spectra which are frequency resolved in multiple dimensions. CMDVS is based on non-linear spectroscopy. Non-linear spectroscopy is performed by focusing multiple beams into a sample and observing new beams that emerge from the sample because of non-linear processes [1–4]. Non-linear processes occur when the electric fields of focused electromagnetic waves become large and comparable with the fields within sample molecules. The large fields change the optical properties experienced by other beams that probe the sample. At low intensities, electric fields induce a polarization in the sample molecules that linearly follows the excitation field but, at high intensities, the oscillating polarization acquires distortions. The Fourier

components of the distortion create new fields that radiate from the oscillating non-linear polarization. Thus, $(n+1)$-wave mixing occurs when n electromagnetic waves with frequencies ω_i create a non-linear polarization at $\omega_{out} = \sum_{i=1}^{n} \pm\omega_i$ which in turn launches the $n+1$ wave that is detected. The non-linear process can be envisioned as a coupling between fields that is mediated by matter [5]. From energy conservation, energy flows from the fields having positive signs into the fields having negative signs in the expression $\sum_{i=1}^{n} \pm\omega_i - \omega_{out} = 0$.

Frequency domain non-linear spectroscopy is based on the enhancement of the output beams' intensities when each incoming beam excites an electronic or vibrational resonance. In $(n+1)$-wave mixing, there are n excitation beams and n possible resonances with either electronic or vibrational states. Electronic states generally provide much larger enhancements than vibrational states. The enhancements from each resonance are multiplicative if the resonant states are coupled and additive if they are not. For vibrational spectroscopy, singly vibrationally enhanced (SIVE) processes give 1D spectra and are not capable of CMDVS. Doubly vibrationally enhanced (DOVE) processes have two resonances that provide 2D spectra. Triply vibrationally enhanced (TRIVE) processes have three resonances that provide three-dimensional (3D) spectra. If the fields are not in resonance with a state, the electronic states will dominate the non-linear polarizations because electron clouds are easier to polarize than the nuclear motions [6]. Vibrational contributions can dominate if a vibrational mode is resonant and the electronic states are non-resonant [7, 8].

Time domain non-linear spectroscopy is an equivalent approach and is based on resolving the temporal oscillations of the n coherences created after each excitation pulse [9–12]. It has many advantages including the multiplex advantage, higher signal levels, temporal discrimination against non-resonant electronic backgrounds and temporal selection of a specific coherence pathway.

Symmetry considerations show that even-wave mixing ($n+1$ is even) processes (such as the four-wave mixing (FWM) examples of coherent anti-Stokes Raman spectroscopy (CARS), frequency tripling, stimulated Raman, inverse Raman) occurs in all materials but odd-wave mixing (such as three-wave (TWM) mixing, e.g. second harmonic generation and sum and difference frequency generation) occurs only when inversion symmetry is not present [13–16]. Non-linear surface spectroscopy takes advantage of odd-wave mixing to acquire spectra that have exquisite surface selectivity. Recently, it has also been shown that even-wave mixing methods can also selectively probe chiral materials [17].

In this paper, we first review the background and underlying theory for CMDVS and discuss its relationships with multidimensional NMR. We then apply the theory to the different CMDVS methods to show the similarities and differences. Finally, we explore example applications and speculate on future developments.

2. Background

2.1. *History*

Multidimensional laser spectroscopy has its roots in the Doppler-free [18–22], the laser-induced fluorescence line narrowing [23–32], the hole burning [33–42] and the site selective [28, 29, 32, 43-45] laser spectroscopies of the 1960s and 1970s. Here, specific atoms or molecules were perturbed by laser excitation and the perturbations were monitored by coherent or incoherent probes. The perturbations served as a label of a subset of sample atoms or molecules so those subsets could be probed

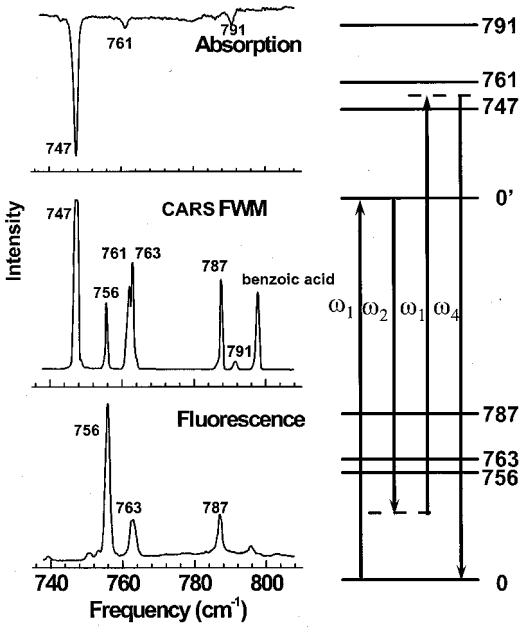

Figure 1. The two-laser doubly resonant CARS FWM spectrum of pentacene in a benzoic acid crystal appear in the centre spectrum. The diagram shows the CARS process when ω_1 is tuned to pentacene's $0 \rightarrow 0'$ electronic transition and ω_2 is tuned so that $\omega_1 - \omega_2$ reaches Raman resonances with the vibrational modes of the ground electronic state or $\omega_1 - \omega_2 + \omega_3$ reaches resonances with the vibronic modes of the excited electronic state. The resonances in the CARS FWM spectrum match the vibronic resonances in the absorption spectrum and the vibrational resonances in the fluorescence spectrum. Reproduced with permission from reference [46].

selectively with high resolution, through either the probe absorption/emission or their intrinsic fluorescence. Although these early methods have been important in research applications, they have not proven practical for widespread routine chemical measurements.

One of the drawbacks to the fluorescence line narrowing and site-selective laser spectroscopies was the lack of sample fluorescence in many materials. Several groups explored the possibility of replacing fluorescence detection with multiresonant non-linear mixing [46–56]. Instead of relying on the spontaneous radiative relaxation of the excited electronic polarization, the output signal was actively created by driving the electronic polarization non-linearly with multiple excitations. Figure 1 shows the first use of FWM for a multiply resonant spectrum [46]. This example represents an electronically resonant CARS spectrum with two lasers, one tuned to an electronic transition (ω_1) and the other (ω_2) scanned to produce a spectrum. The scan shows resonances when $\omega_1 - \omega_2$ matches ground state vibrational modes or $2\omega_1 - \omega_2$ matches excited electronic state's vibronic modes.

The first DOVE multiwave mixing spectrum was a fully resonant three-laser CARS experiment where ω_1 matched an electronic transition, $\omega_1 - \omega_2$ matched a vibrational mode and $\omega_1 - \omega_2 + \omega_3$ matched an excited electronic state vibronic [49–54]. This approach was used to demonstrate site- and component-selective spectroscopy [49–54], line narrowing spectroscopy [57–60] and mode-selective spectroscopy [61–64]. It used the same idea of labelling a subset of the sample molecules by an

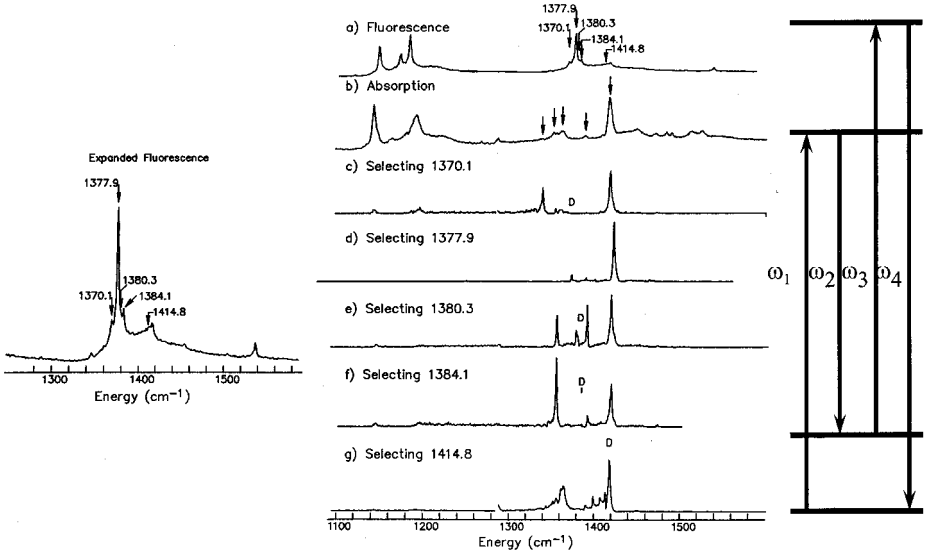

Figure 2. The right side shows a series of three-laser triply resonant CARS FWM spectra ((*c*)–(*g*)) of pentacene in benzoic acid crystal with $\omega_1 - \omega_2$ set to select the different vibrational states seen in the fluorescence spectrum (*a*) while ω_3 scans across the vibronic resonances seen in the absorption spectrum (*b*). Arrows in the absorption spectrum indicate the positions of the peaks seen in the CARS spectra of (*c*)–(*g*). 'D' indicates an artifact that occurs when $\omega_1 = \omega_3$. Reproduced with permission from reference [4].

excitation but now the probing was done by actively driving the output polarization rather than passively watching its radiative relaxation.

The first DOVE experiment to observe cross-peaks between modes is shown in figure 2 [61–64]. Here, ω_1 and $\omega_1 - \omega_2$ were tuned to match an electronic transition and a vibrational mode respectively and ω_3 was scanned so vibronic features appeared in the spectrum when $\omega_1 - \omega_2 + \omega_3$ matched an excited electronic state vibronic state. The cross-peaks are DOVE features that are only observed for modes that are coupled. Thus, vibronic mode cross-peaks only appear at $\omega_1 - \omega_2 + \omega_3$ if the modes are coupled to the ground state mode that is resonant with $\omega_1 - \omega_2$. The absorption spectrum at the top of the figure shows all the vibronic states so comparison of each non-linear spectrum with the absorption spectrum shows how different vibronic modes can be selectively enhanced by establishing resonance with different vibrational states. All the vibrational states are shown in the fluorescence spectrum. Although this approach allowed one to extend high-resolution methods to non-fluorescent systems, spectral selectivity required cryogenic temperatures in order to sharpen the electronic transitions.

In order to eliminate the complications caused by the broadening of electronic transitions, it is desirable to use vibrational transitions. Vibrational transitions have narrow lines at room temperature and provide detailed structural information and molecular fingerprints. There are several experiments that have extended non-linear processes to include vibrational resonances. Sum frequency generation uses SIVE TWM to achieve surface-selective one-dimensional vibrational spectra [13, 65–69]. Fayer and coworkers developed the first vibrationally enhanced photon echo methods to measure vibrational dynamics [70, 71]. These were TRIVE experiments

but they were not designed to provide frequency resolved spectra. LaBuda *et al.* used FWM to measure the size of the vibrational enhancements relative to the non-resonant electronic processes [7, 8]. These SIVE experiments showed that vibrational enhancements could create non-linear polarizations that exceeded the non-resonant electronic contributions so non-linear methods could be used for CMDVS.

The first experiments directed at achieving CMDVS used six-wave mixing (SWM) [72–77]. SWM has five possible vibrational resonances and six transitions. It can be done with six infrared transitions, four infrared transitions and one Raman transition, two infrared transitions and two Raman transitions, or three Raman transitions. All of the experiments have used three Raman transitions to achieve DOVE SWM. The first experiments reported that CMDVS was obscured by two cascaded FWM processes [72]. Later ultrafast time domain experiments reported success in observing SWM with three Raman transitions [73–77]. It was called 2D Raman spectroscopy and Raman echo spectroscopy. However, it became clear that these observations were flawed and cascaded FWM was still obscuring the true SWM process [78, 79]. More recently, it was shown that the true SWM process could be observed by discriminating against the cascaded processes [80–84].

After observing the cascading processes in SWM [72], DOVE FWM experiments were initiated to avoid the complication of cascading [85–89]. Cascading does not affect FWM because any cascading process would require TWM, a process that vanishes in isotropic materials. FWM has three possible vibrational resonances and four transitions. It can be performed with four infrared transitions, two infrared transitions and one Raman transition or two Raman transitions. The previously described fully resonant CARS demonstrated DOVE FWM with two Raman transitions [49–54, 61–64] but this approach was not capable of accessing multiple ground state modes. In order to achieve CMDVS of ground state modes, it is necessary to use infrared lasers. The first demonstration of CMDVS used two infrared transitions and one Raman transition. The two infrared transitions drove two vibrational modes and the double vibrational coherence was probed by the Raman transition [90–92].

Multidimensional laser spectroscopy also has roots in NMR. Shortly after the invention of the laser, it was recognized that the optical analogues to NMR could be created [93, 94]. Free induction decay [95, 96], optical nutation [97] and photon echo [98–101] processes were demonstrated but again they were not practical for routine chemical measurements. A major problem was that the short coherence dephasing times (typically picoseconds) for vibrational and electronic states required either cryogenic temperatures or very low gas pressures to lengthen the dephasing times enough to observe the coherent transients [102, 103]. This problem is overcome if the coherent processes can be implemented on an ultrafast time scale that is short compared with the dephasing time [104, 105].

The first successful experiments to implement the optical analogue to a multi-dimensional COSY NMR spectroscopy were performed by Jonas's group using electronic states [10, 106]. This experiment was based on a heterodyned stimulated photon echo where three ultrafast visible beams created a series of electronic coherences. The final signal from the output coherence was heterodyned with a fourth beam which served as a local oscillator so one could resolve the phase oscillations of the output coherence. The phase oscillations of each excited coherence could be mapped by changing the delay times between each excitation beam. Fourier transformation to the frequency domain then displayed the multidimensional

electronic spectrum. This approach can be directly translated to performing CMDVS by using infrared transitions between vibrational modes.

The first vibrational experiments that used four infrared transitions were done by incoherent pump–probe methods that involved probing excited populations [107]. These experiments provided 2D vibrational spectra by using a strong pump to create vibrational populations that perturb other modes. All modes that are affected by the population changes induced by the pump appear in a probe beam that measures the changes in absorption of the affected modes. Later experiments were able to isolate the coherent portion of the pump–probe experiment by measuring the small temporal modulations that were induced by double vibrational quantum coherences [108]. Fourier transformation of the modulations could then provide the correlation with the absorption changes seen in the probe spectrum.

The first implementation of heterodyne-detected stimulated photon echo to CMDVS was first performed by Hamm *et al.* [11]. This method is a true coherent technique that directly probes the double vibrational quantum coherences. It is the vibrational analogue to a 2D COSY experiment. A single ultrafast excitation beam is divided into four beams that drive a particular vibrational mode. Three beams are used for degenerate FWM to create a signal that is then combined with the fourth beam so the heterodyned signal can be measured. The temporal oscillations of the first and last coherence are measured by scanning the time delays after the first and last coherences were created. 2D spectra are created by Fourier transformation of the two time delays. This technique has been applied in a number of experiments on biologically relevant samples to obtain detailed structural information on femtosecond time scales [11, 12, 109, 110].

2.2. *Theory*

The theory for CMDVS has been developed by a number of groups. There are several excellent references on non-linear spectroscopy [2, 3, 111]. The theory for SWM 2D Raman experiments was first described by Tanimura and Mukamel [112]. DOVE methods were described by Wright *et al.* [87]. Heterodyne-detected FWM and stimulated photon echo processes were described by Cho *et al.* [113]. There has been a great deal more theoretical work in CMDVS (see [84, 114–136]). There is also a recent review of the theoretical aspects of CMDVS [137]. In this review, we present a tutorial that focuses on the theoretical aspects required to understand CMDVS. We start with a phenomenological description of non-linear spectroscopy.

2.2.1. *Phenomenology*

Spectroscopy is based on the relationship between an electromagnetic wave and the induced molecular polarization [2, 3, 111]. Figure 3 shows the relationship between the electric field, $E = \frac{1}{2}[E^0 e^{i(kz-\omega t)} + E^{0*} e^{-i(kz-\omega t)}]$ and the polarization, $P = \frac{1}{2}[P^0 e^{i(k'z-\omega t)} + P^{0*} e^{-i(k'z-\omega t)}]$, of an electromagnetic wave. At low electric fields, there is a linear relationship between the polarization and the electric field but, at higher fields, the relationship becomes non-linear. The electric field is related to the light intensity by

$$I = \frac{cn\xi}{8\pi}(E^0)^2 = \frac{cn\xi}{4\pi}E^2 \tag{1}$$

where n is the refractive index and ξ is a constant that is 1 if E is a classical electromagnetic field but can take on other values for non-classical fields. If the

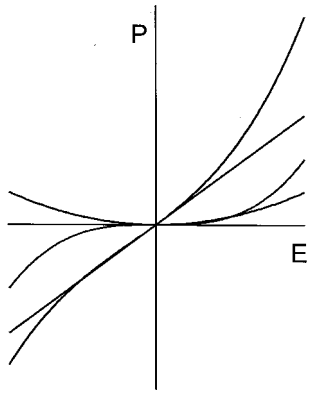

Figure 3. Schematic of the functional dependence of the polarization induced by the electric field of light. The schematic also shows the linear, quadratic and cubic terms that are required to fit the polarization dependence.

intensity is $10^8\,\mathrm{W\,cm^{-2}}$, the electric field magnitude is $2.7 \times 10^5\,\mathrm{volts\,cm^{-1}}$, a value that is nearing dielectric breakdown where electrons are removed from molecules. Since the binding energy of the electrons is changed in these strong fields, it is easy to see why the polarization becomes a non-linear function of the electric field. In the non-linear regime, the polarization is distorted so it acquires new frequency components that radiate light at new frequencies. One expects new frequencies at all the sum and differences that can be formed from all the excitation frequencies.

The position where the polarization's slope in figure 3 becomes vertical is dielectric breakdown so the strongest non-linearities occur at the highest laser intensities. The actual intensity required for sample damage depends on the laser pulse width. Shorter pulses have higher damage thresholds. For nanosecond laser pulses, laser damage becomes important at 10^9–$10^{10}\,\mathrm{W\,cm^{-2}}$ but this damage threshold improves considerably for ultrafast pulses [138].

It is instructive to find the intensities characteristic of different experiments. A focused laser's beam waist has a radius, w_0, given by [139]

$$w_0 = \frac{2\lambda f/\#}{\pi} \tag{2}$$

where $f/\#$ is the focal length/beam size ratio and λ is the light's wavelength. Conventional incoherent sources typically have intensities of $1\,\mathrm{Wcm^{-2}}$ but a 1 W, 1 mm beam continuous wave (CW) laser at 800 nm focused with a 20 mm lens would have a focused intensity of $3 \times 10^5\,\mathrm{W\,cm^{-2}}$. A 100 μJ, 10 ns pulsed laser would focus to a peak intensity of $3 \times 10^9\,\mathrm{W\,cm^{-2}}$ while an ultrafast laser with a 10 μJ, 40 fs pulse would focus to a peak intensity of $8 \times 10^{13}\,\mathrm{W\,cm^{-2}}$. A CW system does not have adequate power to reach the non-linear regime but a pulsed system can reach this regime and beyond quite easily.

The functional dependence of P vs. E is described phenomenologically using a Taylor series expansion:

$$P = \chi^{(1)}E + \chi^{(2)}E^2 + \chi^{(3)}E^3 + \cdots \tag{3}$$

where χ is a tensor called the susceptibility [139]. The contribution from the different terms is shown schematically in figure 3. We suppress the tensor character of χ for

this review but, in fact, the polarization dependence is a powerful probe of molecular structure. $\chi^{(n)}$ corresponds to $(n+1)$-wave mixing with n input fields and an output field. If there are multiple excitation beams, the total electric field is

$$E = \tfrac{1}{2}\{E_1^0 \exp[\mathrm{i}(k_1 z - \omega_1 t)] + E_2^0 \exp[\mathrm{i}(k_2 z - \omega_2 t)] + E_3^0 \exp[\mathrm{i}(k_3 z - \omega_3 t) + \cdots + \text{c.c.}\}. \quad (4)$$

If equation (4) is substituted into equation (3), one obtains a large expression with many direct and cross-terms. An example cross-term for FWM is

$$P^0 = D\chi^{(3)} E_1^0 E_2^0 E_3^0 \quad (5)$$

where D is a factor that accounts for the different electric field permutations in the cross-products. It can take on different values for different conventions of defining χ [111, 140, 141]. For a three-laser experiment $D = 6$ while, for a two-laser experiment where $E_1 = E_2$, $D = 3$.

The surface selectivity of odd-wave mixing spectroscopies is easily understood by realizing that the even terms in equation (3) create symmetric curves on reversing the electric field [142]. For example, the $\chi^{(2)}$ term in equation (4) is represented by the parabola in figure 3 which is clearly symmetric. It adds equally to the polarization regardless of the sign of E. Since P must be an antisymmetric function of E, all even terms must vanish in an isotropic material so one cannot generate even combinations of the excitation frequencies.

2.2.2. *Quantum mechanical theory—coherences*

A more insightful approach uses quantum mechanical coherences [2]. It is first important to understand the concept of a coherence. When an electromagnetic field perturbs a state, ψ_a and mixes it with another state, ψ_b, the wavefunction is a coherence given by

$$\Psi(x,t) = c_a(t)\psi_a(x)\exp(\mathrm{i}\omega_a t) + c_b(t)\psi_b(x)\exp(\mathrm{i}\omega_b t). \quad (6)$$

Since the probability, $\psi\psi^*$ has a cross-term involving $\exp[\mathrm{i}(\omega_b - \omega_a)t]$, the coherence is a time-dependent state that oscillates at a frequency $\omega_b - \omega_a$ and is measured by $\rho_{ba} \equiv c_b c_a^*$. If c_a or c_b is zero, it becomes a stationary state, a population and $\rho_{aa} \equiv c_a c_a^*$ measures the population. If states a and b have a transition dipole moment, μ_{ba}, the oscillating coherence couples with an electromagnetic field and absorbs or emits light, depending on its phase relative to the field. If the quantum system starts in the ground state with $\rho_{aa} = 1$ and it begins to interact with a resonant field, then $c_b = \sin \Omega_{ba} t/2$ and $c_a = \cos \Omega_{ba} t/2$. The coherence evolves as $c_b > 0$: it reaches a maximum when $\Omega_{ba} t = \pi/2$, it becomes an excited state population when $\Omega_{ba} t = \pi$ and it then evolves back to the $\rho_{aa} = 1$ population. Between $\Omega_{ba} t = 0$ and π, the system is absorbing light and between $\Omega_{ba} t = \pi$ and 2π the system is emitting light by stimulated emission. Observationally, one observes alternating dimming and brightening of the excitation beam. This process is called optical nutation and Ω is the angular Rabi frequency. The Rabi frequency is intensity dependent:

$$\Omega_{ba} = \frac{\mu_{ba} E}{2\hbar}. \quad (7)$$

For electronic transitions with a transition dipole moment of 1 debye, conventional sources of $0.01\,\mathrm{W\,cm^2}$ have a linear Rabi frequency of 10^6 Hz, a time scale that is

much longer than electronic relaxation processes. For the previous examples with focused lasers of $3 \times 10^5\,\mathrm{W\,cm^{-2}}$, $3 \times 10^9\,\mathrm{W\,cm^{-2}}$ and $8 \times 10^{13}\,\mathrm{W\,cm^{-2}}$, the Rabi frequencies are 8×10^9, 8×10^{11} and 10^{14} Hz. These frequencies can easily exceed the 10 ns lifetime of many electronic states so optical nutation becomes important. These intensities are the regime of the dynamic Stark effect where saturation and line broadening become important for electronic transitions. For vibrational transitions with a transition moment of 0.03 debye, the Rabi frequencies for similarly focused lasers are 2×10^8, 2×10^{10} and 4×10^{12} Hz. Except for the very highest intensity, these time scales are slower than typical vibrational dynamics so the dynamic Stark effects occur only in the region where samples are damaged. It is therefore common to treat the non-linear mixing processes perturbatively.

Liouville diagrams show the evolution of the coherences and populations when a sample interacts with electromagnetic fields [2]. They are a powerful way to visualize any spectroscopic process because they show how each transition changes the coherences and populations. Consider a steady state coherence described by $\rho_{\alpha\beta}$ as it interacts with an electromagnetic field, beginning at $t = 0$ [4, 87]. The field can induce a transition on either the bra or ket of the coherence, thus changing either state α or state β to a new state γ. The new coherence will be either $\rho_{\gamma\beta}$ or $\rho_{\alpha\gamma}$. If the initial steady state coherence is written as

$$\rho_{\alpha\beta} = \rho^0_{\alpha\beta} \exp\left[\mathrm{i}(k_{\mathrm{lasers}} z - \omega_{\mathrm{laser}} t)\right], \tag{8}$$

the resulting coherence will be either [143]

$$\begin{aligned}
\rho_{\gamma\beta} = \frac{\Omega_{\alpha\gamma}\rho^0_{\alpha\beta}}{2}\Bigg(&\frac{\exp\left\{\mathrm{i}[(k_{\mathrm{lasers}} + k)z - (\omega_{\mathrm{lasers}} + \omega)t]\right\}}{\omega_{\gamma\beta} - (\omega_{\mathrm{lasers}} + \omega) - \mathrm{i}\Gamma_{\gamma\beta}} \\
&+ \frac{\exp\left\{\mathrm{i}[(k_{\mathrm{lasers}} - k)z - (\omega_{\mathrm{lasers}} - \omega)t]\right\}}{\omega_{\gamma\beta} - (\omega_{\mathrm{lasers}} - \omega) - \mathrm{i}\Gamma_{\gamma\beta}} \\
&+ \exp\left(-\Gamma_{\gamma\beta}t\right)\exp\left(-\mathrm{i}\omega_{\gamma\beta}t\right)\Bigg\{-\frac{\exp\left[\mathrm{i}(k_{\mathrm{lasers}} + k)z\right]}{\omega_{\gamma\beta} - (\omega_{\mathrm{lasers}} + \omega) - \mathrm{i}\Gamma_{\gamma\beta}} \\
&- \frac{\exp\left[\mathrm{i}(k_{\mathrm{lasers}} - k)z\right.}{\omega_{\gamma\beta} - (\omega_{\mathrm{lasers}} - \omega) - \mathrm{i}\Gamma_{\gamma\beta}}\Bigg\}\Bigg) \\
&+ \rho_{\gamma\beta}(t = 0)\exp\left(-\Gamma_{\gamma\beta}t\right)\exp\left(-\mathrm{i}\omega_{\gamma\beta}t\right)
\end{aligned} \tag{9}$$

or

$$\begin{aligned}
\rho_{\alpha\gamma} = \frac{\Omega_{\beta\gamma}\rho^0_{\alpha\beta}}{2}\Bigg(&\frac{\exp\left\{\mathrm{i}[(k_{\mathrm{lasers}} + k)z - (\omega_{\mathrm{lasers}} + \omega)t]\right\}}{\omega_{\gamma\alpha} + (\omega_{\mathrm{lasers}} + \omega) + \mathrm{i}\Gamma_{\gamma\beta}} \\
&+ \frac{\exp\left\{\mathrm{i}[(k_{\mathrm{lasers}} - k)z - (\omega_{\mathrm{lasers}} - \omega t)]\right\}}{\omega_{\gamma\alpha} + (\omega_{\mathrm{lasers}} - \omega) + \mathrm{i}\Gamma_{\gamma\beta}} \\
&+ \exp\left(-\Gamma_{\gamma\alpha}t\right)\exp\left(\mathrm{i}\omega_{\gamma\alpha}t\right)\Bigg\{-\frac{\exp\left[\mathrm{i}(k_{\mathrm{lasers}} + k)z\right]}{\omega_{\gamma\alpha} + (\omega_{\mathrm{lasers}} + \omega) + \mathrm{i}\Gamma_{\gamma\alpha}} \\
&- \frac{\exp\left[\mathrm{i}(k_{\mathrm{lasers}} - k)z\right]}{\omega_{\gamma\alpha} + (\omega_{\mathrm{lasers}} - \omega) + \mathrm{i}\Gamma_{\gamma\alpha}}\Bigg\}\Bigg) \\
&+ \rho_{\alpha\gamma}(t = 0)\exp\left(-\Gamma_{\gamma\alpha}t\right)\exp\left(\mathrm{i}\omega_{\gamma\alpha}t\right).
\end{aligned} \tag{10}$$

Here, k_{lasers} and ω_{lasers} are the combinations of excitation wavevectors and frequencies that created the $\rho_{\alpha\beta}$ coherence, and $\omega_{\gamma\beta} \equiv \omega_\gamma - \omega_\beta$ and $\Gamma_{\gamma\beta}$ are the frequency and dephasing rate of the $\rho_{\gamma\beta}$ coherence. These expressions assume weak excitation fields, i.e. $\Omega_{\alpha\gamma} \ll \Gamma_{\gamma\beta}$. The first two terms in each expression are the steady state values of the coherence and the last three terms are the transients. In the rotating wave approximation, two of the first four terms can be neglected depending on whether the denominator $\omega_{\gamma\beta} - (\omega_{\text{lasers}} + \omega)$ or $\omega_{\gamma\beta} - (\omega_{\text{lasers}} - \omega)$ is closer to resonance. These terms can either be resonant or antiresonant.

These expressions show several important characteristics. The coherence's magnitude is controlled by the Rabi frequency in the numerator and the resonance factors in the denominator. Frequency domain spectroscopy uses the resonance enhancement that occurs when the driving frequencies match the molecular transitions. Time domain spectroscopy is based on the oscillations of the transient terms at the molecular coherence's frequency. Note that this frequency is the difference in frequency between the two states in the coherence.

For the special case where $\rho_{\alpha\beta} = \rho_{\alpha\alpha}$ and state γ is more energetic than state α, the steady state resonant terms in equations (9) and (10) are

$$\rho_{\gamma\alpha} = \frac{\Omega_{\alpha\gamma} \exp\left[\mathrm{i}(kz - \omega t)\right] \rho^0_{\alpha\alpha}}{2\Delta_{\gamma\alpha}} \tag{11}$$

and

$$\rho_{\alpha\gamma} = -\frac{\Omega_{\alpha\gamma} \exp\left[\mathrm{i}(kz + \omega t)\right] \rho^0_{\alpha\alpha}}{2\Delta_{\alpha\gamma}} \tag{12}$$

respectively, where $\Delta_{\gamma\alpha} \equiv \omega_{\gamma\alpha} - \omega - \mathrm{i}\Gamma_{\gamma\alpha}$. The $\exp(-\mathrm{i}\omega t)$ factor indicates an absorption transition and the $\exp(\mathrm{i}\omega t)$ factor indicates an emission. The ket side transition is an absorption (equation (11)) and the bra side transition is an emission (equation (12)). For the special case where state γ is less energetic than state α, the two resonant terms are instead

$$\rho_{\gamma\alpha} = \frac{\Omega_{\alpha\gamma} \exp\left[\mathrm{i}(kz + \omega t)\right] \rho^0_{\alpha\alpha}}{2\Delta_{\gamma\alpha}} \tag{13}$$

and

$$\rho_{\alpha\gamma} = -\frac{\Omega_{\alpha\gamma} \exp\left[\mathrm{i}(kz - \omega t)\right] \rho^0_{\alpha\alpha}}{2\Delta_{\alpha\gamma}} \tag{14}$$

respectively, where $\Delta_{\gamma\alpha} \equiv \omega_{\gamma\alpha} + \omega - \mathrm{i}\Gamma_{\gamma\alpha}$. Now the ket side transition is an emission and the bra side transition is an absorption. Notice that the subscripts of the resonant denominator are identical to those of the coherence. Note also that both bra side transitions introduced a negative sign.

These ideas provide some general guidelines for interpreting the frequencies and resonances expected for a coherence pathway in a Liouville diagram [144, 145]. Each coherence in a Liouville diagram is labelled by the two states composing the coherence. Consider for example a series of resonant interactions with laser frequencies ω_1, ω_2 and ω_3 that lead to the following sequence of coherences: $\mathrm{gg} \rightarrow \mathrm{v'g} \rightarrow \mathrm{v'v} \rightarrow \mathrm{ev}$ where the energy of each state increases in the order $\mathrm{g, v, v', e}$. Time domain spectroscopy directly measures the oscillations of each coherence after creation so one expects coherence frequencies of $\omega_{\mathrm{v'g}}$, $\omega_{\mathrm{v'v}}$ and ω_{ev}.

In frequency domain spectroscopy, one measures the enhancements of the final coherence because of the resonance that creates each coherence. By successive application of equations (11)–(14), one can show that, in the steady state and the rotating wave approximation, the final coherence can be written as

$$\rho_{ev} = -\frac{\Omega_{gv}\Omega_{gv'}\Omega_{v'e}\exp\{i[(k_1 - k_2 + k_3)z - [(\omega_1 - \omega_2 + \omega_3)t]\}\rho^0_{\alpha\alpha}}{8\Delta_{v'g}\Delta_{v'v}\Delta_{ev}} \tag{15}$$

where $\Delta_{v'g} \equiv \omega_{v'g} - \omega_1 - i\Gamma_{v'g}$, $\Delta_{v'v} \equiv \omega_{v'v} - (\omega_1 - \omega_2) - i\Gamma_{v'v}$ and $\Delta_{ev} \equiv \omega_{ev} - \omega_4 - i\Gamma_{ev}$. There are three resonance enhancements that are given by $\Delta_{v'g}$, $\Delta_{v'v}$ and Δ_{ev}.The Rabi frequencies reflect the transitions between each state in the pathway, the resonance denominators reflect the states of each coherence and the wavevectors and frequencies reflect the applied fields. The negative sign appears because there was a single bra side transition in the pathway.

Processes that involve multiple transitions are classified as parametric if only the bra or ket state changes and non-parametric if both the bra and ket states change along the coherent pathways. The distinction is important because the output coherence's phase is different for each process. If two coherences are simultaneously present, either constructive or destructive interference occurs, depending on their relative phases.

Example Liouville diagrams are shown in figure 4 for representative linear and non-linear spectroscopies. The two letters label the bra and ket states of the coherence and the numbers label the excitation field. The figure also shows WMEL diagrams that visualize the resonances [146]. Here, full and dotted arrows label the ket and bra state transitions between the states identified with letters while the final arrow is the output field from the final coherence. The initial population and the final coherence are each enclosed in a box. Linear refraction and absorption are simply described by a single arrow to the output coherence in the Liouville diagram and a single resonance in the WMEL diagram. Equation (11) describes the coherence

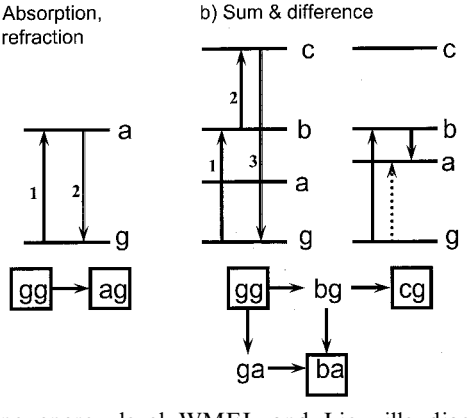

Figure 4. The wave mixing energy level WMEL and Liouville diagrams that show the resonances and coherence pathways for (*a*) absorption and refraction and (*b*) sum and difference frequency TWM. The pairs of letters indicate the two states of a coherence that is created by interaction with the fields labelled by 1–3. Full arrows indicate ket side transitions where the first state of the coherence changes while the dotted arrows indicates a bra side transition where the second state of the coherence changes. Boxes indicate the initial ground state population and the final emitting coherence.

associated with linear refraction and absorption. The real part of the coherence describes refraction and the imaginary part of the coherence describes absorption. Interaction with other fields causes further changes of the coherence and results in the non-linear spectroscopies.

The final coherence is an oscillating charge which emits an output field if it has a dipole moment [2, 3, 111]. The non-linear polarization that is associated with the oscillating charge is related to the coherence by

$$P = NF(\mu_{ba}\rho_{ba} + \mu_{ba}\rho_{ab}) \tag{16}$$

where N is the concentration of chromophores (cm^{-3}) and F is the local field enhancement factor, $F = (n^2 + 2)/3$. The non-linear polarization launches a field that is determined by the equation:

$$\frac{\partial E^0}{\partial z} + \frac{n}{c}\frac{\partial E^0}{\partial t} = \frac{2\pi i F \omega P^0}{nc} e^{i\Delta kz} \tag{17}$$

where P^o is defined by $P = \frac{1}{2}[P^o e^{i(k'z-\omega t)} + P^{o^*} e^{-i(k'z=\omega t)}]$ and $\Delta k \equiv k' - k$ is the difference in the polarization and field wavevectors. Equation (1) relates the electric field magnitude to the output intensity.

2.3. *Non-linear Spectroscopy*

2.3.1. *Experimental considerations*

Experimentally, it is also important to consider the spatial dependence of the non-linear polarization and the fields [2, 3, 87, 89, 111]. The non-linear polarization and the electromagnetic field that it launches have different spatial modulations that are characterized by the wavevectors. The non-linear polarization wavevector, k', is the vector sum of the excitation beams' wavevectors so

$$\boldsymbol{k}' = \sum_i \pm \boldsymbol{k}_i. \tag{18}$$

The $\boldsymbol{k}_i$ depend on the beam direction and the indices of refraction at the excitation frequencies, ω_i. The field that is launched by the non-linear polarization has a wavevector that depends on the index of refraction at the output frequency. Since the indices of refraction are generally different at different frequencies, the wavevector of the non-linear polarization is different from the field that it launches. Thus, the non-linear polarization and the output fields become out of phase and limit the field that can be created. Phase matching is performed by bringing the excitation beams together at angles so the vector sum will match the field's wavevector. Since the beams are now angled, there is a limited region where the excitation beams overlap so the angled beams limit the mixing efficiency.

The refractive index and absorption in a sample are frequency dependent and change the multidimensional spectrum through the changing phase matching conditions and effective mixing pathlength [147, 148]. These changes can distort lineshapes and create new features that can be mistaken for multiresonant peaks. In addition, there can be lineshape changes from coherent interference between non-resonant and resonant signals. This interference often occurs in a sample because there is always a background contribution from non-resonant electronic states. The real part of this contribution is expected to dominate and it is often tempting to subtract the window contribution from the sample background. However, there is a subtle effect that becomes important when a thin sample is contained between thick

windows. Since the windows and sample have different refractive index dispersions, it is not possible to phase match both materials simultaneously. In order to understand these effects, consider a sample cell that has a glass window, the sample solution and a second glass window. Scholten *et al.* described the dependence of signal intensity (I_4) on material properties [149] using the following formalism. We assume there are three excitation beams (with intensities I_1–I_3) and we assume that the windows are transparent to all four interacting beams [147, 148]:

$$I_4 \propto I_1 I_2 I_3 |M_s \chi_s^{(3)} + M_w \chi_w^{(3)}|^2. \tag{19}$$

M_s and M_w are phase matching factors that depend on the window and sample wavevectors (k_{w_i}, k_{s_i}) and on the sample absorption coefficients (α_{s_i}) at each experimental frequency ω_i:

$$M_s = e^{i\,\Delta k_w l_w} \left\{ \frac{e^{i(\Delta k_s l_s)}\, e^{-\Delta\alpha_s l_s} - 1}{i\,\Delta k_s - \Delta\alpha_s} \right), \tag{20}$$

$$M_w = [1 + e^{i(\Delta k_s l_s + \Delta k_w l_w)}\, e^{-\Delta\alpha_s l_s}] \left(\frac{e^{i\,\Delta k_w\, l_w} - 1}{i\,\Delta k_w} \right) \tag{21}$$

where

$$\Delta\alpha_s = \alpha_{s_1} + \alpha_{s_2} + \alpha_{s_3} - \alpha_{s_4}, \tag{22}$$

$$\Delta k_s = \overline{k_{s_1}} - \overline{k_{s_2}} + \overline{k_{s_3}} - \overline{k_{s_4}}. \tag{23}$$

In our experimental geometry k_1 and k_3 are collinear and k_2 is angled at θ_s. The sample phase mismatch (Δk_s) for this geometry is given in equation (6).

$$\Delta k_s = 2\pi \sqrt{(\omega_1 n_{s_1} + \omega_3 n_{s_3})^2 + (\omega_2 n_{s_2})^2 + \omega_2 n_{s_2} (\omega_1 n_{s_1} + \omega_3 n_{s_3}) \cos(\theta_s)} - 2\pi\omega_4 n_{s_4} \tag{24}$$

An analogous expression describes the window phase mismatch, Δk_w. These equations describe the refractive index and absorption effects on the CMDVS spectra.

If $\Delta k_w \neq 0$, equation (21) shows that M_w can be complex so the net window contribution can have imaginary character even if χ_w is real. The phase mismatch of the windows can therefore change the relative amounts of real and imaginary character in equation (19) so the sample's lineshape changes. These effects can be important when there is inadequate discrimination against non-resonant non-linear polarizations. These artifacts can occur in frequency domain spectroscopy where the pulse lengths are long [147, 148] and in time domain spectroscopy when the delays are near zero.

The non-linear output signal can be measured by homodyne or heterodyne detection [9, 10, 80, 81, 150–157]. In homodyne detection, the output intensity is measured directly and it is proportional to the squared electric field strength through equation (1). In heterodyne detection, the output electric field is overlapped with another reference electric field that serves as a local oscillator and one measures the resulting intensity. Since

$$I = \frac{cn\xi}{4\pi} |E_{signal} + E_{local}|^2, \tag{25}$$

there is a cross-term, $E_{signal}E_{local}$, that is linear in the signal field and becomes large if E_{local} is large. If the local oscillator has a constant intensity, heterodyne detection improves the detection sensitivity. One must simply discriminate between the signal and local oscillator. Often the discrimination is achieved by chopping one of the excitation beams so E_{signal} is modulated [12, 156, 158]. Measuring the signal with a lock-in detector then discriminates against interfering signals that do not involve the signal. The most important reason to use heterodyne detection is the ability to measure independently the phase of the signal field relative to the local oscillator. Clearly, the signal and local oscillator must have the same frequency if they are to have a constant phase relationship. In addition, the experimental system must be stable enough to maintain a constant phase relationship within $\lambda/100$ or better over the course of the experiment in order to avoid excess noise and artifacts. One of the most stable approaches uses diffractive optics to generate multiple beams from a single common beam [80, 81].

In time domain methods, the phases of the different coherences are measured by adjusting the time delays between excitation pulses. Jonas and coworkers described the relationship between adjusting the phase directly and changing the time delays [159, 160]. The time domain signal is then converted to the frequency domain by Fourier transformation. The time domain signal may be apodized to improve the resolution by increasing the weight of the long-time components but S/N is degraded and artifacts can be introduced into the spectrum [12, 110]. The apodization can also decrease the weighting and increase S/N but the resolution is then degraded.

There can also be artifacts introduced in the data treatment. In stimulated photon echo methods, the signal in the direction $-k_1 + k_2 + k_3$ is measured in order to take advantage of the rephasing of inhomogeneously broadened coherences where the inhomogeneous broadening of the different vibrational modes is correlated. Here, k_1 is the k vector of the first excitation beam. If the first time delay, t_{12}, is moved to negative values so the first and second excitation beams exchange places; one is then measuring the signal at $-k_2 + k_1 + k_3$. This signal corresponds to a virtual echo which does not rephase if the inhomogeneous broadening of the different modes is correlated (see later discussion). Often, the virtual echo is ignored and only signals with $t_{12} > 0$ are considered for the Fourier transformation. However, it has been pointed out that the neglect of the $t_{12} < 0$ data causes distortions of the lineshape after the Fourier transformation [106]. The distortion can result in a misinterpretation of the inhomogeneous broadening.

Ghosting artifacts can also be introduced into time domain spectra if there are periodic positional errors in the translation stages used to change the time delays. When the periodic errors are Fourier transformed, they give rise to ghost peaks that are analogous to the ghosts that are seen in mechanically ruled diffraction gratings [10].

2.3.2. *Three-wave mixing spectroscopy*

Sum and difference frequency spectroscopy are the non-linear processes possible with TWM [134, 161]. Two excitation beams (ω_1 and ω_2) are focused into an anisotropic sample and new fields are created at the sum and difference frequencies ($\omega_3 = \omega_1 \pm \omega_2$). The requirement for anisotropy gives TWM methods their superb surface selectivity. Second-harmonic generation and optical rectification are special cases of sum and difference frequency spectroscopy where the two excitation beams

have the same frequency [13, 15, 69]. The coherence pathways responsible for TWM are shown in figure 4(b) [162–164]. Sum frequency spectroscopy is a parametric process with a single path to the ρ_{cg} output coherence (see figure 4(b)). Difference frequency spectroscopy is a non-parametric process with two paths to the output ρ_{ba} coherence. These two pathways can interfere if their coherences overlap in space and time. Experimentally, the ω_1 frequency has always been larger than typical vibrational frequencies so the output signals appear in the visible and are easily detected. However, this choice does not allow resonance with two vibrational modes, as required for a 2D DOVE TWM process. If ω_1 is vibrationally resonant in a 2D DOVE TWM experiment, the output frequency appears in the infrared, which is more difficult to detect. This problem may account, at least partially, for the lack of 2D DOVE TWM experiments.

The magnitude of the coherence generated by each pathway depends on the ratio of the product of the Rabi frequencies of the three transitions to the product of the detuning factors for the two resonances [162–164]. For sum frequency spectroscopy in the steady state,

$$\rho_{cg} = \frac{\Omega_{gb}\Omega_{bc}}{4\Delta_{bg}\Delta_{cg}} \tag{26}$$

where $\Delta_{bg} = \omega_{bg} - \omega_1 - i\Gamma_{bg}$ and $\Delta_{cg} = \omega_{cg} - \omega_1 - \omega_2 - i\Gamma_{cg}$ while for difference frequency spectroscopy,

$$\rho_{ba} = -\frac{\Omega_{gb}\Omega_{ga}}{\Delta_{ga}\Delta_{ba}} - \frac{\Omega_{gb}\Omega_{ga}}{\Delta_{bg}\Delta_{ba}} = \frac{\Omega_{gb}\Omega_{ga}}{\Delta^*_{ag}\Delta_{ba}} - \frac{\Omega_{gb}\Omega_{ga}}{\Delta_{bg}\Delta_{ba}} \tag{27}$$

where $\Delta^*_{ag} = \omega_{ag} - \omega_2 + i\Gamma_{ag}$ and $\Delta_{ba} = \omega_{ba} - \omega_1 + \omega_2 + i\Gamma_{ba}$.

In these calculations, one must perform a sum over all the possible states. The states can be resonant or non-resonant. The implementation of sum and difference frequency spectroscopy rests on the choice of states. The states a, b and c can be either electronic or vibrational. Non-resonant electronic states would be considered virtual states in the language of Raman spectroscopy. There are three choices—all the states can be electronic, one state can be vibrational and one electronic or all can be vibrational. The excitation frequencies can be resonant or non-resonant with any of the states. Non-resonant excitation is usually indicated on WMEL diagrams by dotting the upper state level. Experimentally, all of the sum and difference spectroscopies performed thus far have used either electronic states for every transition or a single electronic state and a vibrational state. The latter case allows sum frequency spectroscopy to perform 1D vibrational spectroscopy selectively on surfaces [13, 15, 65–69, 161, 165]. The resonances require one infrared absorption transition and one Raman transition, both involving the same vibrational mode. Since only one mode is involved, the spectra have the same information as 1D infrared/Raman spectra and CMDVS spectroscopy is not possible.

On the other hand, if the a and b states in the figure 4 WMEL diagrams are vibrational modes, sum frequency spectroscopy will have three transitions, g → b, b → c and c → g. For DOVE, at least one of these transitions must involve a combination band. For example, let $|i,j\rangle$ represent the vibrational quantum numbers of a and b states. The three transitions could then involve the sequence $|0,0\rangle \rightarrow |1,0\rangle \rightarrow |1,1\rangle \rightarrow |0,0\rangle$ so the first two transitions are fundamentals with $\Delta v = \pm 1$ but the final transition requires a combination band where two vibrational

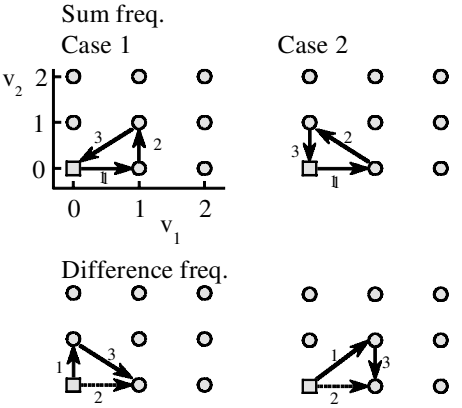

Figure 5. The arrows show the changes in the two vibrational quantum numbers, ν_1 and ν_2, that occur during the three transitions in a sum and difference frequency experiment for DOVE TWM.

quantum numbers must change. The combination band transition is a double vibrational quantum excitation. In this example, state c is a combination band of states a and b. If this process is to be observed, the combination band would need a reasonable intensity. There are other approaches as well. Figure 5 diagrams the changes in vibrational quantum numbers for the three transitions under different choices of resonance conditions. The system starts in the state indicated by the square and the transitions change the vibrational quantum numbers. The axes are the vibrational quantum numbers of coupled vibrational modes. The diagonal arrows are combination bands and the other arrows are fundamentals. The numbers label the transitions, not the fields inducing the transitions. Conservation of energy requires closed figures.

In difference frequency spectroscopy, there are also two vibrational states and three transitions, g → a, g → b and b → a. Again, at least one of these transitions must involve a combination band for DOVE. As an example, the three transitions could involve the sequence $|0,0\rangle \rightarrow |1,0\rangle, |0,0\rangle \rightarrow |0,1\rangle$ and $|1,0\rangle \rightarrow |0,1\rangle$. The first two transitions are again fundamentals with $\Delta v = \pm 1$ and the final transition is a combination difference band where two vibrational quantum numbers must change. The combination transition in this case is a zero vibrational quantum transition since one mode increases by 1 while the other decreases by 1. Figure 5 diagrams the changes in vibrational quantum numbers for the three transitions under different choices of resonance conditions [143].

The magnitudes of the sum and difference frequency coherences are related to each other. They both involve infrared transitions where $\Delta v = +1$ for vibrational modes a and b (note that the b → c transition for sum frequency generation has $\Delta v = +1$ for mode a since c = a + b) and a combination band involving either the sum or differences of modes b and a. A sum and a difference combination band have the same transition strength [166]. The similarity of the transitions suggests that the DOVE sum and difference spectroscopies should have similar strengths. The primary difference lies in how the anharmonicities affect the transition strengths and the output frequencies. For example, difference frequency spectroscopy involves the g → a transition whereas sum frequency spectroscopy involves the b → (a + b)

transition if state c is the (a + b) combination band. The two cases differ in whether the excitation of the a mode occurs from the unexcited ground state or an excited b mode. The differences are the result of the change in the oscillator strength that is caused by the anharmonicity when modes a and b are excited.

In both sum and difference frequency spectroscopy, cross-peaks between two different modes can only be observed if there is mode coupling. Excitation of one mode causes changes in the molecule's electronic structure that affect a second mode so the second mode experiences modulations at the frequency of the first mode and vice versa. The mode coupling causes combination bands and anharmonic shifts in the combination band energy relative to the sum of the two coupled fundamentals. It is this coupling that provides DOVE with its sensitivity to intra- and intermolecular interactions.

The shape of DOVE spectral features depends on the resonances in the coherent pathways shown in figure 4. The lineshapes for the DOVE sum frequency pathway and the two DOVE difference frequency pathways are shown in figure 6. The DOVE sum frequency lineshape has a vertical symmetry along one axis and a negatively sloped symmetry along the other axis because the Δ_{ag} and Δ_{cg} resonances depend on ω_1 and $\omega_1 + \omega_2$ respectively. The shapes for both DOVE difference frequency pathways have a positively sloped diagonal character because each has a Δ_{ba} resonance that depends on $\omega_1 - \omega_2$. They differ because one pathway has a Δ_{bg} and the other a Δ^*_{ag} resonance factor that depend on ω_1 and ω_2 respectively. The non-linear polarizations from the two pathways interfere so the observed lineshape depends on the relative contributions from each pathway. The relative contributions depend on the relative dephasing rates for each transition and the time ordering of the excitation pulses [143].

One of the most important factors in achieving high resolution with CMDVS is the ability to narrow broad, inhomogeneous lines. If inhomogeneous broadening is present in a sample, DOVE sum and difference frequency spectroscopies are expected to have different line-narrowing abilities [162–164]. Line narrowing is based on the selective enhancement of particular molecular transitions within an inhomogeneous line profile through double resonances with a subset of the molecular ensemble [145, 167]. For frequency domain spectroscopy in the steady state where the laser excitation is long compared with the dephasing times, an excitation within an inhomogeneously broadened transition will cause an enhancement of the resonant molecules but only a pre-resonance enhancement of the more numerous non-resonant molecules. The second excitation can create a double vibrational enhancement for the resonant molecules but only a single enhancement for the pre-resonant molecules. One might expect that the double enhancement would dominate and a sharp, line narrowed feature would be seen from the doubly resonant molecules. In fact, the situation is more complex because one must account for interference between the resonant and the near-resonant molecules [4, 56].

The resonant and near-resonant subsets of molecules will contribute non-linear polarizations which can add constructively or destructively [4, 168]. If they interfere destructively, the individual pre-resonant molecules have a smaller contribution but their greater numbers make the net contribution equivalent to the smaller number of doubly enhanced molecules. Together, the singly resonant contributions suppress the doubly enhanced contribution so that it does not dominate. The inhomogeneously broadened envelope is still observed and line narrowing does not occur. On the other hand, if they interfere constructively, the individual pre-resonant molecules augment

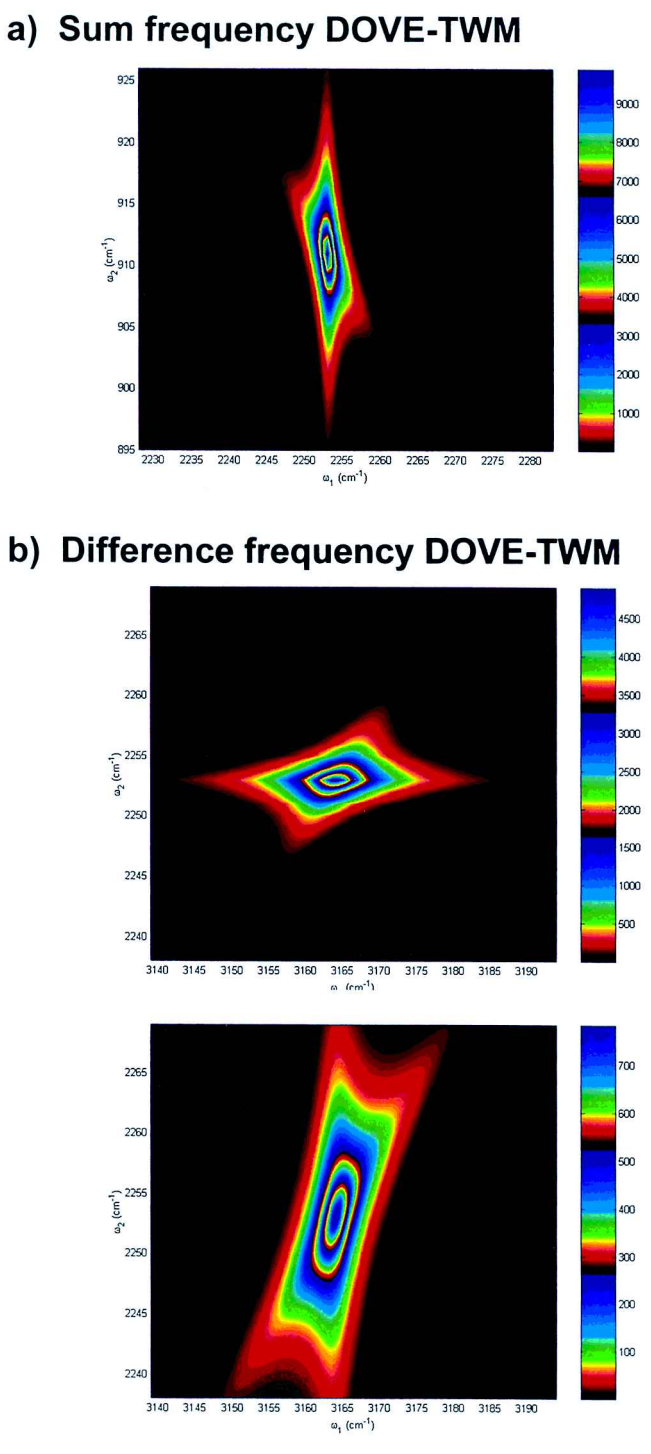

Figure 6. Simulations of the sum and difference frequency spectra for DOVE TWM with two vibrational modes. The two difference frequency spectra correspond to the two coherence pathways shown in figure 4. The multiple colour bars indicate the intensity of the output signal.

the doubly enhanced molecules' contribution so a line-narrowed feature is observed riding on top of an inhomogeneous envelope.

The interference depends on the relative signs of the real and imaginary parts of the resonance factors in the output coherence and on the relative shift of the two resonant levels that is caused by the inhomogeneous broadening [4, 168]. If the inhomogeneous broadening perturbation causes correlated shifts of the two resonant levels, then DOVE difference frequency spectroscopy produces coherences that constructively interfere and give line narrowing while DOVE sum frequency spectroscopy produces coherences that destructively interfere and do not give line narrowing. On the other hand, if the inhomogeneous broadening perturbation caused anticorrelated shifts in the two resonant levels, the DOVE sum frequency spectroscopy gives line narrowing and the DOVE difference frequency spectroscopy does not give line narrowing.

Although vibrational enhancements were first observed in TWM, TWM has not been used for CMDVS, even though TWM is the lowest-order process where DOVE mixing is possible. In TWM, the two excitation beams could have two vibrational resonances and three infrared transitions including the output transition. At least one of those transitions would require involvement of a combination band. However, current research has only used SIVE processes where there is one infrared vibrational transition and one Raman transition (remember that a Raman transition requires two transitions that each involve a real or virtual electronic state) [13, 15, 69].

2.3.3. *Four-wave mixing spectroscopy*

FWM can be accomplished in many ways and consequently there are many names associated with FWM techniques [2, 3, 111, 168]. This proliferation generates confusion but, in fact, they all can be understood with a common framework. For CMDVS, we will classify the FWM methods according to the number of vibrational resonance enhancements because the number of vibrational resonances is the most important factor that determines a technique's characteristics. One must remember that two or more vibrational resonances are required for CMDVS. Thus, SIVE, DOVE and TRIVE will designate all methods with singly, doubly or triply vibrationally enhancements.

2.3.4. *Frequency tripling and two-photon absorption*

Figure 7 summarizes many of the most common FWM methods. In these cases, three excitation beams are focused into a sample and new fields are created at all the possible sum and difference frequencies

$$\omega_4 = \pm\omega_1 \pm \omega_2 \pm \omega_3 \tag{28}$$

where ω_i and ω_j can be equal. There are three possible resonances with electronic or vibrational states.

The first example in figure 7(*a*), frequency tripling, typically uses only electronic resonances and it is not commonly used for spectroscopy. Spectroscopic applications of frequency tripling are hampered by the inability to provide phase matching in most materials and by the breadth of excited electronic state transitions. It has been used for imaging applications [169].

The second example in figure 7(*a*) is two-photon absorption spectroscopy. Often, two-photon absorption is performed with a single laser frequency. There are three

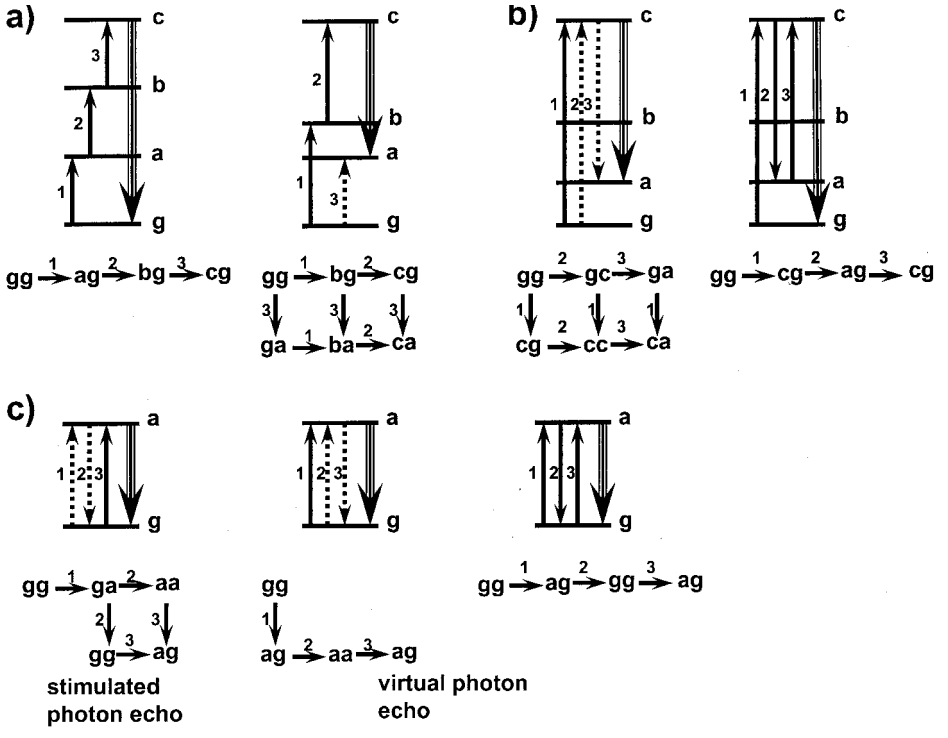

Figure 7. WMEL and Liouville diagrams for different non-linear processes. (*a*) Frequency tripling and DOVE IR. (*b*) Fluorescence and Raman. (*c*) Degenerate FWM including examples of the photon echo (left hand diagram) and the virtual photon echo (last two diagrams).

possible resonances but, commonly, the resonances involve non-resonant virtual states with the possible exception of the resonance with the highest energy state. Two-photon processes involving only virtual states are the dominant source of non-resonant background in FWM experiments. Two-photon absorption has been used for spectroscopy but it has recently found wide application for selective non-linear imaging because of its spatial resolution and gentle treatment of biological samples [170–172].

2.3.5. *Coherent and incoherent raman and fluorescence spectroscopies*

The most common non-linear spectroscopies are the family of coherent Raman spectroscopies that use one, two or three excitation source(s) for the different fields. CARS and coherent Stokes Raman spectroscopy (CSRS) are usually done with two excitation frequencies to create an output at $\omega_4 = 2\omega_1 - \omega_2$ and $\omega_4 = 2\omega_2 - \omega_1$ respectively, where $\omega_1 > \omega_2$ [173]. If three lasers are used, one can also use multiply enhanced non-parametric spectroscopy (MENS) and multiply enhanced parametric spectroscopy (MEPS) for coherent Raman spectroscopy as described in previous publications [4, 49–51, 56]. Vibrational resonance occurs when $|\omega_1 - \omega_2| = \omega_{ag}$. We previously described multidimensional spectroscopy at low temperatures where the electronic transitions are sharpened and vibronic structure is resolvable [4]. Under these conditions, one can achieve multiplicative vibrational and vibronic resonances so that line narrowing, component selection and mode selection are all possible.

The CARS, CSRS, MENS and MEPS methods created a new output frequency but FWM also can result in an output that has the same frequency as the input frequencies [168, 174]. Figure 7(*b*) shows non-linear methods with two frequencies that produce outputs at $\omega_4 = \omega_1 - \omega_2 + \omega_3 = \omega_1$ when $\omega_2 = \omega_3$ and $\omega_4 = \omega_2$ when $\omega_1 = \omega_3$. These methods become resonant when $|\omega_1 - \omega_2| = \omega_{ag}$. These diagrams correspond to Raman loss and Raman gain spectroscopy. When a vibrational resonance occurs, the ω_1 beam dims and the ω_2 beam brightens as the vibrational resonance mediates energy transfer between the two beams and simultaneously excites vibrational modes [32]. Raman loss spectroscopy is also called the inverse Raman effect when the ω_1 beam is broad and an absorption feature at the Raman frequency appears within the broad ω_1 spectral profile from the loss of photons at the position where $\omega_1 - \omega_2 = \omega_{ag}$. Raman gain spectroscopy is also called stimulated Raman scattering because the presence of ω_2 photons stimulate the emission of more ω_2 photons when $\omega_1 - \omega_2 = \omega_{ag}$. Often, stimulated Raman occurs where there is no excitation at ω_2 originally but the vacuum fluctuations provide it nonetheless and an ω_2 beam is created by amplification of the vacuum fluctuations [174].

These methods are related to traditional fluorescence and common old ordinary Raman spectroscopy (COORS) methods [32]. First, the vacuum fluctuations are responsible for spontaneous Raman and fluorescence spectroscopies. Here, the vacuum fluctuations again drive the Raman and fluorescence processes by supplying photons at ω_2. Second, the diagrams in figure 7(*b*) have two pathways that contain the ρ_{cc} population and one that involves only coherences. The two pathways that involve the ρ_{cc} population correspond to spontaneous fluorescence when ω_2 is only a vacuum photon from zero point fluctuations and to stimulated emission when there is an ω_2 field. The $gg \rightarrow gc \rightarrow ga \rightarrow ca$ pathway that involves only coherences corresponds to both fluorescence and COORS [2].

2.3.6. *Fully degenerate four-wave mixing methods*

Examples of the fully degenerate family of FWM methods are shown in figure 7(*c*). The diagram is deceptively simple. Only two states are involved and the fields are identical. Although the diagrams look simple, they include a wide range of methods including pump–probe methods, stimulated photon echo, photon echo, virtual photon echo, three-pulse stimulated photon echo peak shift, transient grating, inverse transient grating, AC Kerr effect, phase conjugation, self-focusing and self-phase modulation [2, 3, 113, 175]. Self-focusing and self-phase modulation are processes that occur in a single beam because the refractive index is intensity dependent. Self-focusing results from the spatial variation in refractive index where the more intense beam centre has a lower refractive index and lensing occurs. Self-phase modulation results from the temporal variation where more intense parts of the beam experience a lower index of refraction and speed up to overtake less intense parts of the beam, thus introducing new frequencies. These two processes play an important role in non-linear spectroscopy because they often limit the highest intensities that can be used in a sample.

The other processes are done in the time domain and involve multiple beams. Three ultrafast pulses are brought into a sample at different times and different angles. The time between the *i* and *j* pulses is t_{ij}. The field labels (*i* and *j*) specify the time ordering instead of the frequencies since now the excitation beams have the same frequency.

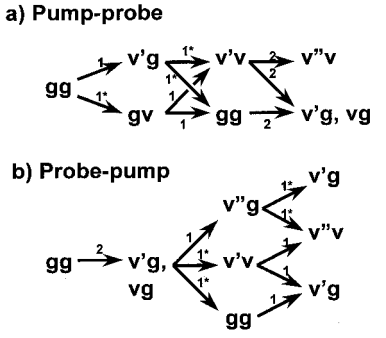

Figure 8. Flow of coherence for a pump–probe experiment for the (*a*) cases when the pump precedes the probe and (*b*) vice versa. The notation 1 and 1^* labels absorption and emission transitions, respectively.

The simplest of these processes is the pump–probe experiment where a pump beam perturbs the sample and a probe beam interrogates the changes caused by the pump beam. Figure 8 shows that the pump causes two simultaneous excitations ($t_1 = 0$) that create the populations ρ_{vv} and ρ_{gg} when $v' = v$ and coherences $\rho_{v'v}$ when $v' \neq v$. The population differences are probed at a later time, t_2, by a probe pulse. The output created by the ρ_{vg}, $\rho_{v'g}$ and $\rho_{v''v}$ coherences appears in the direction of the probe pulse and is naturally heterodyned with the probe pulse. This method is not actually a coherent spectroscopy since it involves incoherent populations but it can provide complementary information to a coherent experiment.

A coherent spectroscopy is possible by using the phase matching conditions to isolate particular output beams. Three ultrashort excitation beams are directed into a sample at different angles and new output beams are created in new directions. We consider two directions defined by the phase matching vector sums $\boldsymbol{k}_4 = -\boldsymbol{k}_1 + \boldsymbol{k}_2 + \boldsymbol{k}_3$ and $\boldsymbol{k}_4 = +\boldsymbol{k}_1 - \boldsymbol{k}_2 + \boldsymbol{k}_3$. The first corresponds to a stimulated photon echo and the second to a virtual photon echo [175]. The difference can be understood by examining the diagrams for the two processes in figure 7(*c*). The stimulated photon echo generates a ρ_{ga} coherence after the first step and a ρ_{ag} after the third step. The ρ_{ga} and ρ_{ag} coherences are complex conjugates and their temporal phases are controlled by $\exp(-i\omega_{ag}t)$ and $\exp(+i\omega_{ag}t)$, respectively. In an inhomogeneous sample, different molecules have different ω_{ag} transition frequencies so their coherences dephase during the time t_{12} after their initial creation. However, if the molecules retain their same frequencies before the conjugate coherence is created, the molecules' conjugate coherence will rephase at a time t_{34} equal to t_{12}. The intensity of the ensemble becomes large because there is a phased emission at that point in time. If the transition frequencies change in the intervening time because of a change in their environment, the time required to rephase is different and the echo shifts in time. This effect forms the basis for the three-pulse stimulated photon echo peak shift method of probing the dynamics of the environment [176–180].

The virtual echo creates a natural reference for the stimulated photon echo [177, 179, 180]. Referring back to figure 7(*c*), the virtual echo creates an initial ρ_{ag} coherence and, later, a second ρ_{ag} coherence. Since the two coherences have the same time dependence ($\exp(-i\omega_{ag}t)$), they cannot rephase in an inhomogeneously broadened system (the name virtual echo arises because the echo forms at inaccessible negative times). The virtual echo serves as a natural reference for the

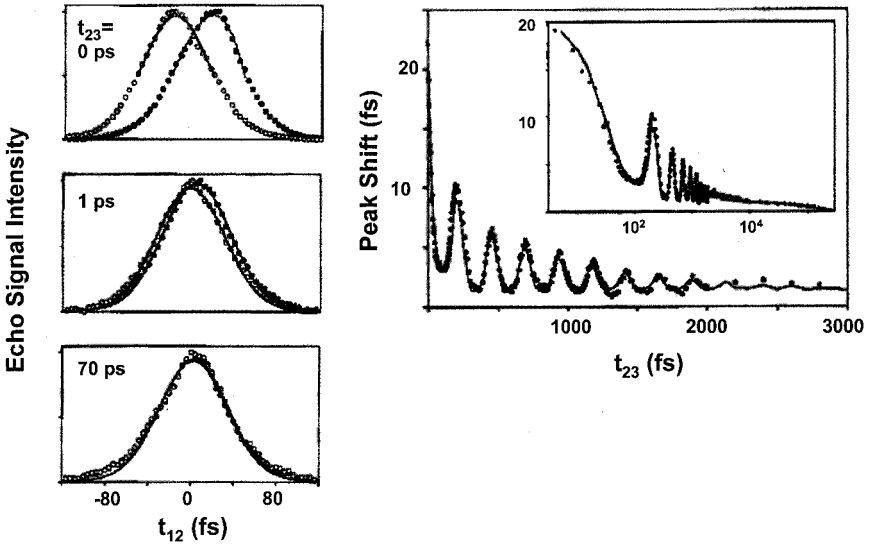

Figure 9. Three-photon SPE peak shift measurement of *N*, *N*-bis-dimethylphenyl-2,4,6,8-perylenetetracarbonyl diamide (PERY) in benzene. The t_{23} delay time is fixed at the values indicated for the left-hand signals while the t_{12} delay times are scanned. The two curves correspond to the virtual photon echo at $+k_1 - k_2 + k_3$ and the SPE at $-k_1 + k_2 + k_3$. The right-hand graph shows the peak shift between the two curves as a function of t_{23} for short times and long-times (see insert). Reproduced with permission from reference [181].

stimulated photon echo. By monitoring both the $\boldsymbol{k}_4 = -\boldsymbol{k}_1 + \boldsymbol{k}_2 + \boldsymbol{k}_3$ and the $\boldsymbol{k}_4 = \boldsymbol{k}_1 - \boldsymbol{k}_2 + \boldsymbol{k}_3$ signals, one can accurately measure temporal differences between the stimulated and virtual photon echo signals as a function of the intervening time, t_{23}, between the two coherences. During t_{23}, figure 7(*c*) shows that the system is pursuing two pathways between the initial and conjugate coherence, one involving ρ_{gg} and the other ρ_{aa}. The phase information about the ρ_{ga} coherence is encoded and stored in the population difference, $\rho_{aa} - \rho_{gg}$, during time t_{23}. Figure 9 shows an example of the shift between the stimulated photon and virtual photon echo signals for a specific t_{23} [181]. It also shows the peak shifts as a function of t_{23}. The latter graph is a direct probe of the environmental dynamics. This technique is called three-pulse stimulated photon echo peak shift (3PEPS). A variation on this technique called three-pulse photon echo short-time slope (3PESS) is a direct measure of the solvation correlation function [182].

Other methods are special cases of the stimulated photon echo and virtual photon echo [113, 175]. Photon echo methods are stimulated photon echo experiments where $t_{23} = 0$. Transient grating methods are either stimulated photon echo or virtual echo experiments where $t_{12} = 0$. In this case, the interference between the beams forms a grating that modulates the sample's refractive index and/or absorption and pulse 3 probes the dynamics of the grating relaxation. Reverse transient grating methods are virtual echo experiments with $t_{23} = 0$.

2.3.7. *Relationships with NMR*

It is insightful to compare NMR experiments with CMDVS. The aligned and anti-aligned orientations of 1/2 nuclear spins in a magnetic field create the ground

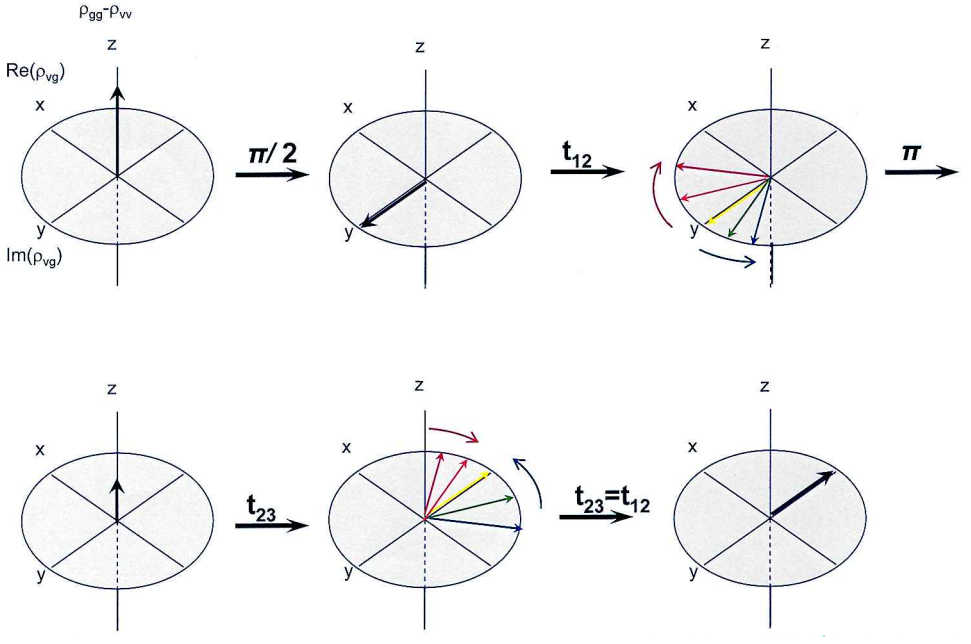

Figure 10. Spin echo experiment for a nuclear spin in the rotating frame.

and excited states in NMR [183, 184]. An aligned spin can be inverted by driving it with a resonant r.f. field. The r.f. field causes the spin to precess around the external field at the Larmor frequency as the r.f. field tips the magnetization. The tip angle continues to increase as shown in figure 10, the familiar rotating frame where the x, y and z axes reflect the spin system's in-phase, out-of-phase (relative to the driving r.f. field) and population (i.e. $n_\uparrow - n_\downarrow$) difference respectively. The arrow shows how the net magnetization rotates about the x axis and progresses from aligned to orthogonal to anti-aligned to orthogonal with the opposite phase as before and back to aligned. The frequency of this cycle is the Rabi frequency. If the r.f. pulse is turned off when the magnetization lies along the $+y$ axis, it is a $\pi/2$ pulse since the magnetization is 1/4 of the way through the entire cycle. If the spin is inverted, it is a π pulse. Between 0 and π, the spin system is absorbing energy. Between π and 2π, it is emitting energy. The spin's precession depends on maintaining its phase and magnetization. Relaxation of the phase by interactions with the environment is characterized by the dephasing time, T_2. Relaxation of the magnetization is characterized by the population relaxation time, T_1. These relaxation times are typically in the millisecond range.

A central tool in NMR is the spin echo [183, 185]. A $\pi/2$ pulse creates a coherence aligned along the y axis in figure 10. After a delay time, t_{12}, during which the coherences can dephase, a π pulse is applied to create the conjugate coherence. The conjugate coherence rephases and an echo appears after a delay time equal to t_{12}. By incrementing t_{12} and measuring the echo intensity, one can determine the dephasing rate without complication from inhomogeneous broadening affecting the measurement.

In CMDVS, the correspondences to the up and down spin states are ground and singly excited vibrational modes. Instead of a two-state system, all vibrational

quantum numbers are allowed. The connection to the coherent non-linear vibrational experiments is established through the quantum mechanical description of spin coherences. A spin coherence for a spin 1/2 system is defined by

$$|\Psi(t)\rangle = c_{\uparrow}(t)\exp(i\omega_{\uparrow}t)|\uparrow\rangle + c_{\downarrow}(t)\exp(i\omega_{\downarrow}(t)|\downarrow\rangle + \text{c.c.} \quad (29)$$

Since the spin and vibrational coherences have the same form, one can use figure 10 to describe vibrational coherences as well. The aligned spin would be analogous to the ground vibrational state and the anti-aligned spin would be analogous to the singly excited vibrational state. Figure 10 for vibrational coherences, however, does not have the same intuitive picture as a time-dependent spin orientation. Instead, the diagram visualizes the changes in the in-phase and out-of-phase components of the coherence, the population differences and the coherence magnitude. Thus, resonant optical nutation can be visualized as a vector rotating around the x axis in figure 10 at the Rabi frequency. It can also be visualized using the Liouville diagrams where it corresponds to the pathway gg $\rightarrow$ gv $\rightarrow$ vv $\rightarrow$ vg $\rightarrow$ gg $\rightarrow$ etc., but one must use caution with the Liouville diagrams because they are based on a perturbative treatment that fails in the limit of strong fields that apply for figure 10. Thus, the Liouville pathways describe the weak field limit that is required for this review while the rotating frame picture describes the high field limit that is appropriate for spins.

The amplitude, pulse width and phase of the r.f. pulses in NMR must be carefully controlled to obtain $\pi/2$ or π pulses in the strong field limit. In CMDVS, there are two ways to create vibrational coherences. One can control the amplitude and pulse width in direct analogy with the strong field limit but this is much harder to achieve with optical pulses [102, 186, 187]. It is more common to control the coherences in the Liouville picture by selecting the process of interest with the phase matching conditions [113, 175]. The key is realizing that each step in the coherence pathway is equivalent to a $\pi/2$ pulse. Thus, the initial generation of a coherence by $gg \rightarrow gv$ represents a $\pi/2$ pulse and the inversion of a population by gg $\rightarrow$ gv $\rightarrow$ vv represents an overall π pulse. The focused lasers create all possible coherences and the experimenter selects the coherent process of interest by the phase matching condition. Thus, the stimulated vibrational photon echo is created by a series of three $\pi/2$ pulses with the phase matching condition $\boldsymbol{k}_4 = -\boldsymbol{k}_1 + \boldsymbol{k}_2 + \boldsymbol{k}_3$ and this choice selects the pathways gg $\rightarrow$ gv $\rightarrow$ vv $\rightarrow$ vg and gg $\rightarrow$ gv $\rightarrow$ gg $\rightarrow$ vg. The vibrational photon echo is a subcase where the $\boldsymbol{k}_2$ and $\boldsymbol{k}_3$ overlap in time.

There are three major factors controlling a spin's Larmor frequency—the nature of the nucleus, the chemical shift and the spin–spin coupling [183]. Different nuclei have different magnetic moments. Different chemical environments also shift the Larmor frequency (chemical shifts). If a nearby nuclear spin interacts by spin–spin coupling, the spin's Larmor frequency is changed depending on whether the neighbour is aligned or anti-aligned. In this interesting case, one can manipulate the Larmor frequency by controlling the neighbouring spin. If the coupled nuclei are identical, the coupling is homonuclear and, if they are different, the coupling is heteronuclear.

In CMDVS, the analogy to the chemical shift is the energy of the vibrational mode, which is fixed by the intramolecular interactions and masses. The analogy to the spin–spin coupling is anharmonic mode coupling between a mode and other modes. The coupled modes would be 'homomodal' if they involved similar modes like a series of coupled C=O stretch modes in a polypeptide and 'heteromodal' if

they involved different modes like the C≡N stretch and C–C stretch in acetonitrile (CH_3CN).

NMR has a large family of powerful methods for extracting detailed information about molecular structure and dynamics [183, 184]. Multidimensional NMR is used extensively for structural studies of complex systems. For homonuclear systems, COSY (homonuclear correlated spectroscopy) and its relatives are the most common and useful methods. Here, an initial $\pi/2$ pulse excites spin coherences on each of the spins and a second $\pi/2$ pulse perturbs the coherences after a delay time t_{12}. The perturbed coherence is monitored by its free induction decay during the time t_{23} after the second pulse. A double Fourier transform over t_{12} and t_{23} creates a 2D spectrum containing cross-peaks from all the coupled spins.

To understand COSY, let us first watch a single spin coherence that is created after the first $\pi/2$ pulse [183–184]. During the t_{12} delay time, the coherence will dephase in the x, y plane of figure 10. If it is aligned with the $+y$ axis in figure 10 when the second $\pi/2$ pulse arrives, it becomes an inverted population (arrow points along $-z$ in figure 10). If it is aligned along $-y$, it returns to the original population. Neither of these two cases results in an emitting coherence because the system is in a pure population state. However, if the coherence is aligned at other positions in the x, y plane, part of the coherence will remain and a signal will continue to be observed. Thus, one expects that the signal will be modulated as a function of t_{12}. However, one must not forget that the populations of all the spins that are coupled to our spin have been perturbed as well so the number of our spins with a particular orientation of neighbours is being modulated at a frequency that reflects the dephasing of those neighbours. It is this perturbation of the neighbours on our spin that carries the frequency information about the neighbouring spins onto our spin [183, 184].

There are comparable NMR methods for heteronuclear systems such as ^1H–^{13}C NMR where different nuclei are excited by pulses with different centre frequencies [183, 184]. For example, heteronuclear correlation spectroscopy (HETCOR) is the heteronuclear equivalent process where the two $\pi/2$ pulses drive the ^1H nuclei in the same way as the COSY experiment but the ^{13}C are also driven, first with a π-pulse to refocus the ^1H spins and a $\pi/2$ pulse to create the ^{13}C signal. By varying the delay between the ^1H $\pi/2$ pulses, one can modulate the populations of the ^1H that couple to the ^{13}C spins and thus modulate the ^{13}C signal at a rate that is determined by the ^1H resonances.

A second approach to multidimensional NMR rests on creating multiple quantum coherences where multiple spins are simultaneously excited. A multiple quantum coherence can only be excited if the spins are coupled. Incredible natural abundance double quantum transfer (INADEQUATE) is an example of such a method [183, 184]. The multiple quantum coherence cannot be excited directly since only single spin flips occur in normal NMR experiments but the effects of the multiple quantum coherence can be measured by allowing the system to exist in the multiple quantum state before transforming it to a single quantum coherence that can be detected. Similarly, the double quantum vibrational coherence in CMDVS involves excitation of two coupled modes. In vibrational spectroscopy, this excitation appears as combination bands that result from anharmonicity between modes. Thus, unlike NMR, it is possible to excite double vibrational coherences directly through the combination bands.

3. Coherent multidimensional vibrational spectroscopies

3.1. *Fully degenerate FWM*

Fully degenerate FWM becomes a TRIVE spectroscopy when the excitation is resonant with a vibrational state. The ability to perform CMDVS depends on how it is implemented. The time delays between pulses 1, 2 and 3 and the output, 4, are indicated by t_{12}, t_{23} and t_{34}. There are six related methods that involve fully degenerate FWM—pump–probe [107, 188], heterodyned pump–probe [108], vibrational photon echo (VPE) [70, 71, 189, 190], heterodyned photon echo (HPE) [9, 10, 109, 191], stimulated photon echo (SPE) [11, 192] and heterodyned stimulated photon echo (HSPE) spectroscopies [9, 10, 12, 110, 191]. For the pump–probe experiment, $t_{12} = 0$ and one measures ΔA for the probe. For the heterodyned pump–probe experiment, $t_{12} = 0$ and one measures the modulation in ΔA for the probe as a function of t_{23}. For the VPE, $t_{23} = 0$ and one measures the echo signal as a function of t_{12}. For the HPE, $t_{23} = 0$ and one measures the modulation in the echo signal as a function of t_{12} and t_{34}. For the SPE, all $t_{ij} > 0$ and one measures the echo as a function of t_{12}. Finally, for the HSPR, all $t_{ij} > 0$ and one measures the echo signal as a function of t_{12} and t_{34}. The latter is a true time domain CMDVS.

3.1.1. *2D Pump-probe experiments*

Pump–probe methods detect the differences in the probe absorbance, ΔA, that are caused by the presence of the pump. They are not really coherent spectroscopies but they can provide 2D vibrational spectra which show cross-peaks between correlated vibrational states. They rely on sensing the differences in the probe intensity caused by the presence of the pump pulse. The 2D vibrational pump–probe experiment is actually quite complex because of its many different pathways. Figure 8 shows two sets of diagrams for the pathways. The top diagrams show the coherence pathways when the pump excitation precedes the probe. The diagrams show the pump fields (labelled by 1 and 1*) acting twice followed after a time t_1 by the probe field (labelled by 2). The different time orderings for the two pump fields are not distinguished in the pump–probe experiment. The v and v′ in the diagram may be the same mode or they may be coupled modes located at different molecular sites. Thus, v′v can indicate both a population when $v' = v$ and a coherence when $v' \neq v$. The v″ state is an overtone (if $v = v'$) or a combination band of v and v′ (if $v \neq v'$). The final coherence oscillates during the time t_2.

The pump–probe experiment measures the changes in populations and coherences that are formed after the pump. The probe signal increases because of bleaching of the ground state absorption and stimulated emission from vibrationally excited states and decreases because of excited state absorption to overtones and combination bands [107, 188]. The two pathways that proceed through the ρ_{gg} intermediate population (see figure 8) are not distinguished in the pump–probe experiment and they correspond to bleaching of the probe's absorption. The ρ_{gg} population does not have an oscillatory component during the t_1 time. The four pathways that proceed through the $\rho_{v'v}$ coherence correspond to stimulated emission if they end at the $\rho_{v'g}$ (two pathways) or excited state absorption if they end at $\rho_{v''v}$ (two pathways). The $\rho_{v'v}$ coherence oscillates at $\omega_{v'v}$ during the t_1 time. All six pathways are interrelated because they involve common coherences and/or populations so the polarizations created by each pathway interfere [107, 188]. The final coherences, $\rho_{v''v}$ and $\rho_{v'g}$, produce fields that oscillate at $\omega_{v''v}$ and $\omega_{v'g}$ during time t_2.

In the detection step, these fields heterodyne with the probe pulse to create the measured signal [108].

The bottom diagrams in figure 8 show the coherence pathways for the probe–pump experiment when the probe precedes the pump (an additional diagram is needed for when the pump and probe overlap because the probe can occur between the two pump interactions) [107, 188]. In this case, the probe excites a free induction decay of vibrational coherence and the pump excitation perturbs it. For perturbed free induction decay, the absorption, stimulated emission and excited vibrational state absorption pathways still contribute in similar ways but, in addition, two-photon vibrational absorption becomes important. The two-photon vibrational absorption pathways are those with the $\rho_{v''g}$ intermediate coherence and either the $\rho_{v'g}$ or the $\rho_{v''v}$ final coherences. The perturbed free induction decay is important for $t_1 < 0$ and can cause artifacts that complicate the pump–probe spectrum [107, 188].

Hamm *et al.* performed several different pump–probe experiments on the five C═O stretch modes of a cyclic pentapeptide. The normal infrared absorption spectrum is shown in figure 11(*a*) [107]. The five C═O fundamentals are located at 1584, 1610, 1620, 1648 and 1673 cm^{-1}. Figures 11(*b*) and (*c*) show the ΔA values in a normal pump–probe experiment with perpendicular and parallel polarizations for the pump and probe and a probe delay time of $t_1 = 800$ fs [107]. The pump had a linewidth of 12 cm^{-1} and the broad probe pulse was frequency resolved with a spectrometer and measured with a 32 element HgCdTe detector array. Increasingly negative values of ΔA appear redder on the graphs and increasing positive values appear more violet. Pumping a particular fundamental results in two features near the diagonal, one with $\Delta A < 0$ and the other with $\Delta A > 0$. Both features lie at the mode's pump frequency, $\omega_1 = \omega_{vg}$. They result from the bleaching/stimulated emission pathways and the excited vibrational state absorption pathways respectively. The $\Delta A < 0$ feature is most prominent when the probe frequency matches the fundamental frequency, $\omega_2 = \omega_{vg}$ and the $\Delta A > 0$ feature is most prominent when $\omega_2 = \omega_{v''v'}$. The diagonal $\Delta A > 0$ feature involves the overtone state of the fundamental mode and it is offset by the overtone's anharmonicity. If there is no anharmonicity, the two features cancel because they have opposite phases and $\Delta A = 0$.

The spectrum also has cross-peaks from coupled modes [107]. Cross-peaks are reported between all the modes except for the 1610 and 1620 cm^{-1} modes but the only features that appear as recognizable cross-peaks in Figure 11(*b*) are the $\Delta A > 0$ feature at $\omega_1 = 1610\,cm^{-1}$, $\omega_2 = 1574\,cm^{-1}$ and the $\Delta A < 0$ feature at $\omega_1 = 1648\,cm^{-1}$, $\omega_2 = 1586\,cm^{-1}$. The other cross-peaks are clearer in 1D slices through the contour plot. The figure does have other features that appear to be cross-peaks but these have not been assigned or discussed.

3.1.2. *Heterodyned 2D pump-probe experiments*

Figure 12 shows the dynamics of the probe absorption in the pump–probe experiment [108]. Here, a broadband pump excites all the vibrational modes in the C═O stretch region and the probe absorption difference, ΔA, is measured as a function of the pump–probe delay (t_1) and the probe frequency (ω_2). The data at negative delay times ($t_1 < 0$) are ignored because the signal is dominated by perturbed free induction decay. At positive delay times, there are a series of peaks and valleys. The valleys appear at the positions of the fundamentals at 1584, 1610, 1620, 1648 and 1673 cm^{-1} and represent the decreased probe absorption that results

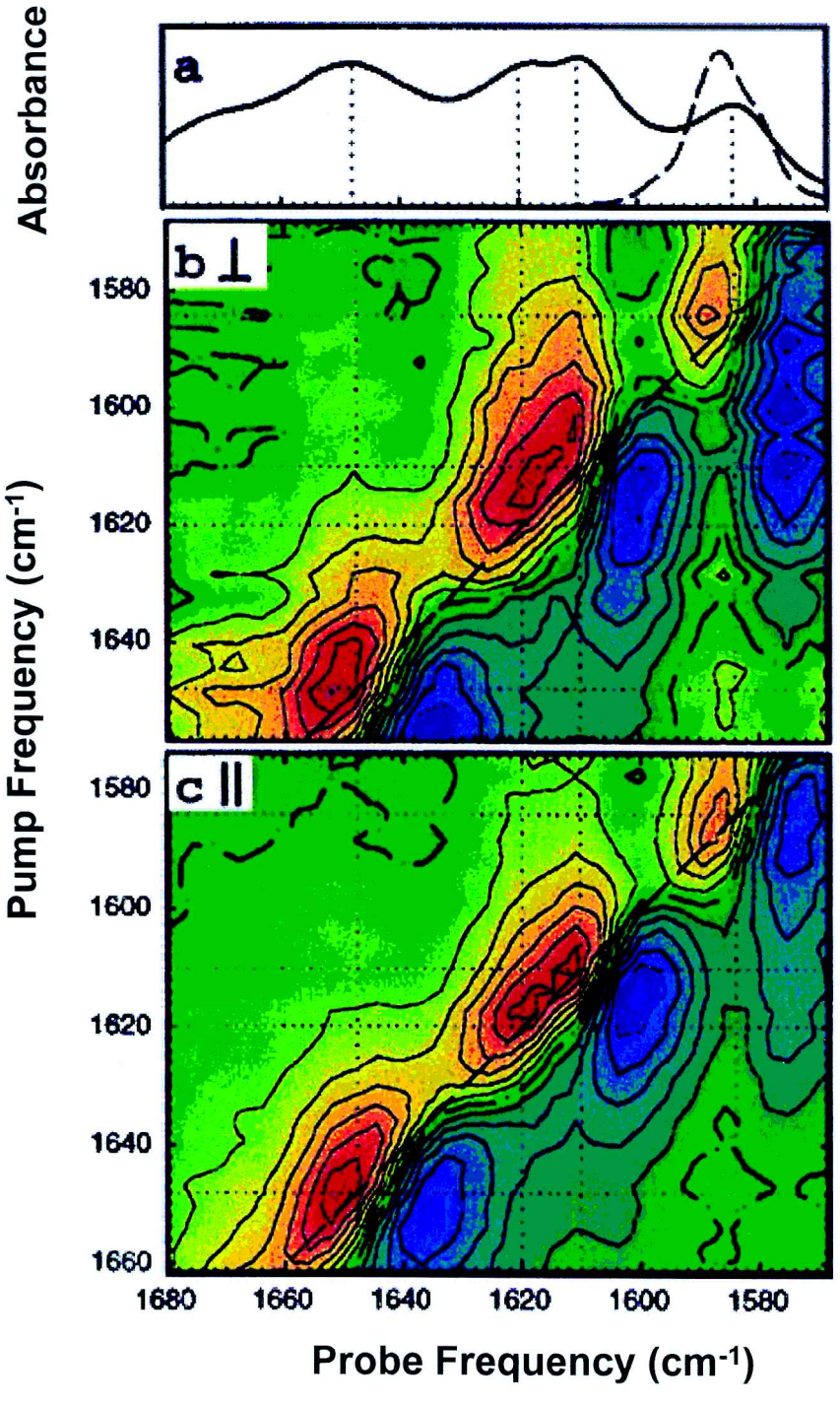

Figure 11. (*a*) Absorbance change in the pump–probe for different delay times and probe frequencies of *cyclo*-Mamb–Abu–Arg–Gly–Asp cyclic pentapeptide. (*b*) Frequency domain absorbance changes in a pump–probe spectrum of pentapeptide. Redder colours indicate negative signals and bluer colours indicate positive signals. Reproduced with permission from reference [107].

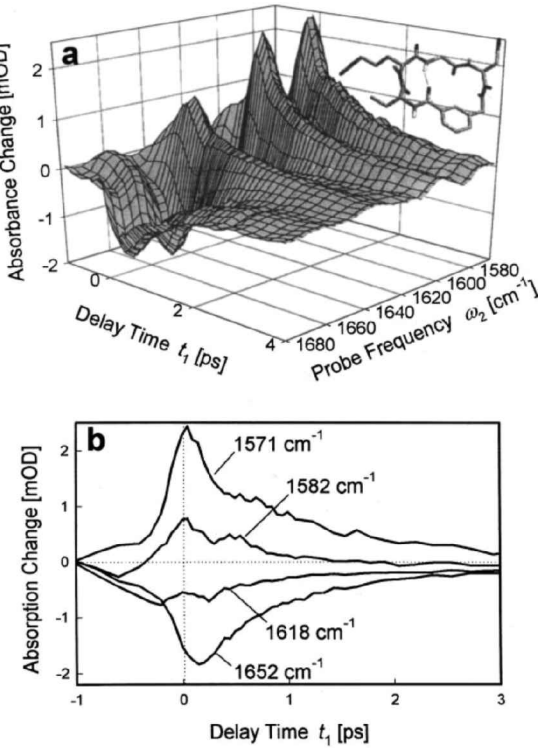

Figure 12. (*a*) Absorbance change in the pump–probe for different delay times and probe frequencies of the cyclic pentapeptide in figure 11. (*b*) Slices through the pump–probe graph for specific probe frequencies. Reproduced with permission from reference [108].

from the bleaching (gg → v′g → gg → v′g and gg → gv → gg → v′g in figure 8) and stimulated emission pathways (gg → v′g → v′v → v′g and gg → gv → v′v → v′g in figure 8) that perturb the final $\rho_{v'g}$ coherence. The peaks appear at positions that are redshifted from the fundamentals. They represent the increased probe absorption that results from the excited vibrational state absorption pathways (gg → v′g → v′v → v″v and gg → gv → v′v → v″v in figure 8). The peaks are redshifted because the excitation of one vibrational mode typically lowers the frequency of the coupled mode by the anharmonicity of the combination band, i.e. $\omega_{v'g} > \omega_{(v+v')v}$. Figures 11(*b*) and 11(*c*) are related to figure 12. Projecting the 2D plot in figures11(*b*) or (*c*) onto the probe frequency axis will give a slice of the data in figure 12(*a*) along the $t_1 = 0.8$ ps section.

Figure 12(*b*) provides slices through the data of figure 12(*a*) that show the relaxation dynamics for representative ω_2 probe frequencies [108]. At $t > 0$, the peaks and dips relax at rates that depend on the vibrational dephasing and population lifetimes but there are also reproducible oscillations that have the appearance of noise. The relaxation at 1582 cm^{-1} in figure 12(*b*) is a good example of these oscillations. If one performs a Fourier transform of t_1, one obtains the 2D spectrum in figure 13(*b*) where the ω_1 axis is the Fourier transform [108]. The oscillations now appear as peaks at specific ω_1 values for the particular choice of ω_2.

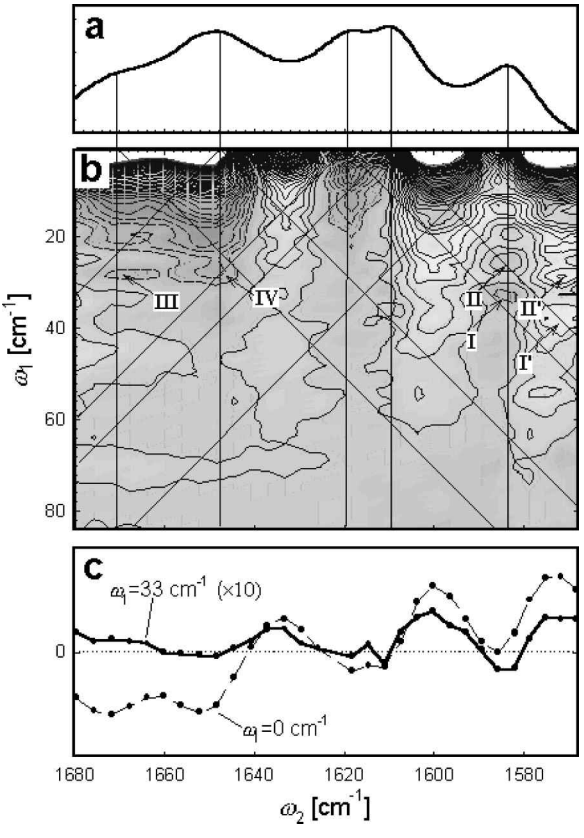

Figure 13. (*a*) Absorption spectrum of the cyclic pentapeptide in figure 11 along with the spectrum of the pump. (*b*) Contour plot of the 2D vibrational pump–probe spectrum where full contour lines and light shading are positive signals and broken lines with dark shading are negative signals. I–IV indicate particular cross-peaks between C═O modes. The vertical and diagonal lines indicate expected positions of modes and their cross-peaks. (*c*) Slices through 2D plot for the indicated ω_1 values. Reproduced with permission from reference [108].

The oscillations are visible because the detection of a pump–probe experiment is inherently a heterodyne measurement where the field launched by the non-linear polarization heterodynes with the probe field [9, 150–157, 191, 193]. The oscillations in the $\rho_{v'v}$ coherence (see figure 8) during t_1 create corresponding oscillations in the output field relative to the probe field because the heterodyne method is sensitive to the relative phases of the fields.

The lighter shaded areas and the full contour lines in figure 13 correspond to $\Delta A > 0$ and the darker shaded areas and the broken contour lines correspond to $\Delta A < 0$ [108]. Vertical lines define the positions of particular vibrational modes, $\omega_2 = \omega_{vg}$, and diagonal lines define the positions expected when these modes couple to form cross-peaks with other modes, $\omega_2 \pm \omega_1 = \omega_{v'g}$. Thus, coupling between two modes should cause two cross-peaks, one at each intersection of the diagonal from one mode and the vertical line of the other mode. The only difference in the two cross-peaks is whether the coherence pathway involves a $\rho_{v'v}$ or $\rho_{vv'}$ coherence. As an example, if the 1584 and 1610 cm^{-1} modes are coupled, one expects a modulation

from the $\rho_{v'v}$ or $\rho_{vv'}$ coherence on the output coherence of both the $\omega_2 = 1584$ and $1610\,cm^{-1}$ probe frequencies. On Fourier transformation, they become cross-peaks at $\omega_1 = |\omega_{v'v}|$.

There are two parts to each cross-peak: one has $\Delta A < 0$ from the stimulated emission pathway and one with $\Delta A > 0$ from the excited vibrational state absorption pathway [108]. The first appears when $\omega_1 = \omega_{v'v}$ and $\omega_2 = \omega_{v'g}$ while the second appears when $\omega_1 = \omega_{v'v}$ and $\omega_2 = \omega_{v''v}$ where v'' represents the $v + v'$ combination band. These negative and positive features are offset by the anharmonicity, $\Delta\omega_{v'v}$. If there is no coupling and the anharmonicity vanishes, the two features overlap and destructively interfere and the cross-peak vanishes. Although one expects the $\Delta A < 0$ and $\Delta A > 0$ features to fall at the same ω_1 value, it has been shown that amplitude level interference between the two features shifts the ω_1 positions and changes the lineshapes of both features. The changes are dependent on whether the cross-peak arises from probing the higher- or lower-energy mode. The amplitude level interference is a consequence of the heterodyning with the probe field. The effects are explained in more detail in [108].

There are four cross-peaks identified in figure 13(*b*) as I, II, III and IV and these correspond to coupling between the modes at the $(\omega_{vg}, \omega_{v'g})$ values of (1584, 1610), (1584, 1620), (1648, 1673) and (1670, 1648) cm^{-1}, respectively [108]. The first two show both the $\Delta A < 0$ and the $\Delta A > 0$ features but the last two do not have such resolved features. Cross-peaks I and II correspond to the same coupling that produced the most prominent cross-peaks in figure 11(*b*). Notice that the $\Delta A < 0$ and $\Delta A > 0$ features (I/I′ and II/II′) do not peak at the same ω_1 value as one might expect since they are both associated with the same $\rho_{v'v}$ coherence. Instead, the I′ and II′ features are shifted to higher ω_1 frequencies by the amplitude level interference discussed above [108].

One would expect many more cross-peaks in figure 13(*b*) but it is likely they are obscured by congestion. Each pair of coupled modes produces two cross-peaks and each of those has two features ($\Delta A > 0$ and $\Delta A < 0$) with the opposite phase. Together with the remaining contributions from the wings of the diagonal features, these will all interfere to obscure the expected features. This interference will be most severe in the middle of figure 13(*b*) where many contributions overlap and least severe towards the edges of the spectrum where the overlapping contributions are minimized [108]. In addition, one must understand the dynamic processes that are responsible for the lineshapes in order to model the interference adequately. The complexity of this picture may explain why so few cross-peaks are observed and why it is difficult to confirm many of the characteristic signatures expected for cross-peaks.

3.1.3. *Vibrational photon echo*

VPE experiments detect an output beam that appears in the direction given by the phase matching condition $\boldsymbol{k}_4 = -\boldsymbol{k}_1 + \boldsymbol{k}_2 + \boldsymbol{k}_3$. Fayer and coworkers demonstrated the first VPE experiment using the free electron laser for the infrared excitation pulses [70, 189]. They then applied the method to probing the vibrational dynamics of proteins [71]. In a VPE, the initial excitation pulse creates a ρ_{ga} coherence. Both non-resonant electronic and resonant vibrational coherences are created since 'a' in ρ_{ga} can be either an electronic or a vibrational state. The coherences dephase by three processes—pure dephasing, the inhomogeneity in coherent oscillators and the population decay. The inhomogeneous contribution

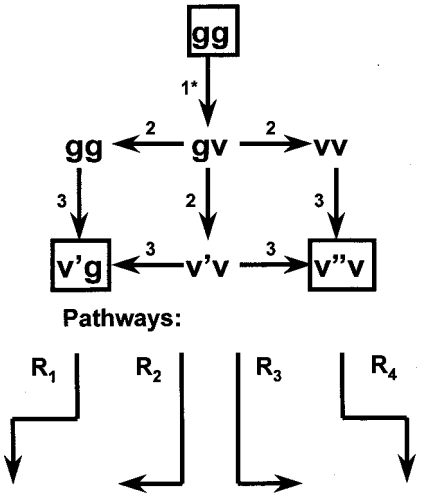

Figure 14. Liouville diagrams for the coherence pathways of stimulated photon echo. The lower arrows label particular pathways.

to the dephasing can be eliminated by the rephasing pulse [149, 190]. In the time period between the excitation and rephasing pulses, the non-resonant electronic coherence decays almost immediately and its only remaining contribution arises from overlapping of the excitation and rephasing pulses' tails. The resonant vibrational coherence dephases over picosecond time scales so it remains when the rephasing pulse arrives. By measuring the photon echo for different rephasing pulse delays, one can determine the vibrational dephasing rate caused by pure dephasing and population decay.

3.1.4. *Heterodyned stimulated photon echo*

The pump–probe and heterodyned pump–probe methods have been able to obtain 2D vibrational spectra but the cross-peaks are difficult to discern. The HSPE experiment is a more direct probe of the multiple vibrational coherences' frequencies. Figure 14 shows the coherence pathways in HSPE [9, 10, 12, 110, 158]. The key coherences for a 2D spectrum are the ρ_{gv} coherence created after the first excitation and the $\rho_{v'g}$ output coherence created after the third excitation. The ω_{gv} oscillations in the ρ_{gv} coherence can be resolved in this experiment by slowly changing t_{12}. Similarly, the $\omega_{v'g}$ oscillations can be measured if one could time resolve the $\omega_{v'g}$ oscillations of the output coherence. Heterodyne detection is a clever way to achieve this time resolution [9, 150–157, 191, 193]. One can scan the relative phases of the local oscillator pulse and the output field by changing t_{34}, the time between the third excitation pulse and the local oscillator pulse [9, 10, 12, 76, 110, 158]. The resulting signal will have an oscillatory part which represents the output coherence's relative phase. 2D spectra are obtained by performing a double Fourier transform of t_{12} and t_{34}. Alternatively, the interference fringes present in the heterodyned output signal/local oscillator fields can be measured by spectral interferometry with a monochromator that resolves the output frequency and either a single-element infrared detector or an array detector (e.g. HgCdTe) [12, 110, 158].

The different coherence pathways in figure 14 are labelled R_1–R_4[10, 12, 76, 110, 158]. The R_1 and R_2 pathways involve two bra-side transitions so the $\rho_{v'g}$ coherence

is positive. The R_3 and R_4 pathways involve one bra-side transition so the $\rho_{v''v}$ coherence is negative. If v'' is a combination band state where $v'' = v + v'$ and if there is no anharmonicity to shift the combination band's frequency or dynamics, the R_2 and R_4 pathways will cancel as will the R_1 and R_3 pathways so no cross-peak appears.

In HSPE, the initial laser pulse is divided into four pulses [10, 12, 110, 158]. For example, three excitation pulses (typically 300 nJ, 120 fs, $\Delta\nu = 150\,cm^{-1}$) are focused into a sample and the output signal in the direction of $\boldsymbol{k}_4 = -\boldsymbol{k}_1 + \boldsymbol{k}_2 + \boldsymbol{k}_3$ is combined with the fourth beam (typically 3 nJ) and measured [110]. The t_{12} and t_{23} time delays between the three excitation pulses and the t_{34} time delay between the third excitation pulse and the local oscillator can each be controlled. The first pulse excites the ρ_{gv} coherence which oscillates at ω_{gv}. Scanning the t_{12} delay time (at $1600\,cm^{-1}$, the typical step size is 18 fs, too small to meet the Nyquist criterion for a 20 fs period oscillation so aliasing corrections are necessary [110]) will resolve the ω_{gv} modulation. The second pulse's excitation produces a ground state population (gg), an excited vibrational population (vv) or a double quantum vibrational coherence ($v'v$). The populations do not have a modulation as a function of t_{23} but the coherence has an $\omega_{v'v}$ modulation. The third pulse excites the $\rho_{v'g}$ or $\rho_{v''v}$ coherence. Note that the $\rho_{v'g}$ or $\rho_{v''v}$ coherences have a π phase shift from each other so their fields have opposite signs and will interfere. The output would have an $\omega_{v'g}$ or $\omega_{v''v}$ modulation as a function of t_{34}. The $\omega_{v'g}$ or $\omega_{v''v}$ modulation can also be resolved in the output's spectrum. 2D spectra are typically obtained by scanning t_{12} and t_{34} (one can also use spectral interferometry) and 3D spectra are obtained by scanning all three time delays (or the first two delays + spectral interferometry). Frequency domain spectra in ω_1, ω_2 and ω_3 are obtained by Fourier transformation of the t_{12}, t_{23} and t_{34} time delays respectively (spectral interferometry gives the frequency dependence directly) [10, 12, 110, 158]. Since the phase information is available through the heterodyne detection, one determines not only the magnitude of the signal but also its real and imaginary parts.

Figure 15 shows a simulation of dicarbonylacetylacetonato rhodium (I)'s (RDC) 2D HSPE vibrational spectrum [158]. RDC has asymmetric and symmetric carbonyl stretching modes at 2015 and $2084\,cm^{-1}$ which we label as v and v' respectively. We write the quanta in the two modes using the notation $|vv'\rangle$. Figure 16 shows the frequencies for the transitions required to understand the spectrum. The transition frequencies involving overtones and combination bands are shifted from the fundamental frequencies by the diagonal and off-diagonal anharmonicities. Each diagonal or cross-peak has two features at $\omega_1 = |\omega_{gv}|$ and $\omega_3 = \omega_{v'g}$ or $\omega_{v''v}$ with opposite signs. The diagonal peaks have $v = v'$ and $v'' = 2v$ and the cross-peaks have $v \neq v'$ and $v'' = v + v'$. One therefore expects four diagonal peaks—the $(\omega_1, \omega_3) = (2015, 2015)$ and $(2015, 2001)\,cm^{-1}$ pair for the first diagonal feature and the $(\omega_1, \omega_3) = (2084, 2084)$ and $(2084, 2073)\,cm^{-1}$ pair for the second diagonal feature. One expects four cross-peaks—the $(\omega_1, \omega_3) = (2015, 2084)$ and $(2015, 2059)\,cm^{-1}$ pair for the first off-diagonal feature and the $(\omega_1, \omega_3) = (2084, 2015)$ and $(2084, 1990)\,cm^{-1}$ pair for the second off-diagonal feature. All of the transitions for these FWM processes are allowed since $\Delta v = \pm 1$. In addition, there are three peaks that require transitions which are forbidden in the harmonic approximation. The coherence pathways for the first set of forbidden features are $gg \rightarrow gv \rightarrow v'v \rightarrow (v' + v')v$ and $gg \rightarrow gv \rightarrow vv \rightarrow (v' + v')v$ (assuming $v' \neq v$). In each, there is a transition requiring a three-quantum change. For $v \rightarrow 2v'$, v must

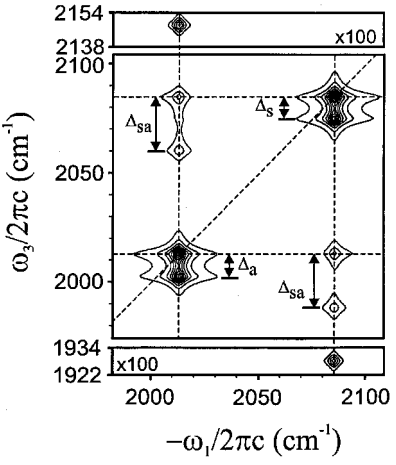

Figure 15. Simulation of the magnitude of the 2D heterodyne detected stimulated photon echo experiment in RDC. The broken lines indicate the positions of the modes and their cross-peaks. Reproduced with permission from reference [158].

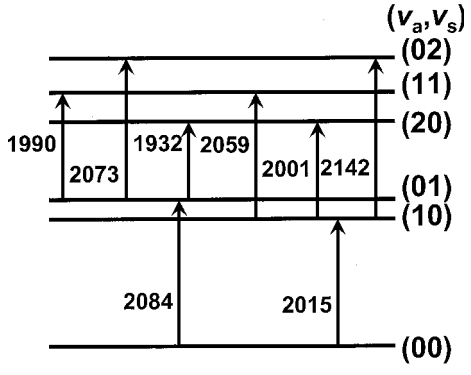

Figure 16. Transitions between vibrational states in RDC that are seen in SPE experiments. The number pairs indicated the vibrational quanta in the v_a and v_s C═O stretch modes. Adapted with permission from reference [158].

lose one vibrational quantum and v′ must gain two quanta. For (v′ + v′)v to emit, one must destroy two v′ quanta and create one v quantum. For RDC, these forbidden peaks fall at $(\omega_1, \omega_3) = (2015, 2142)$ and (2084, 1932) cm^{-1}. For the third forbidden peak, the coherence pathway is gg → gv → v′v → (v + v)v. For RDC, this pathway creates two peaks at $(\omega_1, \omega_3) = (2015, 2001)$ and (2084, 2073) cm^{-1}. These peaks fall on top of the previously described allowed peaks. They are forbidden because the third transition on the pathway involves a transition where v′ → 2v.

The relative intensities and shapes of these10 peaks have interesting dependences on a number of factors [158]. If the anharmonic shift is zero, the fields generated by the $\rho_{v'g}$ and $\rho_{v''v}$ coherences will have the same frequency and they will destructively interfere. If the two coherences also have the same dephasing dynamics and if their transition moments obey the linear dipole approximation, the two fields will be equal and no peak will appear [194]. If the anharmonic shift is finite, the dephasing

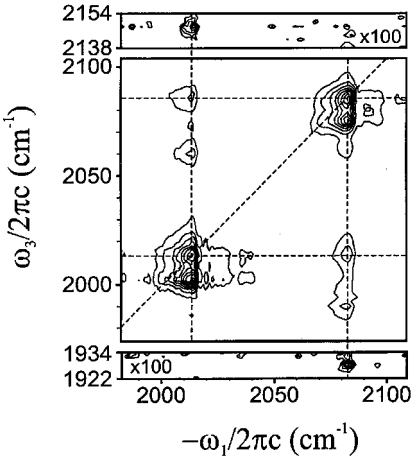

Figure 17. Magnitude of the 2D HSPE experiment in RDC. There is a factor of 100× amplification in the top and bottom sections of the figure. The broken lines indicate the positions of the modes and their cross-peaks. Reproduced with permission from reference [158].

dynamics change for different transitions or the transition moments do not obey the harmonic approximation, then a cross-peak(s) will appear. Two cross-peaks will be observed if there is an anharmonic shift. The relative intensities of the two peaks will depend on whether the coupling involves mechanical anharmonicities, electrical anharmonicities or transition dipole coupling [158, 194].

Tokmakoff has discussed how the line shapes in SPE and transient grating experiments depends on the inhomogeneous broadening [195]. In time domain photon echo experiments where a particular time ordering of pulses is defined, inhomogeneous broadening appears as an echo where the peak intensity at a time t_{34} depends linearly on the t_{12} delay time. When these are transformed into 2D frequency spectra, inhomogeneously broadened lines appear as narrowed diagonal features. If there is no inhomogeneous broadening and pure dephasing dominates, the signal relaxations along t_{12} or t_{34} are independent of each other and the 2D frequency spectrum has Lorentzian line shapes along both frequency axes. In transient grating experiments, echoes do not form in the time domain and narrowing is not observed in the 2D frequency spectra.

Figure 17 shows the experimental 2D spectrum for RDC [158]. It compares quite favourably with that predicted from the simulation in figure 15. Each diagonal feature has a pair of peaks where the diagonal anharmonic shift has caused an 11 and 14 cm^{-1} separation between the two peaks of the pair for the symmetric and asymmetric modes respectively. There is also a pair of peaks at each cross-peak position where the off-diagonal anharmonic shift has caused a 25 cm^{-1} shift between the peaks within each pair. Note also the forbidden peaks that appear at $(\omega_1, \omega_3) = (2015, 2142)$ and $(2084, 1932)$ cm^{-1}. The relative intensity of the two peaks within both the diagonal and the cross-peak pairs is the same. This similarity means that mechanical anharmonicity, either involving through-bond or through-space interactions, must determine the size of the anharmonic coupling. If electrical anharmonicity were important, the relative intensities of the two peaks in each pair would be different because the transition moments for the $\rho_{v''v}$ coherence would be different from the $\rho_{v'g}$ coherence.

Some of the most important applications of CMDVS are biological. Hochstrasser's group has pioneered the applications of CMDVS to complex peptides and proteins [11, 12, 107–110, 188, 192]. Figure 18 shows an example of a 2D vibrational spectrum of acetylproline–NH_2^+ [110]. The HSPE signal magnitude is graphed on figure 18(*a*) and the real part of the signal is plotted in figure 18(*b*). Note also that the ω_1 and ω_3 axes are interchanged from those in figures 15 and 17. In figure 18(*a*), there are three fundamental modes that are responsible for the A, B and C peaks along the diagonal: the amide II mode at 1585 cm^{-1}, the amide I mode of the acetyl CO stretch at 1630 cm^{-1} and the amide I mode of the amino CO stretch at 1690 cm^{-1}. There is also a series of cross-peaks labelled D–I. Since this system has only one additional mode compred with RDC, one would expect three allowed diagonal pairs and six allowed cross-peak pairs but the situation is much more complex [110]. The interpretation of the cross-peaks indicates there are actually two (or perhaps more) different acetylproline–NH_2^+ conformations which have vibrational frequencies for the amide II and acetyl amide I modes on either side of the A and B peak positions. So, actually, the A and B peaks are unresolved pairs of peaks from two conformations. The two conformations have the same vibrational frequencies at peak C. Each conformer would have 18 peaks but those involving the diagonal C feature would have the same frequency. The anharmonic shifts in acetylproline–NH_2^+ are smaller than in RDC so the two peaks in each pair are not resolved in the magnitude spectrum. However, since the two peaks have fields that are shifted by π, one will appear as a positive feature and one will appear as a negative feature in the real part of the signal. The real part of the signal is shown in figure 18(*b*) and the expected pairs of peaks appear in the diagonal features and in the D and G cross-peaks. However, it is also clear that the spectrum is much more complex than the RDC spectrum. The D and E peaks are assigned to cross-peaks between the amide II (diagonal feature A) and the acetyl amide I (diagonal feature B). The F and G peaks are assigned to cross-peaks between the amide II (diagonal feature A) and the amino amide I (diagonal feature C). The H and I peaks are assigned to cross-peaks between the acetyl amide I (diagonal feature B) and the amino amide I (diagonal feature C).

One should notice that, unlike RDC, the cross-peaks on either side of the diagonal are not symmetrical. This difference is attributed to the differences in the positions of the cross-peaks between the two conformers on either side of the diagonal [110]. The interferences between conformer contributions lead to changes in the lineshapes. A detailed description for the positions and shapes of the cross-peaks in the real part of the spectrum is not available in the literature because of the complexities in understanding the contributions from the dynamics of inhomogeneous and pure dephasing contributions and even the number of different conformers that are present [110]. Nevertheless, a great deal of information about the dynamics and structure can still be extracted from the spectral data. In particular, the polarization dependence of the relative peak intensities allows one to determine the angles between the two amide I transition dipoles for each of the two conformers [110].

3.2. *Non-degenerate non-linear mixing*

3.2.1. *Doubly vibrationally enhanced four wave mixing*

3.2.1.1. *Theory*. Non-degenerate FWM occurs when the excitation frequencies are different. There are a number of DOVE FWM mixing strategies that access vibrational resonances and these are sketched in figure 19 [87]. The upper state can

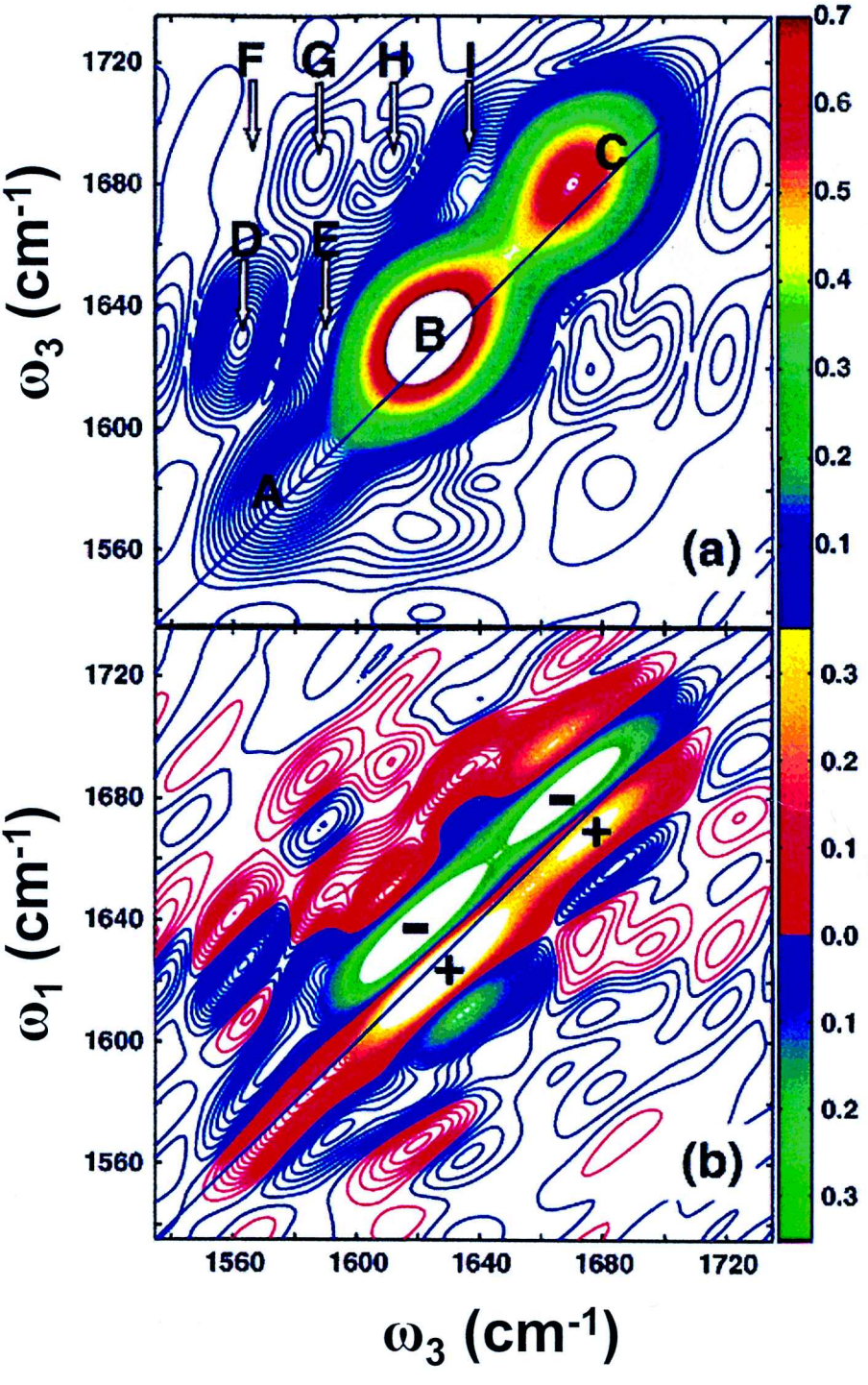

Figure 18. The top 2D spectrum shows the heterodyned detected SPE signal magnitude of acetylproline–NH_2 in $CDCl_3$. The bottom spectrum shows the real part of the signal. The diagonal and cross-peaks are labelled by A–I. Reproduced with permission from reference [110].

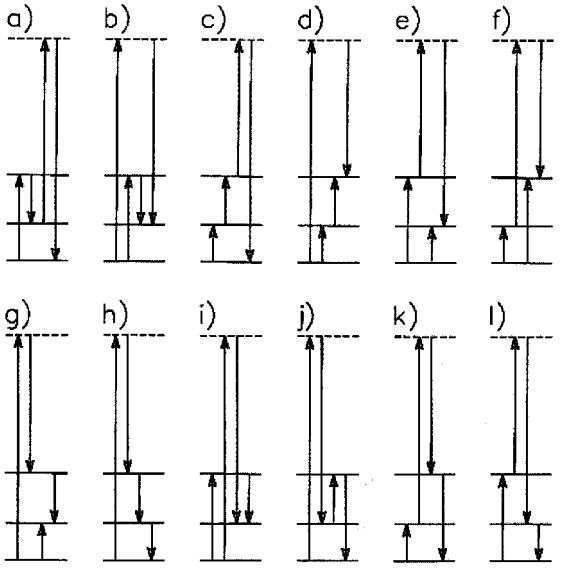

Figure 19. DOVE methods involving two infrared absorptions/emissions and one Raman transition. The diagrams for DOVE Raman and DOVE IR are (*a*) and (*b*), respectively.

represent an electronic state that may or may not be resonant (i.e. a virtual state) or it can represent a vibrational state that may or may not be the same as the others. The diagrams differ in the vibrational resonances that are accessed by the different excitation frequencies. For the case where the upper state is an electronic state, each of the diagrams involves two vibrational states that participate in two single infrared absorption/emission transitions and one Raman transition. The top diagrams show processes with two infrared absorption/emission transitions and an output frequency that is at a higher frequency and is easier to detect. The lower diagrams use a Raman transition and an infrared absorption/emission transition that drive the two vibrational resonances and the output is at a low frequency that is more difficult to detect. Although the output is more difficult to detect, the Raman transition that drives one vibrational mode is easier to create since it does not require infrared lasers. Thus far, research has focused on the DOVE Raman scheme shown in figure 19(*a*) and the DOVE IR scheme shown in figure 19(*e*) since these produce an output on the anti-Stokes side of the excitation lasers and have vibrational state energies that are compatible with convenient laser sources. The DOVE IR and DOVE Raman processes are often observed in combination with each other [90, 92, 143]. As will be seen, their transitions are very similar and one would expect them to have comparable intensities although there are cases where they are not expected to occur simultaneously.

The resonances for DOVE IR and DOVE Raman are best understood from the coherence pathways and WMEL diagrams in figure 20 [90, 92, 143]. There are three coherence pathways and the letters in the pathways can represent any molecular state. One must sum over all possible states to determine the non-linearity. We will concentrate on the resonant states since they make the largest contributions. The resonant states are easily identified in the WMEL diagrams. Here, the energy levels indicated by full lines represent ground vibrational states (indicated by a = v; b = v′;

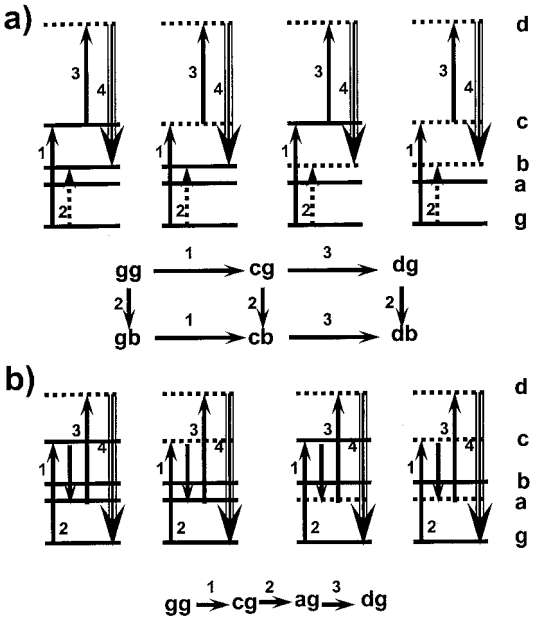

Figure 20. (*a*) Dove IR diagram where the b and c states can be either vibrational (b = v′; c = v″) or virtual electronic substitute (d = e) along with the coherence pathways. (*b*) DOVE Raman diagram showing the same possibilities (a = v; c = v″; d = e′).

c = v″) and the levels indicated by dotted lines represent non-resonant virtual electronic states (indicated by d = e or e′), i.e. high-lying electronic states that are not resonant with the excitation frequency. Since any of the levels can be a virtual or resonant state, there will be a different dependence on ω_1 and ω_2 according to which frequencies are resonant with vibrational states. Non-resonant transitions will not have an appreciable frequency dependence and we treat them as adjustable constants.

There are three pathways that are doubly vibrationally enhanced—the two that create the $\rho_{ev'}$ coherence are labelled $\rho^{\alpha}_{ev'}$ (pathway gg → v″g → v″v′ → ev′) and $\rho^{\beta}_{ev'}$ (pathway gg → gv′ → v″v′ → ev′) and one that creates the $\rho_{e'g}$ coherence (pathway gg → v″g → vg → e′g). In the rotating wave approximation, the steady state expressions for the coherences are:

$$\rho^{\alpha}_{ev'} = -\sum_{g,v,v',v'',e,e'=\text{all states}} \frac{\Omega_{gv''}\Omega_{v''e}\Omega_{gv'}}{8\Delta_{v''g}\Delta_{v''v'}\Delta_{ev'}}\rho_{gg}\exp\{i[(k_1-k_2+k_3)z-(\omega_1-\omega_2+\omega_3)t]\}, \tag{30}$$

$$\rho^{\beta}_{ev'} = \sum_{g,v,v',v'',e,e'=\text{all states}} \frac{\Omega_{gv''}\Omega_{v''e}\Omega_{gv'}}{8\Delta^{*}_{v'g}\Delta_{v''v'}\Delta_{ev'}}\rho_{gg}\exp\{i[(k_1-k_2+k_3)z-(\omega_1-\omega_2+\omega_3)t]\} \tag{31}$$

and

$$\rho_{e'g} = \sum_{g,v,v',v'',e,e'=\text{all states}} \frac{\Omega_{gv''}\Omega_{v''v}\Omega_{ve'}}{8\Delta_{v''g}\Delta_{vg}\Delta_{e'g}}\rho_{gg}\exp\{i[(k_1-k_2+k_3)z-(\omega_1-\omega_2+\omega_3)t]\} \tag{32}$$

where $\Delta_{v''g} = \omega_{v''g} - \omega_1 - i\Gamma_{v''g}$, $\Delta_{v''v'} = \omega_{v''v'} - \omega_1 + \omega_2 - i\Gamma_{v''v'}$, $\Delta_{ev'} = \omega_{ev'} - \omega_4 - i\Gamma_{ev'}$, $\Delta^*_{v'g} = \omega_{v'g} - \omega_2 + i\Gamma_{v'g}$ and $\Delta_{vg} = \omega_{vg} - \omega_1 + \omega_2 - i\Gamma_{vg}$ [143]. The summation over v, v′ and v″ includes both electronic and vibrational states but the notation emphasizes the vibrational states since those can be resonant. If we group the terms in these summations according to their dependence on the vibrationally resonant terms involving ω_1 and/or ω_2 and suppress the dependence on the non-resonant electronic states, we obtain the following expressions:

$$\rho^{\alpha}_{ev'} = -\sum_{\substack{v,v'v''=\text{all}\\ \text{vibrational states}}} \left(A^{\alpha}_{NR} + \frac{A_{v''g}}{\Delta_{v''g}} + \frac{A_{v''g,v''v'}}{\Delta_{v''g}\Delta_{v''v'}}\right)\rho_{gg} \times \exp\{i[(k_1 - k_2 + k_3)z - (\omega_1 - \omega_2 + \omega_3)t]\}, \tag{33}$$

$$\rho^{\beta}_{ev'} = \sum_{\substack{v,v'v''=\text{all}\\ \text{vibrational states}}} \left(A^{\beta}_{NR} + \frac{A_{v''g}}{\Delta^*_{v'g}} + \frac{A_{v'g,v''v'}}{\Delta^*_{v'g}\Delta_{v''v'}}\right)\rho_{gg} \times \exp\{i[(k_1 - k_2 + k_3)z - (\omega_1 - \omega_2 + \omega_3)t]\} \tag{34}$$

and

$$\rho_{e'g} = \sum_{\substack{v,v'v''=\text{all}\\ \text{vibrational states}}} \left(A^{e'g}_{NR} + \frac{A_{vg}}{\Delta_{vg}} + \frac{A_{v''g}}{\Delta_{v''g}} + \frac{A_{v'g,vg}}{\Delta^*_{v'g}\Delta_{vg}}\right)\rho_{gg} \times \exp\{i[(k_1 - k_2 + k_3)z - (\omega_1 - \omega_2 + \omega_3)t]\}, \tag{35}$$

The non-linear DOVE polarization depends on the sum of the contributions from all the coherences of all the different components:

$$P = \sum_{i=\text{all components}} N_i F[\mu^i_{ev'}(\rho^{i,\alpha}_{ev'} + \rho^{i,\beta}_{ev'}) + \mu^i_{e'g}\rho^i_{e'g} + \text{c.c.}] \tag{36}$$

where N_i is the total concentration of molecules, F is the local field correction factor and μ_{ij} is the transition dipole moment for the ρ_{ij} coherence [90, 92, 143]. The third-order susceptibility can then be written as

$$\begin{aligned}\chi^{(3)} = &\sum_{\substack{i=\text{all components}\\ v,v',v''=\text{all}\\ \text{vibrational states}}} A^i_{NR} + \frac{A^i_{\text{Raman}}}{\omega^i_{vg} - (\omega_1 - \omega_2) - i\Gamma^i_{vg}} \\ &+ \frac{A^i_{\text{SIVE 1}}}{\omega^i_{v''g} - \omega_1 - i\Gamma^i_{v''g}} + \frac{A^i_{\text{SIVE 2}}}{\omega^i_{v'g} - \omega_2 + i\Gamma^i_{v'g}} \\ &- \frac{A^i_{\text{DOVE IR }\alpha}}{(\omega^i_{v''g} - \omega_1 - i\Gamma_{v''g})(\omega^i_{v''v'} - \omega_1 + \omega_2 - i\Gamma^i_{v''v'})} \\ &+ \frac{A^i_{\text{DOVE IR }\beta}}{(\omega^i_{v'g} - \omega_2 + i\Gamma^i_{v'g})(\omega^i_{v''v'} - \omega_1 + \omega_2 - i\Gamma^i_{v''v'})} \\ &+ \frac{A^i_{\text{DOVE Raman}}}{(\omega^i_{v''g} - \omega_i - i\Gamma^i_{v''g})[\omega^i_{vg} - (\omega_1 - \omega_2) - i\Gamma^i_{vg}]}.\end{aligned} \tag{37}$$

The first term represents all the non-resonant contributions, the second term represents the CARS contribution from all the single Raman resonances, the third and fourth terms represent all the SIVE resonances that depend on ω_1 or ω_2 respectively the fifth and sixth terms represent the two DOVE IR pathways and the last term represents the DOVE Raman pathway.

A fundamental question for coherent vibrational spectroscopies is the relative importance of the different terms in equation (37) [7, 8, 88, 196]. Normally, $\chi^{(3)}$ is dominated by electronic contributions and vibrational contributions are neglected [6]. The electronic contributions dominate because the lighter electron mass makes electron clouds more polarizable than nuclear motions. Non-linearities depend on the ratio of the Rabi frequency to the detuning, Ω/Δ. A resonant vibrational resonance will contribute a factor of Ω_v/Δ_v relative to a non-resonant electronic state's value of Ω_e/Δ_e. Even though the electronic transition has a much larger Rabi frequency, it can be offset by the enhancement from the resonance factor. It was shown that the vibrational enhancement is adequate to allow the vibrational contribution to exceed the non-resonant electronic contribution [7, 8, 88, 196].

The contributions from the two DOVE IR pathways both have a dependence on $\Delta_{v''v'}$ that comes from their common intermediate $\rho_{v''v'}$ coherence. They will interfere and, since they have the opposite sign, the destructive interference can cause the dependence on $\Delta_{v''v'}$ to disappear. One can easily show that, if the pathways have equal weights as equations (23) and (24) suggest, then

$$-\frac{1}{\Delta_{v''g}\Delta_{v''v'}}+\frac{1}{\Delta^*_{v'g}\Delta_{v''v'}}=\frac{1}{\Delta_{v''g}\Delta^*_{v'g}}-i\frac{\Gamma_{v''v'}-\Gamma_{v''g}-\Gamma_{v'g}}{\Delta_{v''g}\Delta^*_{v'g}\Delta_{v''v'}}. \tag{38}$$

If $\Gamma_{v''v'}=\Gamma_{v''g}+\Gamma_{v'g}$, then the second term disappears and the $\Delta_{v''v'}$ dependence is lost [187, 197, 198]. Only a dependence on $\Delta_{v''g}$ and $\Delta_{v'g}$ is observed. Since $\Gamma_{ij}=(\Gamma_{ii}+\Gamma_{jj})/2+\Gamma^*_{ij}$ where Γ_{ii} is the population relaxation rate of the ith level and Γ^*_{ij} is the pure dephasing rate, one can show that the previous condition is equivalent to the condition $\Gamma^*_{v''v'}=\Gamma^*_{v''g}+\Gamma^*_{v'g}+\Gamma^*_{gg}=0$. This condition is met if there is no pure dephasing in the 'no pure dephasing limit'. If pure dephasing is present, the $\Delta_{v''v'}$ resonance reappears as a dephasing-induced (DICE) resonance [48]. In the gas phase, these resonances appear as pressure-induced extra resonances (PIER4) [197].

3.2.1.2. *Experimental observations*. (1) *Two-dimensional spectrum*. DOVE FWM has been observed in the model system acetonitrile [90, 92]. Figure 21 shows the infrared and Raman spectra of acetonitrile. Table 1 summarizes the vibrational modes and their frequencies. A frequency domain DOVE FWM experiment was performed with an acetonitrile–deuterobenzene mixture by scanning the ω_1 frequency across the 2950–3200 cm^{-1} region for specific values of ω_2 in the range 2230–2300 cm^{-1}. The intensity of the output was measured using a double monochromator that synchronously scanned its frequency so $\omega_{mono}=\omega_1-\omega_2+\omega_3$. The deuterobenzene was present as an internal standard because its $\chi^{(3)}$ value is known for both the non-resonant electronic contribution and the peak Raman contribution for the ring breathing mode at 944 cm^{-1} [199, 200]. The intensities of each scan can change because the absorption at ω_2 changes as ω_2 becomes resonant with infrared absorption transitions. As explained earlier, absorption shortens the effective FWM pathlength so it becomes difficult to compare the intensities of

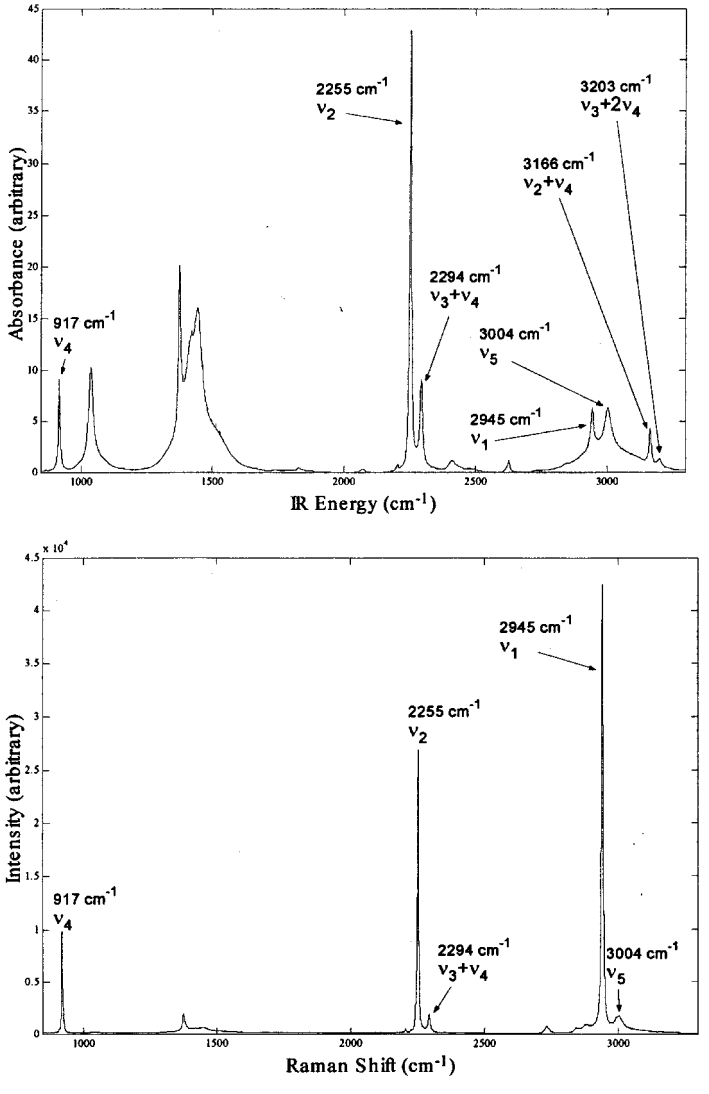

Figure 21. The infrared (top) and Raman spectra of acetonitrile.

different scans. The deuterobenzene internal reference corrects for these effects. Since the deuterobenzene Raman feature has a known $\chi^{(3)}$ at $\omega_1 - \omega_2 = 944\,\mathrm{cm}^{-1}$ that is independent of the absolute ω_1 or ω_2 value, the intensity of each scan was normalized to the intensity of the deuterobenzene Raman feature. Thus, the deuterobenzene Raman line becomes constant in the corrected spectrum.

The coherent 2D DOVE spectrum of an acetonitrile mixture with 8 mol% deuterobenzene is shown in figure 22 [92]. The dominant feature is the DOVE IR process (fifth and sixth terms in equation (37)). One can see that it appears when ω_2 is resonant with the ω_2 C≡N stretch mode at $2253\,\mathrm{cm}^{-1}$ and ω_1 is resonant with the $\nu_2 + \nu_4$ C≡N + C–C stretch combination band at $3163\,\mathrm{cm}^{-1}$. There is a second DOVE IR peak at $(\omega_1, \omega_2) = (3200, 2293)\,\mathrm{cm}^{-1}$ corresponding to an ω_2 resonance with the $\nu_3 + \nu_4$ combination band and an ω_1 resonance with the $\nu_3 + 2\nu_4$

Table 1. Resonances of importance in the IR FWM spectrum of the 35:35:3 by mole ratio mixture of acetonitrile, deuterated acetonitrile and deuterobenzene.

Molecule	Mode		Energy (cm^{-1})	Linewidth (cm)
C_6D_6	ν_2	Ring breathing	944	0.95
CH_3CN	ν_4	C–C stretch	917	1.2
			921.5	2.2
	ν_3	C–H bend	1377	
	ν_2	C≡N stretch	2255	3.5
			2251.5	6.5
	$\nu_3 + \nu_4$		2294	
	ν_1	C–H stretch	2945	
	ν_5	C–H stretch	3004	
	$\nu_2 + \nu_4$		3166	6
	$\nu_3 + 2\nu_4$		3203	
CD_3CN	ν_4	C–C stretch	832	1.2
			835.5	2.2
	ν_3	C–H bend	1101	
	ν_2	C≡N stretch	2264	3.5
			2260.5	6.5
	$\nu_2 + \nu_4$		3094	6

combination band. A third DOVE IR peak is very weakly present at $(\omega_1, \omega_2) = (3163, 2293)\,cm^{-1}$ corresponding to an ω_2 resonance with the $\nu_3 + \nu_4$ combination band and an ω_1 resonance with the $\nu_2 + \nu_4$ combination band. There is a weaker diagonal feature at $\omega_1 - \omega_2 = 918\,cm^{-1}$ that corresponds to the Raman process (second term in equation (37)) for the ν_4 C–C stretch mode. Note that the Raman line is enhanced at two places, one where ω_1 is resonant with the $\nu_2 + \nu_4$ combination band and the other when ω_1 is resonant with the $\nu_3 + 2\nu_4$ combination band. This enhancement is caused by the DOVE Raman process (seventh term in equation (37)). There is also a stronger diagonal feature with a constant intensity at $\omega_1 - \omega_2 = 944\,cm^{-1}$ corresponding to the deuterobenzene internal standard Raman feature. The spectrum has a low background signal at all the frequencies. It arises from the non-resonant electronic contributions (first term in equation (37)). In addition, the background is raised when $\omega_2 = 2253\,cm^{-1}$, presumably from the SIVE process (fourth term in equation (37)). There are interesting interference effects when any of these contributions overlap in the spectrum. The interferences change the lineshapes and relative intensities.

Equation (37) can simulate the observed spectrum [90, 92]. Figure 22(*b*) shows a simulation that reproduces the main features and allows one to estimate the relative size of the non-linearities.

(2) *Mode coupling*. The acetonitrile DOVE IR peak at $(\omega_1, \omega_2) = (\omega_{\nu_2+\nu_4}, \omega_{\nu_2})$ in figure 22(*a*) requires the two infrared transitions $g \rightarrow \nu_2 + \nu_4$ and $g \rightarrow \nu_2$ and the Raman transition $\nu_2 + \nu_4 \rightarrow \nu_2$. The $g \rightarrow \nu_2 + \nu_4$ is a combination band requiring mode coupling while the $g \rightarrow \nu_2$ and $\nu_2 + \nu_4 \rightarrow \nu_2$ are transitions with $\Delta\nu_2 = +1$ and $\Delta\nu_4 = -1$ that do not require mode coupling. The corresponding DOVE Raman peaks require the two infrared transitions $g \rightarrow \nu_2 + \nu_4$ and $\nu_2 + \nu_4 \rightarrow \nu_4$ and the Raman transition $\nu_4 \rightarrow g$. The $g \rightarrow \nu_2 + \nu_4$ is again a combination band requiring mode coupling while the $\nu_2 + \nu_4 \rightarrow \nu_4$ and the Raman transition $\nu_4 \rightarrow g$ are transitions with $\Delta\nu_2 = -1$ and $\Delta\nu_4 = -1$ that do not require mode coupling. The

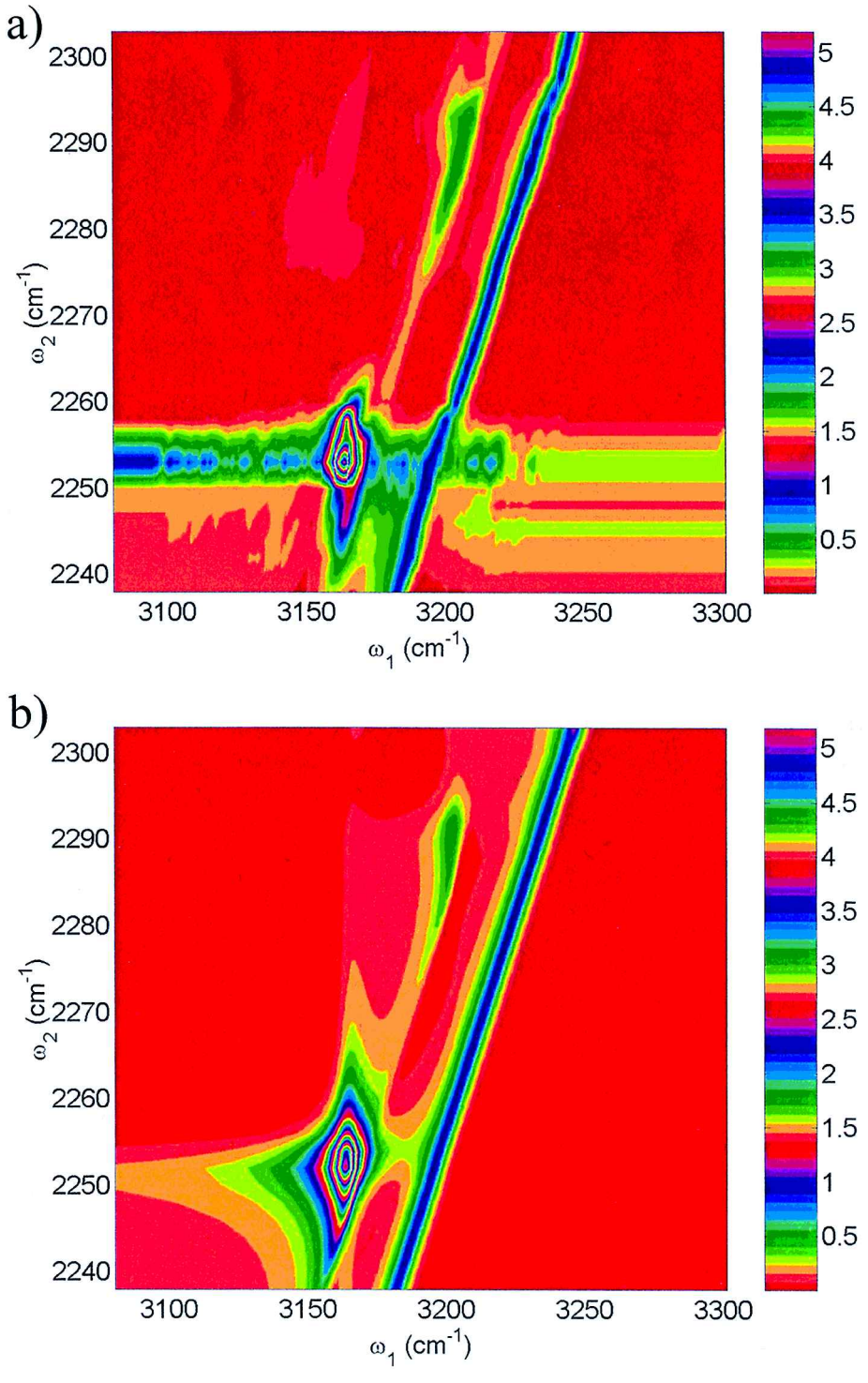

Figure 22. Contour plots of the (*a*) experimental and (*b*) the theoretical 2D DOVE FWM spectrum of acetonitrile–deuterobenzene as a function of the two infrared excitation frequencies. The four-cycle colour bar indicates the signal intensity.

last two transitions are very similar to the DOVE IR transitions and differ only in the initial and final states. One would therefore expect that DOVE IR and DOVE Raman processes would have similar intensities and would differ only because of the differences in transition moments that result from the anharmonicity differences associated with the initial state.

Similar arguments apply to the other features in the spectrum. The DOVE IR peak at $(\omega_1, \omega_2) = (\omega_{\nu_3+2\nu_4}, \omega_{\nu_3+\nu_4})$ in figure 22(*a*) requires the two infrared transitions $g \rightarrow \nu_3 + 2\nu_4$ and $g \rightarrow \nu_3 + \nu_4$ and the Raman transition $\nu_3 + 2\nu_4 \rightarrow \nu_3 + \nu_4$. The $g \rightarrow \nu_3 + 2\nu_4$ and the $g \rightarrow \nu_3 + \nu_4$ transitions are both combination bands requiring mode coupling between the C–H band and the C–C stretch while the $\nu_3 + 2\nu_4 \rightarrow \nu_3 + \nu_4$ Raman transition is allowed since $\Delta\nu_4 = -1$. The corresponding DOVE Raman peaks require the two infrared transitions $g \rightarrow \nu_3 + 2\nu_4$ and $\nu_3 + 2\nu_4 \rightarrow \nu_4$ and the Raman transition $\nu_4 \rightarrow g$. The $g \rightarrow \nu_3 + 2\nu_4$ and $\nu_3 + 2\nu_4 \rightarrow \nu_4$ are again IR combination bands requiring mode coupling while the $\nu_4 \rightarrow g$ Raman transition is allowed because $\Delta\nu_4 = -1$.

The states that are required for DOVE IR and DOVE Raman processes can be visualized using the diagrams in figures 23 and 24 [143]. Here, the vibrational quantum numbers for two coupled modes are plotted and arrows indicate the quantum number changes for each transition. The full arrows indicate ket-side transitions and the dotted arrows indicate bra-side transitions. A square designates the initial state. For example, the main acetonitrile DOVE IR peak that corresponds to the transitions $g \rightarrow \nu_2 + \nu_4$, $g \rightarrow \nu_2$ and $\nu_2 + \nu_4 \rightarrow \nu_2$ is visualized by case 1 in DOVE IR where mode 1 corresponds to ν_2 and mode 2 corresponds to ν_4. The corresponding DOVE Raman process involving the transitions $g \rightarrow \nu_2 + \nu_4$, $\nu_2 + \nu_4 \rightarrow \nu_4$ and $\nu_4 \rightarrow g$ is visualized by case 1 in figure 24. Similarly, the DOVE IR and DOVE Raman for the peak at $(\omega_1, \omega_2) = (\omega_{\nu_3+2\nu_4}, \omega_{\nu_3+\nu_4})$ corresponds to case 4 in figures 23 and 24. Vertical and horizontal lines that change by $\Delta\nu = \pm 1$ are

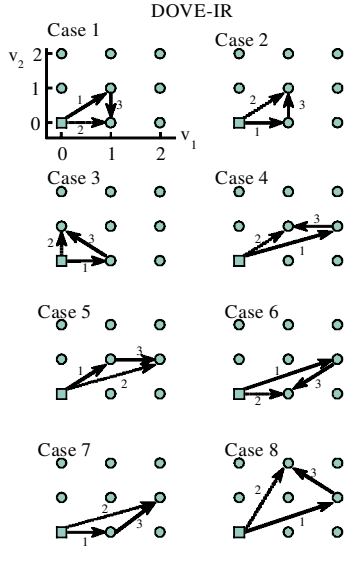

Figure 23. The arrows show different examples of the possible changes in the two vibrational quantum numbers, ν_1 and ν_2, that occur during the four transitions in a DOVE IR FWM experiment. Reproduced with permission from reference [143].

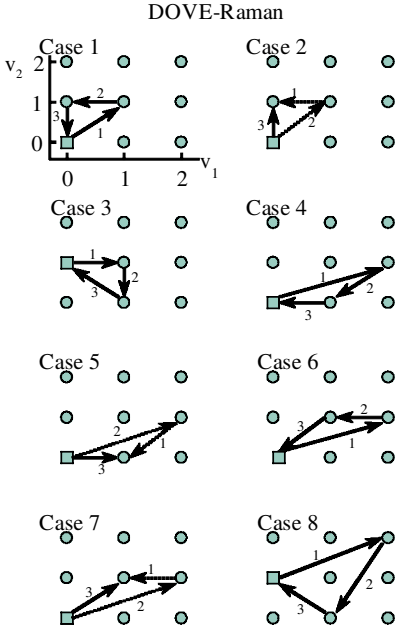

Figure 24. The arrows show different examples of the possible changes in the two vibrational quantum numbers, ν_1 and ν_2, that occur during the four transitions in a DOVE Raman FWM experiment. Reproduced with permission from reference [143].

allowed transitions and diagonal lines are combination bands requiring mode coupling. Diagonal lines with positive slopes are double or triple quantum transitions and diagonal lines with negative slopes are zero quantum transitions. Energy conservation requires the arrows to form a closed figure.

The diagrams also predict that DOVE IR and DOVE Raman are not always observed together. For example, the DOVE Raman case 3 and case 8 require excited vibrational populations so DOVE Raman will not appear with the DOVE IR feature for these cases. It is also possible to draw a case 3 and case 8 diagram for DOVE Raman that begins from the ground state and requires an initially excited vibrational state for the corresponding DOVE IR process. In this case, one would observe the DOVE Raman feature but not the DOVE IR feature (assuming the excited vibrational state was not populated).

(3) *Component selectivity*. An important capability of CMDVS is the ability to enhance selectively specific components, isotopomers, conformers and isomers. In order to test this capability, a DOVE FWM experiment was performed with a mixture of acetonitrile, deuteroacetonitrile and deuterobenzene. The deuterobenzene was again an internal standard. Figure 25 shows the infrared and Raman spectra of an equal molar CH_3CN–CD_3CN mixture. Table 1 summarizes the modes and line positions. The Raman spectrum shows that there are two C≡N stretch modes separated by $9\,cm^{-1}$. The coherent 2D DOVE FWM spectrum is shown in figure 26 [201]. In addition to the same features that were observed in figure 22, there is an additional DOVE IR peak at $(\omega_1, \omega_2) = (3094, 2264)\,cm^{-1}$ corresponding to an ω_2 resonance with the CD_3CN ν_2 C≡N stretch mode and an ω_1 resonance with the $\nu_2 + \nu_4$ combination band. There is also a diagonal feature at $\omega_1 - \omega_2 = 832\,cm^{-1}$

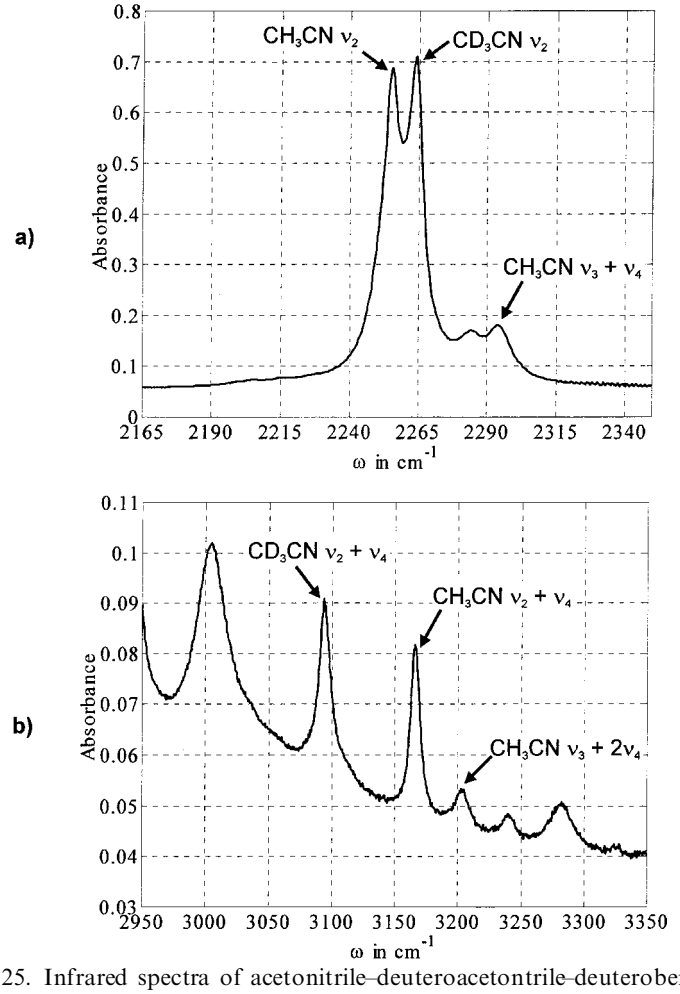

Figure 25. Infrared spectra of acetonitrile–deuteroacetontrile–deuterobenzene.

corresponding to the CD_3CN ν_4 C–C stretch mode. The high selectivity and resolution of the CH_3CN and CD_3CN isotopomer peaks in a 2D vibrational spectrum are clear from this figure.

The 2D spectrum of the mixture was modelled using equation (37). The results are shown in figure 26(*b*) [201]. Again, the simulation reproduces the general features of the spectrum.

(4) *Mode selectivity and line narrowing*. One of the most important capabilities for CMDVS is the mode selectivity that is possible. The previous discussions emphasized the importance of mode coupling for observing cross-peaks. This requirement makes CMDVS selective to modes that are interacting and insensitive to modes that are isolated. This insensitivity means that one can selectively enhance coupled modes that are obscured by stronger fundamentals which are not coupled so one can observe them, even in the presence of stronger transitions. There are three examples of this selectivity.

The first example of CMDVS mode selectivity is shown in figure 27 [201]. This spectrum was taken with the same sample as figure 26 but with an expanded range

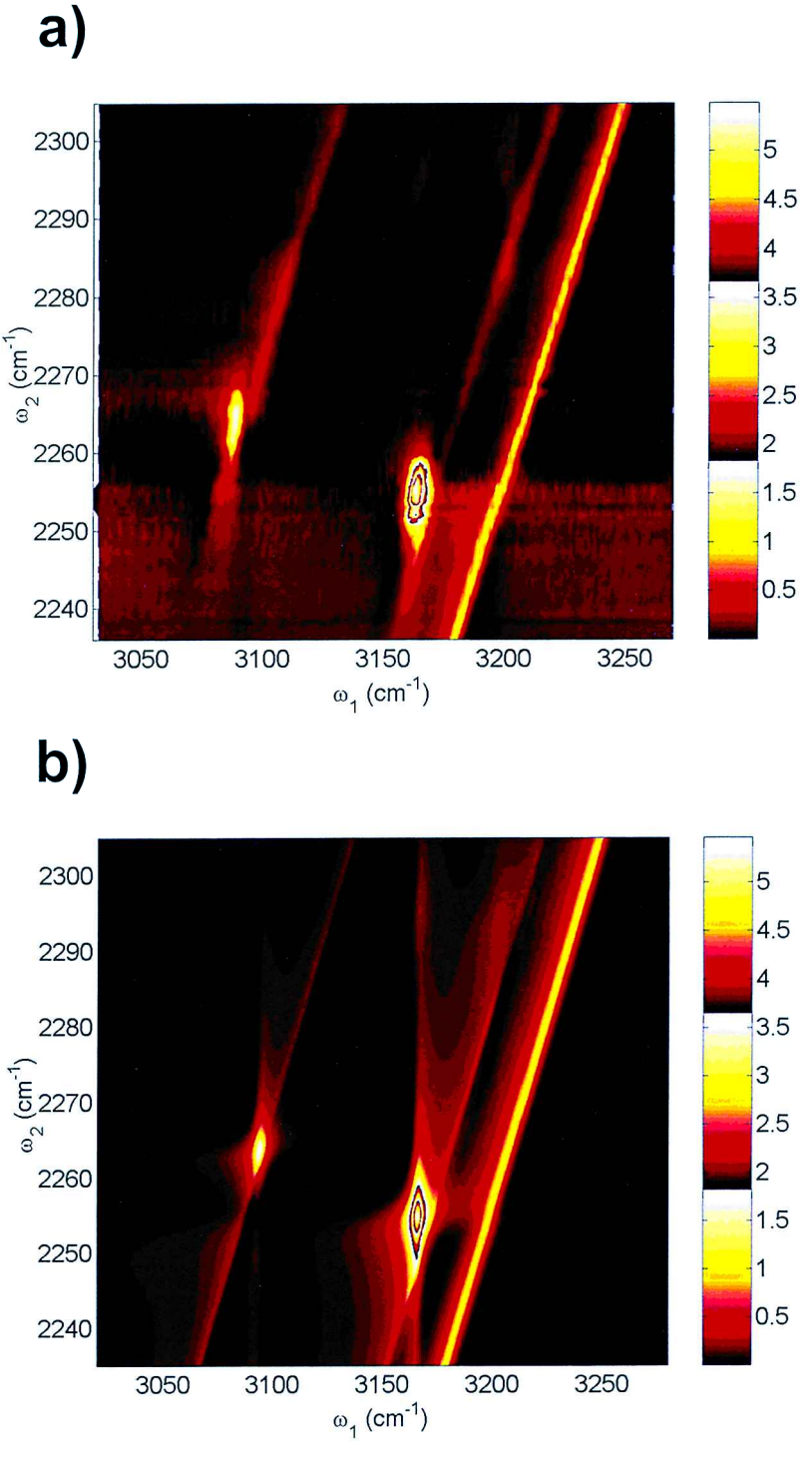

Figure 26. Contour plot of (*a*) the experimental and (*b*) the theoretical 2D DOVE FWM spectrum of acetonitrile–deuteroacetonitrile–deuterobenzene as a function of the two infrared excitation frequencies. Reproduced with permission from reference [201].

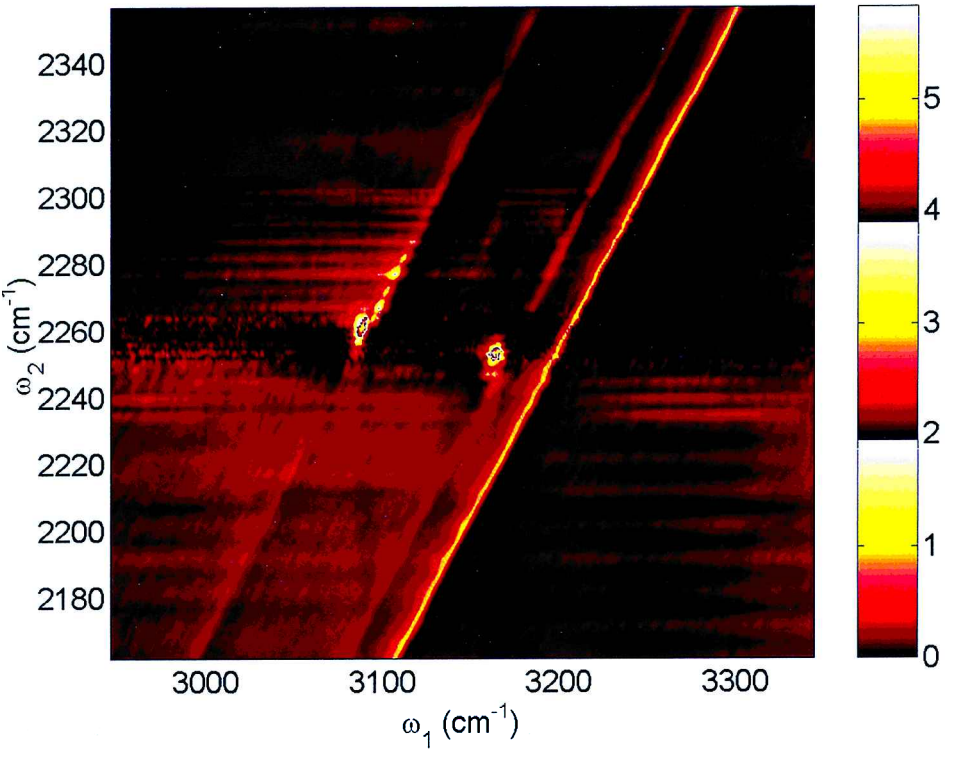

Figure 27. Contour plot of the 2D DOVE FWM spectrum of acetonitrile–deutero-acetonitrile–deuterobenzene as a function of the two infrared excitation frequencies. Reproduced with permission from reference [201].

for ω_1 and ω_2. In particular, the ω_1 range includes the region of the strong C–H stretch modes of CH_3CN. Although these modes are present at $\omega_1 = 2945$ and $3004\,cm^{-1}$, there is no indication of their presence in the 2D DOVE spectrum because they are not coupled to the ν_2 and $\nu_3 + \nu_4$ states in this range of ω_2 values.

The second example of CMDVS addresses the problem of strong solvent bands obscuring weaker solute transitions [91]. This problem is particularly severe for infrared spectroscopy of biological materials where the strong water absorption obscures the vibrational spectrum of dissolved proteins. In order to define whether CMDVS has sufficient mode selectivity to address the solvent problem, a mixture of 40:60 mol% CH_3CN–H_2O was created. The infrared spectrum of this sample is shown in figure 28(*a*). The $\nu_2 + \nu_4$ combination band is obscured by the much stronger water absorption band. It is only present as a small inflection in the expanded plot of figure 28(*a*). Nevertheless, when a DOVE FWM ω_1 scan is performed across the $\nu_2 + \nu_4$ combination band with ω_2 set for resonance with the ν_2 mode, the peak associated with the DOVE IR process emerges as seen in figure 28(*b*). There is no apparent contribution from the stronger water absorption band.

The water in the CH_3CN–H_2O mixture can form hydrogen bonds to the CH_3CN and broaden the spectrum. Thus, this sample forms a good model system for examining the line narrowing capabilities of DOVE methods [91]. The broadening can be clearly seen if the sample is changed to a 40:60 mol% CH_3CN–D_2O mixture. The water band is removed and the broadened acetonitrile $\nu_2 + \nu_4$ and $\nu_3 + 2\nu_4$

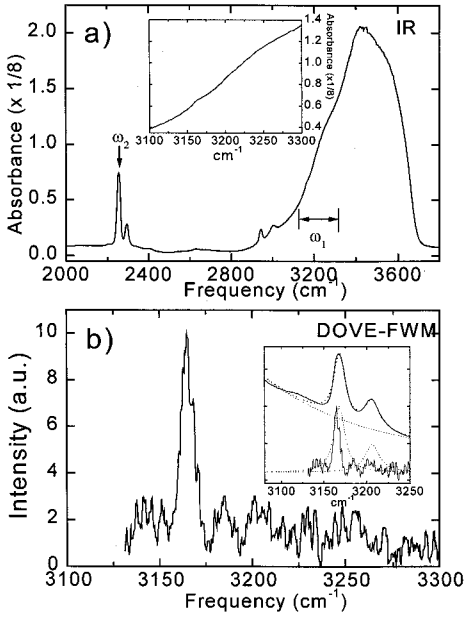

Figure 28. (*a*) The infrared absorption spectrum and an expanded view (the inset) for a 40:60 mol% CH_3CN–H_2O solution. (*b*) Spectral scan of ω_1 with ω_2 at the 2253 cm^{-1} C≡N resonance. The inset shows the line narrowing of DOVE FWM in comparison with the linewidth of the IR band. The upper full curve is the IR absorption spectrum obtained from a 40:60 mol% CH_3CN–D_2O solution. Dotted curves are decomposed from the full curve by using least-squares fitting. Reproduced with permission from reference [91].

combination bands can be seen in the inset of figure 28(*b*). The inset also shows the DOVE IR feature on the same scale. It is clearly narrower. It also shifts as a function of the ω_2 frequency. The narrowing and correlated shifting are the signatures of line narrowing where there is a selective enhancement in the non-linear polarization from the subset of doubly resonant CH_3CN molecules within the broadened distribution of CH_3CN molecules with different hydrogen-bonding environments.

The third example uses a sample that is created to have infrared absorption and Raman transitions within the same range of frequencies as the main acetonitrile DOVE IR peak [91]. Figure 29 shows the infrared, Raman and DOVE FWM spectra of a mixture of acetonitrile, deuterated acetonitrile, deuterated chloroform, tetrahydrofuran, deuterated THF, deuterobenzene and water. Table 2 summarizes the modes and frequencies for the different features in the spectra. Note that there are three overlapping modes near the acetonitrile $\omega_2 = 2253\,\text{cm}^{-1}$ C≡N stretch mode from deuterated chloroform, deuterated acetonitrile and THF-d_8 as can be seen in the inset. The $\nu_2 + \nu_4$ combination band is overlapped with the strong water O–H stretch band and the C–H stretch modes of acetonitrile and THF. The Raman spectrum has overlapping bands from the ν_4 acetonitrile and the THF ring modes. Again, the DOVE FWM spectrum contains only the DOVE IR peak from acetonitrile because the method is selective for the modes that are coupled by intra- and intermolecular interactions.

The examples given so far involve only intramolecular interactions but one of the important characteristics of CMDVS for applications will be its sensitivity to

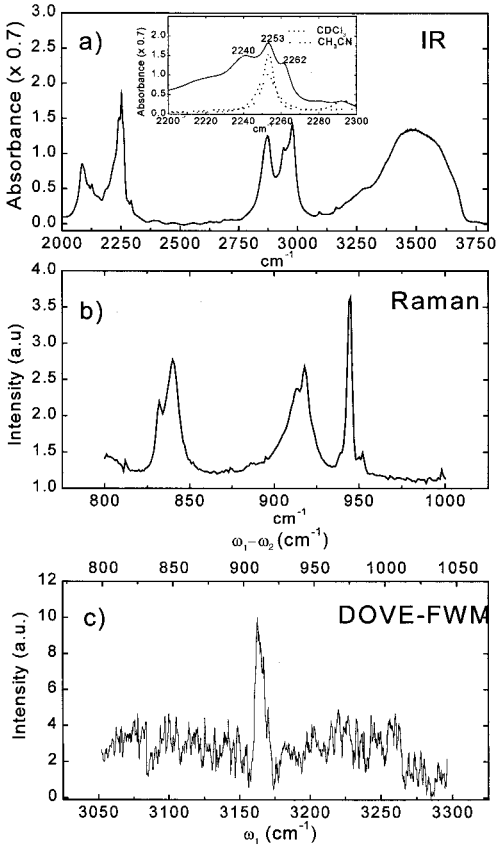

Figure 29. (*a*) The infrared absorption spectrum of a CH_3CN–CD_3CN–$CDCl_3$–THF–THF-d_8–C_6D_6–H_2O mixture. The inset shows the spectral overlap near 2253 cm^{-1}. (*b*) Spontaneous Raman spectrum of the mixture under Ar^+ laser 514.5 nm excitation. (*c*) FWM spectrum of the mixture where ω_1 is scanned while ω_2 is set at the 2253 cm^{-1} C≡N resonance of CH_3CN. The bottom axis shows ω_1 and the top axis shows $\omega_1 - \omega_2$. Reproduced with permission from reference [91].

intermolecular interactions [90, 124]. For example, it would be very interesting if one could observe the mode coupling that results from intermolecular interaction between an N–H mode in one protein and the C=O mode on another protein that was mediated by hydrogen-bonding interactions between the two. It would also be interesting to observe the intramolecular interactions that are responsible for controlling the conformation of a protein or peptide.

(5) *Temporal discrimination against non-resonant background contributions.* CMDVS is based on the multiresonant non-linear vibrational polarization but non-linear mixing will always generate a non-resonant electronic polarization that can interfere. The two polarizations have different relaxation rates. The non-resonant electronic polarization relaxes almost instantaneously on the time scale of femtosecond pulses while the vibrational polarization decays over picosecond time scales. If ultrafast pulses are used for the excitations, a time delay between the pulses discriminates against the electronic polarizations [149, 190, 202]. Figure 30 shows DOVE FWM spectra in a mixture of carbon disulphide and bromochloromethane

Table 2. Summary of the infrared absorption and Raman features of the molecules with interfering transitions in a complex test mixture.

Molecule	IR frequency (cm^{-1})	Mode	Molecule	Raman frequency (cm^{-1})	Mode
THF-d_8	2240	C–D stretch	CD_3CN	832	C–C
CH_3CN	2253	C≡N	THF-d_8	840	Ring
$CDCl_3$	2253	C–D stretch	THF	914	Ring
CD_3CN	2262	C≡N	CH_3CN	918	C–C stretch
THF	2860	C–H stretch	C_6D_6	944	Ring
CH_3CN	2945	C–H stretch			
THF	2976	C–H stretch			
CH_3CN	3004	C–H stretch			
CD_3CN	3092	C–C + C≡N			
CH_3CN	3164	C–C + C≡N			
H_2O	3350	O–H			

for different t_{12} and t_{23} time delays and pulse widths < 1 ps [202]. The ω_2 frequency was resonant with the C=S asymmetric stretch mode at 1500 cm^{-1}. Two main lines are seen at $\omega_1 = 2106$ and 2168 cm^{-1} corresponding to the bromochloromethane $\omega_1 - \omega_2 = 606\,cm^{-1}$ Raman transition and the DOVE peak from the C=S symmetric and asymmetric stretching combination band, $(\omega_1, \omega_2) = (2168, 1500\,cm^{-1})$, respectively. The spectrum in figure 30(*a*) has a strong contribution from the non-resonant electronic polarization. The spectrum in figure 30(*b*) has lost the non-resonant electronic contribution because the $t_{23} = 2$ ps delay time allows the non-resonant polarization to decay without losing an appreciable amount from the Raman and DOVE polarizations. The spectrum in figure 30(*c*) now discriminates against the Raman contribution as well because the t_{12} delay time prevents the Raman excitation but the DOVE polarization is not affected appreciably. This temporal discrimination allows one to achieve detection limits that are much lower than is possible without discrimination.

(6) *Measurement of DOVE* $\chi^{(3)}$. The size of the DOVE $\chi^{(3)}$ is of fundamental interest because it is a quantitative measure of the vibrational enhancement that results from resonances. It can then be compared with the non-resonant electronic $\chi^{(3)}$. Since the $\chi^{(3)}$ values of the deuterobenzene internal standard are known [199, 200], the relative intensities and lineshapes of the DOVE FWM features serve as the basis for finding the DOVE FWM $\chi^{(3)}$ values. This approach is an interferometric method that was first developed by Levenson and Bloembergen [199, 200], who used it to determine the non-resonant electronic non-linearity in benzene. It is based on the detailed fitting of the lineshapes that result because of the interference between two non-linearities. Figure 31 shows the concentration dependence of DOVE FWM spectra in acetonitrile samples with different deuterobenzene concentrations [90]. The spectrum in figure 31(*a*) has two lines that are the normal Raman transitions at 918 cm^{-1} and 944 cm^{-1} of acetonitrile and deuterated benzene respectively. The $\omega_2 = 2500\,cm^{-1}$ value chosen for this spectrum is far from any vibrational resonance so the two lines are not enhanced by any vibrational feature. Their relative intensities and lineshapes are characteristic of the normal CARS spectrum for this mixture. The remaining spectra are taken with $\omega_2 = 2253\,cm^{-1}$ so the main line at 3163 cm^{-1} is the DOVE IR feature. The deuterobenzene Raman line at $\omega_1 - \omega_2 = 944 cm^{-1}$

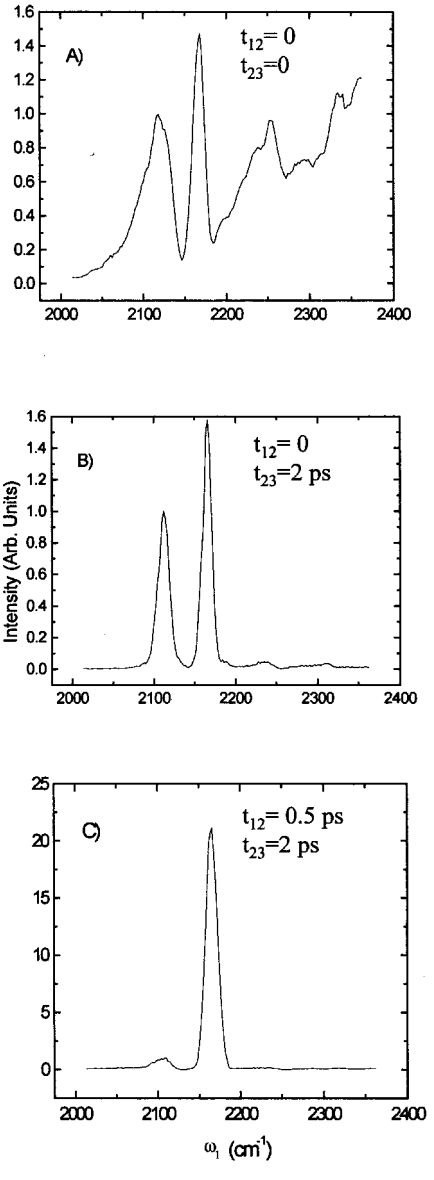

Figure 30. DOVE FWM frequency spectra as a function of delays at $\omega_2 = 1500\,\text{cm}^{-1}$. (*a*) All three beams are temporally overlapped. (*b*) The delay of ω_2 from ω_1 (delay 1) is 0.0 ps and the delay of ω_3 from ω_2 (delay 2) is +2.00 ps. (*c*) Delay 1 = +0.50 ps, delay 2 = +1.50 ps. These spectra are all scaled to the reference CARS feature at $\omega_1 = 2106\,\text{cm}^{-1}$. Reproduced with permission from reference [202].

(or $\omega_1 = 3197\,\text{cm}^{-1}$) is obscured by the much stronger DOVE IR feature. As the deuterobenzene concentration is raised, the deuterobenzene line reappears and dominates at a concentration of 29 mol% deuterobenzene.

The spectra in figure 31 can be fitted using a common set of parameters and equation (37) over the range of deuterobenzene concentrations. The detailed fitting of the relative intensities and lineshapes provides the size of each non-linearity shown in table 3 [90]. The results show that $\chi^{(3)}$ is $3.1 \times 10^{-14}\,\text{cm}^3\,\text{erg}^{-1}$ for the acetonitrlle

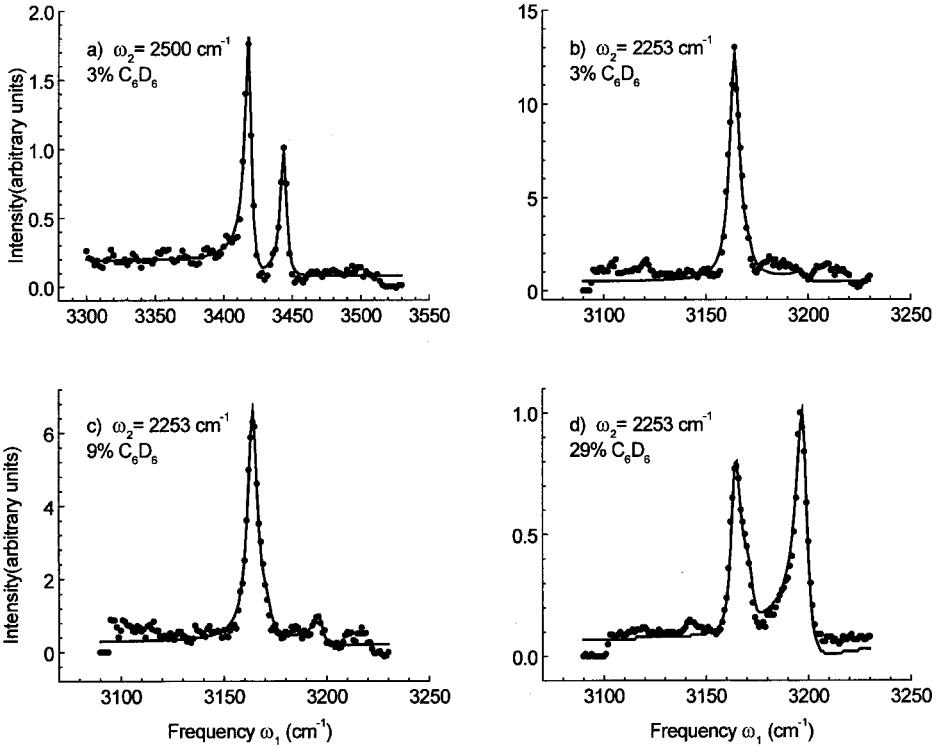

Figure 31. FWM scans of ω_1 where ω_2 and the C_6D_6 concentrations are indicated in the figure. Reproduced with permission from reference [90].

DOVE IR feature when $\omega_1 = \omega_{\nu_2+\nu_4}$ and $\omega_2 = \omega_{\nu_2}$. This value should be compared with 7.1×10^{-14} and $2.8 \times 10^{-15}\,\mathrm{cm^3\,erg^{-1}}$ for the Raman and non-resonant electronic $\chi^{(3)}$ values respectively of benzene at the frequencies of the DOVE experiments.

It is also possible to estimate the value of the DOVE IR $\chi^{(3)}$ from the absorption coefficients and the Raman $\chi^{(3)}$ of the three transitions in a DOVE FWM process [90]. The infrared absorption coefficient, Raman $\chi^{(3)}$ and DOVE $\chi^{(3)}$ are

$$\alpha_{\mathrm{v'g}} = \frac{4\pi\omega_{\mathrm{v'g}} N F_{\mathrm{v'g}} \mu^2_{\mathrm{v'g}} \rho_{\mathrm{gg}}}{hc\Gamma_{\mathrm{v'g}}}, \tag{39}$$

$$\chi^{(3)}_{\mathrm{vg,Raman}} = -\frac{\mathrm{i}NF^2_{\mathrm{eg}} F_{\mathrm{ev}} \mu^2_{\mathrm{eg}} \mu^2_{\mathrm{ev}} \rho_{\mathrm{gg}}}{4D_{\mathrm{Raman}} h^3 |\Delta_{\mathrm{eg}}|^2 \Gamma_{\mathrm{vg}}} \tag{40}$$

and

$$\chi^{(3)}_{\mathrm{DOVE}} = \frac{NF_{\mathrm{v'g}} F_{\mathrm{v''g}} F_{\mathrm{ev''}} \mu_{\mathrm{v''g}} \mu_{\mathrm{v'g}} \mu_{\mathrm{v''e}} \mu_{\mathrm{ev'}} \rho_{\mathrm{gg}}}{4D_{\mathrm{DOVE}} h^3 \Gamma_{\mathrm{v'g}} \Gamma_{\mathrm{v''g}} \Delta_{\mathrm{ev'}}} \left(1 + \frac{\Gamma^{\mathrm{g}}_{\mathrm{v''v'}}}{\Gamma_{\mathrm{v''v'}}}\right). \tag{41}$$

Combining these expressions and a similar one for $\alpha_{\mathrm{v''g}}$, we find

$$\chi^{(3)}_{\mathrm{DOVE}} = \frac{c(1 + \Gamma^{\mathrm{g}}_{\mathrm{v''v'}}/\Gamma_{\mathrm{v''v'}})}{8\pi D_{\mathrm{DOVE}}} \sqrt{\frac{\mathrm{i}F_{\mathrm{v'g}} F_{\mathrm{v''g}} D_{\mathrm{Raman}} \alpha_{\mathrm{v'g}} \alpha_{\mathrm{v''g}} \chi^{(3)}_{\mathrm{Raman}} \Gamma_{\mathrm{vg}}}{F_{\mathrm{ev'}} \omega_{\mathrm{v'g}} \omega_{\mathrm{v''g}} \Gamma_{\mathrm{v'g}} \Gamma_{\mathrm{v''g}} \rho_{\mathrm{gg}}}}, \tag{42}$$

Table 3. Parameter values required for calculating DOVE $\chi^{(3)}$ and values in the fitting routine to obain experimental values for $\chi^{(3)}$. The 944 cm^{-1} deuterobenzene $\chi^{(3)}$ is the standard and relative uncertainties on the measurements are ±20%. From reference [90].

Literature	N (cm^{-3})	F	$\varepsilon_{ba}, \varepsilon_{ca}$ ($l\,mol^{-1}\,cm^{-1}$)	Γ_{ba} (cm^{-1})	Γ_{ca} (cm^{-1})	Predicted $\chi^{(3)}$ ($cm^3\,erg^{-1}$)
CH_3CN	1.97×10^{22}	2.59	42.9, 3.16[a]	2.85[a]	4.39[b]	2.7×10^{-14}
C_6D_6	6.73×10^{21}	4.04		1.15[c]		7.1×10^{-14}

Experimental	CH_3CN DOVE	CH_3CN Raman[b]	CH_3CN NR[b]	C_6D_6 Raman[c]	C_6D_6 NR[c]	Windows[b]
$A^{b,d}$			0.013		0.04	0.012
$B/\Gamma_{ba}{}^{b,d}$		0.043		1		
$C/\Gamma_{ba}\Gamma_{ca}{}^{b,d}$	0.232					
$D/\Gamma_{ba}\Gamma_{ba}{}^{b,d}$	0.03					
Γ_{ba} (cm^{-1})	2.85[c]	2.72[d]		3.01[d]		
Γ_{ca} (cm^{-1})[d]	4.39					
ω_{ba} (cm^{-1})[d]	2253	918		944		
ω_{ca} (cm^{-1})[d]	3164					
$\chi^{(3)}$ (experiment)[d] ($cm^3\,erg^{-1}$)	3.1×10^{-14}	5.75×10^{-15}	1.7×10^{-15}	7.1×10^{-14} [e]	2.8×10^{-15} [e]	1.6×10^{-15}

[a] J. E. Bertie and Z. Lan, 1997, *J. Phys. Chem.* B, **101**, 411.
[b] W. Zhao and J. C. Wright, 1999, *phys. Rev. Lett.*, **83**, 1950.
[c] M. D. Levenson and N. Bloembergen, 1974, *J. chem. Phys.*, **60**, 1323.
[d] Peak values are normalized to the 944 cm^{-1} deuterobenzene hyperpolarizability.
[e] Published value was corrected for the frequencies used in this experiment. See M. J. LaBuda and J. C. Wright, 1998, *J. Chem. Phys.*, **108**, 4112.

where $\Gamma^{g}_{v''v'} = \Gamma_{v''v'} - \Gamma_{v'g} - \Gamma_{v''g}$, c is the speed of light, F is the local field factor, N is the number density and D is a degeneracy factor. The values used in the expression are summarized in table 3 and [90]. They give a predicted value for $\chi^{(3)}_{DOVE}$ of $2.7 \times 10^{-14}\,cm^3\,erg^{-1}$. This value is in good agreement with the measured value.

3.2.2. *Doubly vibrationally enhanced six-wave mixing (2D Raman)*

It is also possible to perform CMDVS using two Raman excitations of two modes and a probe pulse to excite the output Raman transition [72, 112]. This approach requires SWM, a higher-order non-linearity. The extension of CMDVS to higher-order non-linearities is important because it provides higher dimensionality spectroscopies that are increasingly more selective. Higher-order non-linear spectroscopies are analogous to multipulse NMR spectroscopies [187]. There are important differences between multipulse NMR and higher-order wave mixing that make the implementation more difficult. In multipulse NMR, it is easy to reach Rabi frequencies that are higher than typical relaxation times so saturation of transitions is easily accomplished and states can be decoupled. The NMR excitation wavelength is long compared with typical sample sizes so the internal fields that are launched by the sample do not perturb the experiment. On the other hand, in higher-order non-linear spectroscopy, it is difficult to saturate vibrational transitions without inducing sample damage so decoupling states is harder. In addition, the wavelength of the output fields is short compared with the typical sample thicknesses so strong internal fields created by the non-linear polarization can participate in driving further non-linearities.

The resonances and coherence pathways are shown in figure 32(*a*). A pair of pulses with $t_{12} = 0$ excites an initial vibrational coherence. After a time delay, t_{23}, a second pair of pulses with $t_{34} = 0$ excites a double quantum coherence, $\rho_{v''v'}$. After a second time delay, t_{45}, a probe pulse excites the final output coherence. The non-parametric pathways (see upper part of figure 32(*a*)) involve conjugate coherences which can rephase and line narrow if there is correlated inhomogeneous broadening. The parametric pathway (see lower part) has coherences with the same sign for the time dependence and these can rephase for modes which have anticorrelated inhomogeneous broadening.

The coherence pathways in figure 32(*a*) have a close relationship with DOVE FWM. The pathways are the same except that DOVE SWM creates the coherences via Raman transitions and the DOVE FWM creates the coherences via infrared transitions. Note also that there are both parametric and non-parametric processes for the DOVE SWM process that are analogous to the DOVE Raman FWM and DOVE IR FWM pathways respectively.

In order to observe true SWM, one must discriminate against the lower-order processes where the output from one lower-order process drives a second lower-order process [72, 78, 203]. It is often difficult to distinguish between the true SWM and the cascaded lower-order processes. Figure 32(*b*) shows the WMEL diagrams for two types of cascaded FWM processes. The cascaded processes can be sequential (left part of figure 32(*b*)) where the output from the first FWM process drives the second process (the intermediate field is shown as the connecting arrow) or a parallel cascade (right part of figure 32(*b*)) where the second FWM process occurs during the first FWM process [78, 203].

SWM and cascaded FWM have several similarities. In both cases, the output occurs at $\omega_6 = \omega_1 - \omega_2 - (\omega_3 - \omega_4) + \omega_5$, they each have a linear intensity depen-

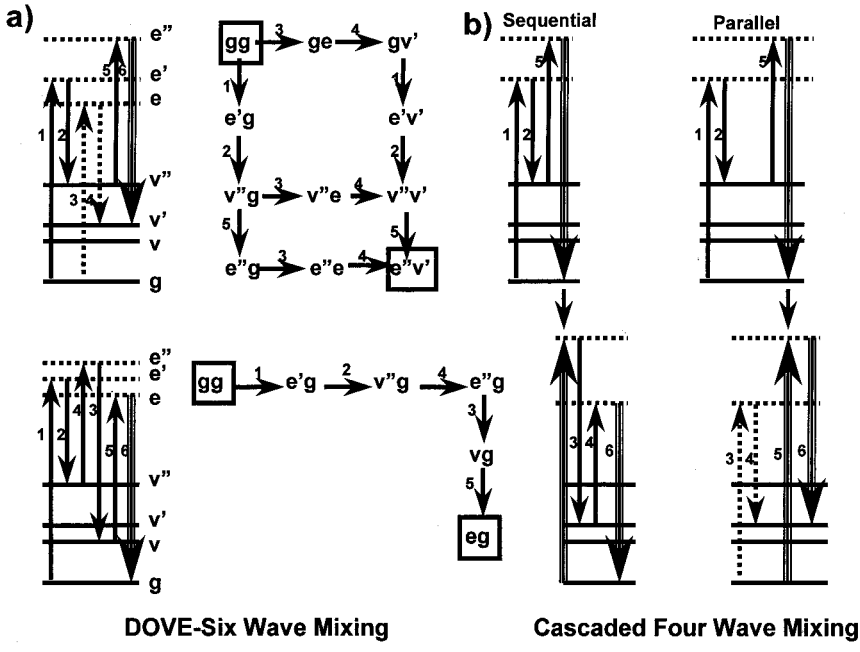

Figure 32. (*a*) WMEL and Liouville diagrams showing the resonances and the flow of coherence for example SWM processes involving three Raman transitions. (*b*) WMEL diagrams for the sequential and parallel cascaded FWM processes. The arrows connecting the upper and lower WMEL diagrams indicate the intermediate field that couples the two steps in the cascade.

dence on each excitation beam and they have the same phase matching conditions for the final output. There are also four differences that form the basis for discriminating between the cascading FWM and SWM processes. (1) The concentration and path length dependence are quartic for cascaded FWM processes and quadratic for SWM processes so lower concentrations and a shorter pathlength favour SWM. (2) The cascaded process produces an intermediate output field whose intensity depends on the phase matching used to create the intermediate field so the phase matching of the intermediate field can control the cascaded contribution. Thus one must minimize the contributions from $\boldsymbol{k}_1 - \boldsymbol{k}_2 + \boldsymbol{k}_4$ phase matching in the sequential process and $-\boldsymbol{k}_3 + \boldsymbol{k}_4 + \boldsymbol{k}_5$ phase matching in the parallel process and maximize $\boldsymbol{k}_1 - \boldsymbol{k}_2 - \boldsymbol{k}_3 + \boldsymbol{k}_4 + \boldsymbol{k}_5$ in the SWM process. (3) Each process also has a characteristic delay time dependence. The sequential cascade produces a signal that is symmetric in the t_{23} and t_{45} time delays since these delays control the intermediate coherences in the FWM processes. The parallel cascade process produces signals that are asymmetric in the time delays because the intermediate coherences depend on t_{45} and $t_{23} + t_{45}$ respectively. (4) Finally, the phase of the output from the cascaded processes is shifted by π from the SWM output [125, 157]. This difference can be the basis for discrimination if heterodyne detection is used [80, 81].

Early work used phase matching to discriminate against the sequential process but it was not realized that a parallel cascade process was also present [73, 74, 76, 77, 204–207]. The phase matching that was chosen in this earlier work was favourable for the parallel cascade so it dominated the experimental data [78].

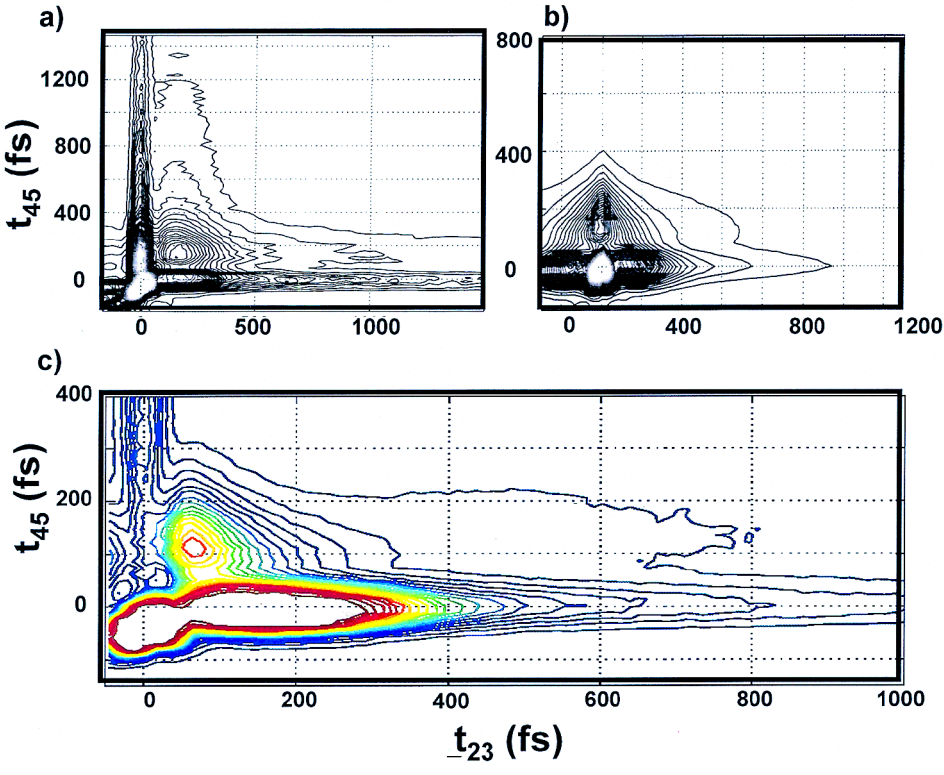

Figure 33. (*a*) Five-laser non-linear signal from carbon disulphide where the phase matching has been set to favour the sequential cascaded FWM process. (*b*) Signal where the phase matching has been set to favour the parallel cascaded FWM process. (*c*) Signal when the cascaded FWM processes are suppressed by phase matching. Reproduced with permission from reference [82].

Recent experimental work has reported successful demonstration of SWM using phase matching to discriminate against the cascaded processes [80–84]. Figure 33 shows example time domain 2D spectra for SWM experiments in carbon disulphide. Carbon disulphide has a very large electronic non-linearity and is an ideal material for studying weak non-linear processes. The experiments focus on low-energy over-damped solvent modes that can be excited by impulsive Raman pulses. Figures 33(*a*) and (*b*) show the measured spectra for phase matching conditions that emphasize the sequential and parallel cascades respectively [78]. From these spectra, one can see that the sequential cascade is symmetrical in t_{23} and t_{45} and the parallel cascade is asymmetrical. Figure 33(*c*) shows the measured spectra for phase matching conditions where the cascaded FWM is minimized by phase matching conditions that attenuate the intermediate field [82]. The spectrum is qualitatively different from the cascaded signals. The dominant feature in figure 33(*c*) is the peak at $t_{23} = 60$ fs and $t_{45} = 110$ fs. The cascaded spectra also have peaks but they are shifted. The sequential cascade has a peak at $t_{23} = t_{45} = 180$ fs and the parallel cascade has a peak at $t_{23} = 0$ fs and $t_{45} = 180$ fs. These are clearly different from the peak observed in the true SWM process. In addition, the SWM spectrum decays more quickly than either cascaded process.

The nature of the non-parametric DOVE SWM pathways (top diagrams in figure 32(*a*)) provides coherences that can rephase if there is correlated inhomogeneous broadening so that echoes can occur. Rephasing causes diagonal character in the peaks. Significantly, the data in figure 33(*c*) do not have an indication of a rephasing feature, indicating that the coherences created after the first and second Raman excitations do not have correlated dephasing dynamics [82]. There is, however, asymmetry between the t_{23} and t_{45} axes that suggests that the data are contaminated with small contributions from parallel cascaded processes [82]. The amount of cascaded contamination in figure 33(*c*) can be found by first modelling the frequency dependence expected for the cascaded processes using the known third-order response. The relative contributions from the different cascaded processes can be modelled by calculating the phase matching factors [83]. Here, one must include not only the direct contributions of the different parallel and sequential cascades but also the cross-terms between all combinations of parallel cascades, sequential cascades and SWM processes. The cross-terms are created because the electric fields from each process are additive and together determine the measured intensity.

The cascaded signals decay more slowly along the t_{23} axis than the SWM signal so it is possible to use the long-time behaviour to estimate the cascaded contribution and to subtract the contributions from the data. It is shown that the cascaded signals are only a minor contributor to the spectrum in figure 33(*c*) [83].

It is interesting to contrast these results with work by Miller and coworkers who also reported success in discriminating against the cascaded processes [80, 81]. Here, the 400 nm doubled Ti:sapphire output was used to create the first two Raman excitations and the 800 nm output created the third excitation and the local oscillator beam that was used for heterodyne detection. A diffractive optic was used to create the phase matching geometry. Two different phase matching geometries were used in the experiment—a 'baseball diamond' geometry which discriminated against the sequential cascaded FWM processes and a 'crossed' geometry which discriminated against both cascaded processes. Each geometry had a different efficiency for measuring the SWM and cascaded FWM signals. The baseball geometry had the signature of the parallel cascaded FWM processes. The crossed geometry eliminated the parallel cascaded processes. After the phase matching discrimination, the remaining signal was markedly different from that expected for cascaded processes so the signal appears to correspond to true SWM.

If one compares the 2D time-dependent data between the two groups, one finds different dependences on the delay times [80–84]. The disagreement indicates either that the experimental differences in the two approaches produce different results or that there are still unknown factors that prevent a definitive observation of true SWM spectra.

Calculations have also been performed to predict the relative size of SWM and cascaded FWM processes. These calculations find that the cascaded intensity should be 2×10^6 larger than the SWM intensity [208]. This factor is so large that it would prevent one from observing SWM but, in fact, SWM was reported with a discrimination factor of only 10^2–10^3 against the cascaded processes. This discrepancy has not yet been resolved [84] but it is important to know the size of the SWM signal and whether it is feasible to discriminate against interfering signals.

4. The future of CMDVS

4.1. *Femtosecond time domain CMDVS*

CMDVS is very much in its infancy. The potential for CMDVS applications rests with improvements in the technology, improvements in our understanding of the spectroscopy and improvements in the theory that relates the spectroscopy to structure. Frequency domain experiments have provided the first insights into CMDVS involving two different modes but frequency domain approaches are limited because the narrow bandwidth excitation that is required for frequency domain experiments necessarily demands longer pulse widths. Longer pulse widths prevent temporal discrimination against non-resonant electronic background so the detection limits are constrained. The ultrafast excitation pulses of time domain methods do allow temporal discrimination against non-resonant backgrounds. In addition, the higher damage threshold of an ultrafast excitation allows one to work at higher peak intensities so the signal levels are markedly higher. Thus, it seems clear that the future of CMDVS lies with time domain spectroscopy with femtosecond excitation pulses.

Time domain spectroscopy must resolve the phase of an oscillating vibrational coherence, either by heterodyne detection with a local oscillator or by sufficiently short excitation pulses. Currently, infrared excitation pulses do not have short enough pulse widths to resolve directly vibrational coherences at the frequencies commonly used for vibrational spectroscopy so heterodyning with a local oscillator is the current method of choice.

A new way to perform CMDVS experiments combines HSPE and DOVE IR/Raman methods into a method that has characteristics of each. The resonances and coherent pathways of this approach are diagrammed in figure 34(*a*). Two independently tunable excitation sources excite two different but coupled modes and the output occurs at the same frequency as an excitation. There are multiple TRIVE pathways that interfere in ways that are analogous to the HSPE and DOVE IR/Raman methods. The transitions can all be allowed $\Delta v = \pm 1$ fundamental transitions. Cross-peaks are not observed in the absence of coupling because the pathways that involve fundamentals destructively interfere with the pathways that involve the combination band. The cross-peaks appear if coupling causes anharmonic shifts, changes in the transition moments or changes in the relaxation dynamics.

4.2. *Surface-selective odd wave mixing CMDVS*

There is also great interest in developing odd-wave mixing CMDVS methods that are surface selective [134, 161] and/or chirally specific [17]. Two examples of five-wave mixing are shown in figure 34(*b*) but there are many other potential methods that are not shown. In the first, two coupled vibrational modes are excited by an infrared absorption and a Raman excitation (indicated on the Liouville diagram by fields 2 and 3 interacting simultaneously) and the output occurs because of a Raman combination band between the two modes. In the second, the two modes are excited by direct infrared transitions and the output occurs as a hyper-Raman combination band (indicated by the simultaneous two-photon absorption involving fields 3 and 4 and an output of field 5). In both examples, the cross-peaks require coupling that creates a combination band.

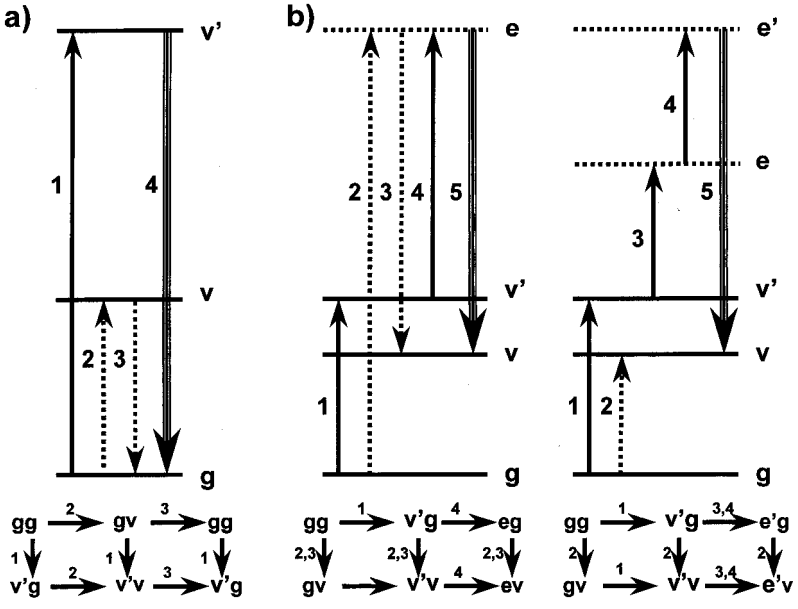

Figure 34. (*a*) WMEL and Liouville diagrams for hybrid DOVE process where two vibrational modes are excited and the output has the same frequency as one of the input frequencies. (*b*) WMEL and Liouville diagrams for CMDVS five-wave mixing methods that will be surface selective.

4.3. *Coherent control and CMDVS*

There are close connections between the ideas of CMDVS and the coherent control of chemical reactions. In CMDVS, a series of excitation pulses create a series of coherences over a particular pathway and the coherences' frequencies are measured by time or frequency domain methods. In coherent control, the temporal profile of the excitation pulse(s) also drives a series of coherences over a pathway that leads to the state of interest, for example a particular dissociative state [175, 209–218]. The temporal profile defines the instantaneous frequency and phase of the excitation field that preferentially drives one coherence pathway over others. By changing the temporal profile, one can choose different coherence pathways that lead to different reactive final states. The reaction products can include ones that are not accessible from thermal reactions.

A clever approach for optimizing particular pathways rests on manipulating the coherence pathway by a genetic learning algorithm that mutates the temporal profile while monitoring a specific reaction product or outcome [211–213]. Mutations that improve the outcome are kept and ones that degrade the outcome are rejected. The learning process is continued until the system evolves to an optimized outcome. The temporal profile is controlled by dispersing an ultrafast excitation pulse with a grating into the wide band of frequencies that are expected from the time–bandwidth product. A programmable mask modifies the phase of particular frequencies within the dispersed spectrum and a second grating operating with subtractive dispersion transforms the frequency distribution into a new temporally shaped pulse. The first grating performed a Fourier transform of the time domain pulse, the mask modified the frequency domain spectrum and the second grating performed an inverse Fourier

transform of the modified frequency domain spectrum into a modified and shaped pulse.

Coherent control of the dissociative photochemistry of acetophenone has been recently achieved [213]. Acetophenone has three different dissociative pathways where $C_6H_5COCH_3$ creates fragments of $C_6H_5^+$, $C_6H_5CO^+$ or $C_6H_5CH_3^+$. The last of these is not observed in electron impact ionization but is observed at high pulse intensities. The pathways are controlled by adjusting the phase and temporal profile of a 25 fs Ti:sapphire laser which is focused into the sample at an intensity of $\sim 10^{13}\,W\,cm^{-2}$. These intensities are in the strong field limit where dynamic Stark effects and higher-order non-linearities become important. The coherent control algorithm can either increase the $C_6H_5^+$:$C_6H_5CO^+$ ratio by $\sim 1.7\times$ or decrease it by $\sim 2.2\times$, depending on which product is to be optimized. It can also increase the $C_6H_5CH_3{}^+$ product yield by $\sim 4\times$ if that fragment is to be optimized.

In addition to dissociative reactions, coherent control of atomic and molecular state populations has been demonstrated so one can control the spectra that one observes [175, 214, 215, 219, 220]. Similar methods should be capable of controlling electron transfer reactions and H bonding interactions. Coherent control experiments have not yet been performed with infrared lasers that can drive vibrational coherences but these offer a complementary approach to control methods that utilize the electronic states. In addition, CMDVS and coherent control are compatible technologies so it will be very interesting to combine the methods. Either one can control the CMDVS spectra that are measured or one can measure the species that are generated in the coherent control process.

4.4. *CMDVS Imaging microscope*

Vibrational spectroscopic imaging methods have generated a great deal of interest because they can provide spectroscopic contrast for particular chemical moieties [221, 222]. Vibrational imaging can be performed with either infrared or Raman spectroscopy. The spatial resolution of infrared imaging is limited because the diffraction limit for a focused infrared beam is large. The spatial resolution of Raman imaging, however, is much better because the excitation beam has a much shorter wavelength.

Recently, there has been interest in extending vibrational imaging methods using non-linear methods [223, 224]. Volkmer *et al.* used CARS to perform Raman scattering microscopy. Since the spatial scale of features in the image was comparable with the wavelength of the excitation beams, the Δk values in the phase matching equation are small so the output is not constrained to a narrow beam as it is in most non-linear methods [223, 224]. Consequently, epi-detection was used where $NA = 1.4$ microscope objectives focused the excitation beams and collected the output signal over a large solid angle. This approach provided spatial resolution of ~ 500 nm and spectroscopic contrast from the C–O stretching frequency of DNA [223].

This approach can be used for any non-linear method including CMDVS methods. For example, in DOVE IR, it would be necessary to focus two infrared and one UV/visible beam with a microscope objective and to detect the output with a second microscope objective. The spatial resolution would be determined by the shortest wavelength excitation beam, in this case the UV/visible excitation, so the spatial resolution would inherently be much larger than that obtainable with all

infrared beams. The spectral contrast should be quite high because of the multi-dimensional capabilities of CMDVS.

4.5. *Near-field microscopy with probe enhancement*

The spatial resolution of near-field microscopy can be reduced to $\sim$10 nm using probe enhancements [225]. It is well known that the electric fields near a sharp metal tip are enhanced by $\sim$1000$\times$. Experiments have shown that this effect can be used in conjunction with a near-field microscope to enhance the spatial resolution [225]. A laser is first tightly focused in the near field to an area of $\sim 10^5$ nm^2. A sharp metal tip is then brought within 2 nm of this region in order to enhance the fields. The area that is enhanced by the sharp metal tip is $\sim 10^2$ nm^2. In order to achieve enhanced spatial resolution, it is necessary that the enhancement in the signal dwarfs the signal from the focal region. Since the ratio of the areas is 10^{-3} and the expected enhancement is 10^3, the enhancement is not adequate to result in improved spatial resolution. However, a two-photon excited fluorescence involves two fields so the enhancement is 10^6. This enhancement is adequate for achieving improved spatial resolution. In fact, these experiments have shown that one can create an image with 15 nm spatial resolution using two-photon excited fluorescence [225]. The extension to FWM and higher-order non-linear spectroscopies should permit an even larger enhancement of the signals because of the higher-order dependence on the electric fields.

Acknowledgments

This work was supported by the Analytical and Surface Science Program of the Chemistry Division of the National Science Foundation under grant CHE-0130947.

References

[1] Wright, J. C., LaBuda, M. J., Thompson, D. E., Lascola, R., and Russell, M. W., 1996, *Anal. Chem.*, **68**, 600A–607A.
[2] Mukamel, S., 1995, *Principles of Nonlinear Optical Spectroscopy*, 1st edn (New York: Oxford University Press).
[3] Shen, Y. R., 1984, *The Principles of Nonlinear Optics* (New York: Wiley Interscience).
[4] Wright, J. C., Carlson, R. J., Hurst, G. B., Steehler, J. K., Riebe, M. T., Price, B. B., Nguyen, D. C., and Lee, S. H., 1991, *Int. Rev. phys. Chem.*, **10**, 349–390.
[5] Kirkwood, J. C., Ulness, D. J., and Albrecht, A. C., 2000, *J. phys. Chem.* A, **104**, 4167–4173.
[6] Bishop. D. M., and Dalskov, E. K., 1996, *J. chem. Phys.*, **104**, 1004–1011.
[7] LaBuda, M. J., and Wright, J. C., 1997, *Phys. Rev. Lett.*, **79**, 2446–2450.
[8] LaBuda, M. J., and Wright, J. C., 1998, *J. chem. Phys.*, **108**, 4112–4122.
[9] Gallagher,. S. M., Albrecht, A. W., Hybl, J. D., Landin, B. L., Rajaram, B., and Jonas, D. M., 1998, *J. Opt. Soc. Am.* B, **15**, 2338–2345.
[10] Hybl, J. D., Albrecht, A. W., Gallagher Faeder, S. M., and Jonas, D. M., 1998, *Chem. Phys. Lett.*, **297**, 307–313.
[11] Hamm, P., Lim, M., DeGrado, W. F., and Hochstrasser, R. M., 1999, *J. phys. Chem.* A, **103**, 10049–10053
[12] Zanni, M. T., Asplund, M. C., and Hochstrasser, R. M., 2001, *J. chem. Phys.*, **114**, 4579–4590.
[13] Schultz, M. J., Schnitzer, C., Simonelli, D., and Baldelli, S., 2000, *Int. Rev. Phys. Chem.*, **19**, 123–153.
[14] Corn, R. M., and Higgins, D. A., 1994, *Chem. Rev.*, **94**, 107–125.
[15] Huang, J. Y., and Shen, Y. R., 1994, *Phys. Rev.*, **49**, 3973–3891.
[16] Corn, R. M., 1991, *Anal. Chem.*, **63**, 285A–292A.

[17] Fisher, P., and Albrecht, A. C., 0000, *J. chem. Phys.* (to be published).
[18] Smith, P. W., and Hansch, T. W., 1971, *Phys. Rev. Lett.*, **26**, 740–743.
[19] Haroche, S., and Hartmann, F., 1972, *Phys. Rev.* A, **6**, 1280.
[20] Chebotayev, V. P., and Letokhov, V. S., 1977, *Prog. quant. Opt.*, **4**, 111–206.
[21] Hansch, T. W., 1977, Nonlinear high resolution spectroscopy of atoms and molecules, in *Nonlinear Optics*, 1st edn, edited by N. Bloembergen (Amsterdam: North-Holland), pp. 17–86.
[22] Patel, C. K. N., 1974, *Appl. Phys. Lett.*, **25**, 112–114.
[23] Szabo, A., 1970, *Phys. Rev. Lett.*, **25**, 924–926.
[24] Flach, R., Hamilton, D. S., Selzer, P. M., and Yen, W. M., 1975, *Phys. Rev. Lett.*, **35**, 1034–1037.
[25] Marchetti, A. P., McColgin, W. C., and Eberly, J. H., 1975, *Phys. Rev. Lett.*, **35**, 387–390.
[26] Everly, J. H., McColgin, W. C., Kawaoka, K., and Marchetti, A. P., 1974, *Nature*, **251**, 215–217.
[27] McColgin, W. C., Marchetti, A. P., and Eberly, J. H., 1978, *J. Am. Chem. Soc.*, **100**, 5622–5626.
[28] Brown, J. C., Duncanson, J. A., and Small, G. J., 1980, *Anal. Chem.*, **52**, 1711.
[29] Jankowiak, R., and Small, G. J., 1989, *Anal. Chem.*, **61**, 1023A.
[30] Abram, I. I., Auerbach, R. A., Birge, R. R., Kohler, B. E., and Stevenson, J. M., 1975, *J. chem. Phys.*, **63**, 2473–2478.
[31] Greisser, H. J., and Wild, U., 1980, *J. chem. Phys.*, **73**, 4715–4719.
[32] Wright, J. C., 1982, Applications of lasers in analytical chemistry, in *Applications of Lasers to Chemical Problems*, 1st edn, edited by T. R. Evans (New York: Wiley), p. 35.
[33] Burland, D. M., and Haarer, D., 1979, *IBM J. Res. Dev.*, **23**, 534.
[34] Small, G. J., 1983, Persistent nonphotochemical hole-burning and dephasing of impurity electronic transitions in glasses, in *Spectroscopy and Excitation Dynamics of Condensed Molecular Systems*, 1st edn, edited by V. M. Granovich and R. M. Hochstrasser (New York: North-Holland), p. 515.
[35] Moerner, W. E. (editor), 1988, *Persistent Spectral Hole Burning: Science and Applications* (New York: Springer).
[36] Shu, L., and Small, G. J., 1990, *Chem. Phys.*, **141**, 447–455.
[37] Lee, H. W. H., Walsh, C. A., and Fayer, M. D., 1985, *J. chem. Phys.*, **82**, 3948.
[38] Wild, U. P., Bucher, S. E., and Burkhalted, F. A., 1985, *Appl. Opt.*, **24**, 1526–1530.
[39] Thijssen, H. P. H., and Volker, S., 1986, *J. chem. Phys.*, **85**, 785.
[40] Hayes, J. M., Stout, R. P., and Small, G. J., 1981, *J. chem. Phys.*, **74**, 4266–4275.
[41] Fearey, B. L., Carter, T. P., and Small, G. J., 1983, *J. phys. Chem.*, **87**, 3590–3592.
[42] Thijssen, H. P. H., Van Den Berg, R. E., and Volker, S., 1983, *Chem. Phys. Lett.*, **103**, 23–28.
[43] Tallant, D. R., and Wright, J. C., 1975, *J. chem. Phys.*, **63**, 2075–2085.
[44] Jouart, J. P., Bissieux, C., Mary, G., and Egee, M., 1985, *J. Phys.* C, **18**, 1539.
[45] Jankowiak, R., Small, G. J., Nishimoto, M., Varanasi, U., Kim, S. K., and Geacintov, N. E., 1990, *J. pharm. biomed. Anal.*, **8**, 113–121.
[46] DeCola, P. L., Andrews, J. R., Hochstrasser, R. M., and Trommsdorff, H. P., 1980, *J. chem. Phys.*, **73**, 4695–4696.
[47] Hochstrasser, R. M., Meredith, G. R., and Trommsdorff, H. P., 1980, *J. chem. Phys.*, **73**, 1009–1019.
[48] Andrews, J. R., and Hochstrasser, R. M., 1981, *Chem. Phys. Lett.*, **83**, 427–431.
[49] Lee, S. H., Steehler, J. K., Nguyen, D. C., and Wright, J. C., 1985, *Appl. Spectrosc.*, **39**, 243–253.
[50] Nguyen, D. C., and Wright, J. C., 1985, *Appl. Spectrosc.*, **39**, 230–243.
[51] Nguyen, D. C., and Wright, J. C., 1985, *Chem. Phys. Lett.*, **117**, 224–228.
[52] Steehler, J. K., and Wright, J. C., 1985, *J. chem. Phys.*, **83**, 3200–3208.
[53] Steehler, J. K., and Wright, J. C., 1985, *J. chem. Phys.*, **83**, 3188–3199.
[54] Steehler, J. K., and Wright, J. C., 1985, *Chem. Phys. Lett.*, **115**, 486–491.
[55] Chang, T. C., Johnson, C. K., and Small, G. J., 1985, *J. phys. Chem.*, **89**, 2984–2992.
[56] Wright, J. C., Carlson, R. J., Riebe, M. T., Steehler, M. T., Nguyen, D. C., Lee, S. H., Price, B. B., and Hurst, G. B., 1989, Fully resonant nondegenerate nonlinear

mixing spectroscopy, in *Vibrational Spectroscopy and Structure*, 1st edn, Vol. 17B, edited by H. D. Bist, J. R. Durig and J. F. Sullivan (Amsterdam: Elsevier), pp. 123–158.
[57] Riebe, M. T., and Wright, J. C., 1987, *Chem. Phys. Lett.*, **138**, 565–570.
[58] Riebe, M. T., and Wright, J. C., 1988, *J. chem. Phys.*, **88**, 2981–2994.
[59] Hurst, G. B., and Wright, J. C., 1997, *J. chem. Phys.*, **95**, 1479–1486.
[60] Hurst, G. B., and Wright, J. C., 1992, *J. chem. Phys.*, **97**, 3940–3949.
[61] Carlson, R. J., Nguyen, D. C., and Wright, J. C., 1990, *J. chem. Phys.*, **92**, 1538–1546.
[62] Carlson, R. J., and Wright, J. C., 1990, *J. chem. Phys.*, **92**, 5186–5195.
[63] Carlson, R. J., and Wright, J. C., 1990, *J. chem. Phys.*, **93**, 2205–2216.
[64] Carlson, R. J., and Wright, J. C., 1991, *Anal. Chem.*, **63**, 1449–1451.
[65] Richmond, G. L., 2001, *Annu. Rev. phys. Chem.*, **52**, 257–265.
[66] Walker, R. A., Smiley, B. E., and Richmond, G. L., 1999, *Spectroscopy*, **14**, 18.
[67] Gragson, D. E., and Richmond, G. L., 1999, *J. phys. Chem.*, **102**, 3861.
[68] Richmond, G. L., 1997, *Anal. Chem.*, **69**, 537A.
[69] Du, Q., Freysz, E., and Shen, Y. R., 1994, *Science*, **264,** 826–828.
[70] Zimdars, D., Tokmakoff, A., Chen, S., Greenfield, S. R., Fayer, M. D., Smith, T. I., and Schwettman, H. A., 1993, *Phys. Rev. Lett.*, **70**, 2718–2722.
[71] Rella, C. W., Kwok, A., Rector, K., Hill, J. R., Schwettman, H. A., Dlott, D. D., and Fayer, M. D., 1996, *Phys. Rev. Lett.*, **77**, 1648–1652.
[72] Ivanecky, J. E., and Wright, J. C., 1993, *Chem. Phys. Lett.*, **206**, 437–444.
[73] Tominaga, K., Keogh, G. P., Naitoh, Y., and Yoshihara, K., 1995, *J. Raman Spectrosc.*, **26**, 495–501.
[74] Steffen, T., and Duppen, K., 1996, *Phys. Rev. Lett.*, **76**, 1224–1227.
[75] Steffen, T., and Duppen, K., 1997, *J. chem. Phys.*, **106**, 3854–3864.
[76] Tokmakoff, A., Lang, M. J., Larsen, D. S., Fleming, G. R., Chernyak, V., and Mukamel, S., 1997, *Phys. Rev. Lett.*, **79**, 2702–2705.
[77] Tokmakoff, A., and Fleming, G. R., 1997, *J. chem. Phys.*, **106**, 2569–2582.
[78] Blank, D. A., Kaufman, L. J., and Fleming, G. R., 1999, *J. chem. Phys.*, **111**, 3105–3114.
[79] Kirkwood, J. C., Ulness, D. J., Albrecht, A. C., and Stimson, M. J., 1998, *Chem. Phys. Lett.*, **293**, 417–422.
[80] Astinov, V., Kubarych, K. J., Milne, C. J., and Miller, R. J. D., 2000, *Chem. Phys. Lett.*, **327**, 334–342.
[81] Astinov, V., Kubarych, K. J., Milne, C. J., and Miller, R. J. D., 2000, *Opt. Lett.*, **25**, 853–855.
[82] Blank, D. A., Kaufman, L. J., and Fleming, G. R., 2000, *J. chem. Phys.*, **13**, 771–778.
[83] Kaufman, L. J., Blank, D. A., and Fleming, G. R., 2001, *J. chem. Phys.*, **114**, 2312–2332.
[84] Kaufman, L. J., Heo, J., Fleming, G. R., Sung, J., and Cho, M., 2001, *Chem. Phys.*, **266**, 251–271.
[85] Zilian, A., LaBuda, M. J., Hamilton, J. P., and Wright, J. C., 1994, *J. Lumin.*, **60 & 61**, 655–657.
[86] Zilian, A., LaBuda, M. J., Hamilton, J. P., and Wright, J. C., 1994, *J. Lumin.*, **60 & 61**, 410–412.
[87] Wright, J. C., Chen, P. C., Hamilton, J. P., Zilian, A., and LaBuda, M. J., 1997, *Appl. Spectrosc.*, **51**, 949–958.
[88] Hamilton, J. P., LaBuda, M. J., and Wright, J. C., 1997, *Chem. Phys. Lett.*, **277**, 175–182.
[89] Chen, P. C., Hamilton, J. P., Zilian, A., LaBuda, M. J., and Wright, J. C., 1998, *Appl. Spectrosc.*, **52**, 380–392.
[90] Zhao, W., and Wright, J. C., 1999, *Phys. Rev. Lett.*, **83**, 1950–1953.
[91] Zhao, W., and Wright, J. C., 1999, *J. Am. Chem. Soc.*, **121**, 10994–10998.
[92] Zhao, W., and Wright, J. C., 2000, *Phys. Rev. Lett.*, **84**, 1411–1414.
[93] Shoemaker, R. L., 1978, Coherent transient infrared spectroscopy, in *Laser and Coherence Spectroscopy*, 1st edn, edited by J. I. Steinfeld (New York: Plenum).

[94] Mossberg, T., Flusberg, A., Kachru, R., and Hartman, S. R., 1977, *Phys. Rev. Lett.*, **34**, 1523–1527.
[95] Brewer, R. G., and Shoemaker, R. L., 1972, *Phys. Rev.* A, **6**, 2001.
[96] Brewer, R. G., 1972, *Science*, **178**, 247.
[97] Brewer, R. G., and Shoemaker, 1977, *Phys. Rev. Lett.*, **27**, 631–634.
[98] Jurnit, N. A., Abella, I. D., and Hartman, S. R., 1964, *Phys. Rev. Lett.*, **13**, 567–570.
[99] Chen, Y. C., Chiang, K., and Hartman, S. R., 1980, *Phys. Rev.* B, **21**, 40–47.
[100] Patel, C. K. N., and Slusher, R. E., 1968, *Phys. Rev. Lett.*, **20**, 1087–1090.
[101] Brewer, R. G., and Genack, A. Z., 1976, *Phys. Rev. Lett.*, **36**, 1959–1962.
[102] Zewail, A. H., Orlowski, T. E., Jones, K. E., and Godari, D. E., 1977. *Chem. Phys. Lett.*, **48**, 256–261.
[103] Zewail, A. H., Orlowski, T. E., and Dawson, D. R., 1976, *Chem. Phys. Lett.*, **44**, 379.
[104] Keusters, D., Tan, H. S., and Warren, W. S., 1999, *J. phys. Chem.* A, **103**, 10369–10380.
[105] Scheurer, C., and Mukamel, S., 2001, *J. chem. Phys.*, **115**, 4989–5004.
[106] Hybl, J. D., Albrecht Ferro, A. A., and Jonas, D. M., 2001, *J. chem. Phys.*, **115**, 6606–6622.
[107] Hamm, P., Lim, M., DeGrado, W. F., and Hochstrasser, R. M., 1999, *Proc. Natl Acad. Sci. USA*, **96**, 2036–2041.
[108] Hamm, P., Lim, M., DeGrado, W. F., and Hochstrasser, R. M., 2000, *J. chem. Phys.*, **112**, 1907–1916.
[109] Asplund, M. C., Zanni, M. T., and Hochstrasser, R. M., 2000, *Proc. Natl Acad. Sci. USA*, **97**, 8219–8224.
[110] Zanni, M. T., Gnanakaran, S., Stenger, J., and Hochstrasser, R. M., 2001, *J. phys. Chem.* B, **105**, 6520–6535.
[111] Levenson, M. D., and Kano, S. S., 1988, *Introduction to Nonlinear Spectroscopy* (New York: Academic Press).
[112] Tanimura, Y., and Mukamel, S., 1993, *J. chem. Phys.*, **99**, 9496–9511.
[113] Cho, M., Scherer, N. F., Fleming, G. R., and Mukamel, S., 1992, *J. chem. Phys.*, **96**, 5618–5629.
[114] Khidekel, V., and Mukamel, S., 1995, *Chem. Phys. Lett.*, **240**, 304–314.
[115] Khidekel, V., Chernyak, V., and Mukamel, S., 1996, *J. chem. Phys.*, **105**, 8543–8555.
[116] Chernyak, V., and Mukamel, S., 1998, *J. chem. Phys.*, **108**, 5812–5825.
[117] Okumura, K., and Tanimura, Y., 1997, *J. chem. Phys.*, **106**, 1687–1698.
[118] Scheurer, C., Piryatinski, A., and Mukamel, S., 2001, *J. Am. Chem. Soc.*, **123**, 3114–3124.
[119] Tanimura, Y., and Okumura, K., 1997, *J. chem. Phys.*, **106**, 2078–2095.
[120] Okumura, K., and Tanimura, Y., 1997, *J. chem. Phys.*, **107**, 2267–2283.
[121] Cho, M., Okumura, K., and Tanimura, Y., 1998, *J. chem. Phys.*, **108**, 1326–1334.
[122] Okumura, K., Tokmakoff, A., and Tanimiura, Y. 1999, *J. chem. Phys.*, **111**, 492–503.
[123] Cho, M., 1998, *J. chem. Phys.*, **109**, 5327–5337.
[124] Cho, M., 1999, Two dimensional vibrational spectroscopy, in *Advances in Multi-Photon Processes and Spectroscopy*, 1st edn, Vol. 12, edited by S. H. Lin, A. A. Villaeys and Y. Fujimura (Singapore: World Scientific), pp. 1–72.
[125] Cho, M., Blank, D. A., Sung, J., Park, K., Hahn, S., and Fleming, G. R., 2000, *J. chem. Phys.*, **112**, 2082.
[126] Park, K., and Cho, M., 1998, *J. chem. Phys.*, **109**, 10559–10569.
[127] Cho, M., 1999, *J. chem. Phys.*, **111**, 10587–10594.
[128] Cho, M., 2000, *Phys. Rev.* A, **61**, 23406–23417.
[129] Cho, M., 2000, *J. chem. Phys.*, **112**, 9002–9014.
[130] Hahn, S., Park, K., and Cho, M., 1999, *J. chem. Phys.*, **111**, 4121–4130.
[131] Park, K., Cho, M., Hahn, S., and Kim, D., 1999, *J. chem. Phys.*, **111**, 4131–4139.
[132] Cho, M., 1999, *J. chem. Phys.*, **111**, 4140–4147.
[133] Hahn, S., Kwak, K., and Cho, M., 2000, *J. chem. Phys.*, **112**, 4553–4556.

[134] Cho, M., 2000, *J. chem. Phys.*, **112**, 9978–9985.
[135] Park, K., and Cho, M., 2000, *J. chem. Phys.*, **112**, 10496–10509.
[136] Park, K., and Cho, M., 2000, *J. chem. Phys.*, **112**, 5021–5036.
[137] Mukamel, S., 2000, *Annu. Rev. phys. Chem.*, **51**, 691–729.
[138] Stuart, B. C., Feit, M. D., Rubenchik, A. M., Shore, B. W., and Perry, M. D., 1995, *Phys. Rev. Lett.*, **74**, 2248–2251.
[139] Demtroder, W., 1981, *Laser Spectroscopy*, 1st edn (Berlin: Springer).
[140] Maker, P. D., and Terhune, R. W., 1965, *Phys. Rev.*, **137**, A801.
[141] Basche, T., Moerner, W. E., Orrit, M., and Talon, H., 1992, *Phys. Rev. Lett.*, **69**, 1516.
[142] Wright, J. C., 1981, Nonlinear optics, in *Lasers in Chemical Analysis*, 1st edn, edited by G. M. Hieftje, J. C. Travis and F. E. Lytle (Clifton, NJ: Humana), pp. 77–90.
[143] Besemann, D. M., Condon, N. J., Murdock, K. M., Meyer, K. A., Zhao, W., and Wright, J. C., 2001, *Chem. Phys.*, **266**, 177.
[144] Druet, S., and Taran, J. P., 1979, Coherent anti-Stokes Raman spectroscopy, in *Chemical and Biochemical Applications of Lasers*, 1st edn, Vol. IV, edited by C. B. Moore (New York: Academic), pp. 187–252.
[145] Druet, S. A. J., Taran, J. P. E., and Borde, C. J., 1979, *J. Physique*, **40**, 819–840.
[146] Lee, D., and Albrecht, A. C., 1985, *Advances in Infrared and Raman Spectroscopy*, 1st edn, Vol. 12 (Chichester: Wiley-Heyden).
[147] Murdoch, K. M., Thompson, D. E., Meyer, K. A., and Wright, J. E., 2000, *Appl. Spectrosc.*, **54**, 1495.
[148] Thompson, D. E., and Wright, J. C., 2000, *J. phys. Chem.* A, **104**, 11282–11289.
[149] Scholten, T. A. H. M., Lucassen , G. W., Koelewijn, E., de Mul, F. F. M., and Greve, J., 1989, *J. Raman Spectrosc.*, **20**, 503–516.
[150] Levenson, M. D., and Easley, G. L., 1979, *Appl. Phys.*, **19**, 1–17.
[151] Scherer, N. F., Carlson, R. J., Matro, A., Du, M., Ruggiero, A. J., Romero-Rochin, V., Cina, J. A., Fleming, G. R., and Rice, S. A.,1991, *J. chem. Phys.*, **95**, 1487–1511.
[152] Vohringer, P., and Scherer, N. F., 1995, *J. phys. Chem.*, **99**, 2684–2695.
[153] Chang, X. J., Cong, P., and Simon, J. D., 1995, *J. phys. Chem.*, **99**, 7857–7859.
[154] de Boiji, W. P., Pshenichnikov, M. S., and Wiersma, D. A., 1995, *Chem. Phys. Lett.*, **238**, 1–8.
[155] Matsuo, S., and Tahara, T., 1997, *Chem. Phys. Lett.*, **265,** 636–642.
[156] Tokmakoff, A., Lang, M. J., Larsen, D. S., and Fleming, G. R., 1997, *Chem. Phys. Lett.*, **272**, 48–54.
[157] Golonzka, O., Demirdoven, N., Khalil, M., and Tokmakoff, A., 2000, *J. chem. Phys.*, **113**, 9893–9896.
[158] Golonzka, O., Khalil, M., Demirdoven, N., and Tokmakoff, A., 2001, *Phys. Rev. Lett.*, **86**, 2154–2157.
[159] Albrecht, A. W., Hybl, J. D., Gallagher Faeder, S. M., and Jonas, D. M., 1999, *J. chem. Phys.*, **111**, 10934–10956.
[160] Gallagher Faeder, S. M., and Jonas, D. M., 2000, *Phys. Rev.* A, **62,** 033820-1-033820-17.
[161] Bonn, M., Hess, C., Miners, J. H., Heinz, T. F., Bakker, H. J., and Cho, M., 2001, *Phys. Rev. Lett.*, **86**, 1566–1569.
[162] Dick, B., and Hochstrasser, R. M., 1984, *Chem. Phys.*, **91**, 1–11.
[163] Dick, B., and Hochstrasser, R. M., 1983, *Chem. Phys.*, **75**, 133–155.
[164] Dick, B., and Hochstrasser, R. M., 1983, *J. chem. Phys.*, **78**, 3398–3409.
[165] Maechling, C. R., Llimer, D. A. V., and Klenerman, D., 1993, *Appl. Spectrosc.*, **47**, 167–172.
[166] Herzberg, G., 1945, *Molecular Spectra and Molecular Structure. II. Infrared and Raman Spectra of Polyatomic Molecules*, 1st edn (New York: Van Nostrand Reinhold).
[167] Ouellette, F., and Denariez-Roberge, M. M., 1982, *Can. J. Phys.*, **60**, 1477–1483.
[168] Oudar, J. L., and Shen, Y. R., 1980, *Phys. Rev.* A, **22**, 1141.
[169] Barad, Y., Eisenberg, H., Horowitz, M., and Silberberg, Y., 1997, *Appl. Phys. Lett.*, **70**, 922–924.

[170] Denk, W., Strickler, J. H., and Webb, W. W., 1990, *Science*, **248**, 73–77.
[171] Xu, C., Zipfel, W., Shear, J. B., Williams, R. M., and Wwbb, W. W., 1996, *Proc. Natl. Acad. Sci., USA*,**93**, 10763–10768.
[172] Xu, C., Shear, J. B., and Webb, W. W., 1997, *Anal. Chem.*, **69**, 1285–1287.
[173] Tolles, W. M., Nibler, J. W., McDonald, J. R., and Harvey, A. B., 1977, *Appl. Spectrosc.*, **31**, 253–271.
[174] Maier, M., 1976, *Appl. Phys.*, **11**, 209–231.
[175] Lozovoy, V. M., Pastirk, I., Brown, E. J., Grimberg, B. I., and Dantus, M., 2000, *Int. Rev. Phys. Chem.*, **19**, 531–552.
[176] Jordanides, X. J., Lang, M. J., Song, X., and Fleming, G. R., 1999, *J. phys. Chem.* B, **103**, 7995–8005.
[177] De Silvestri, S., Weiner, A. M., Fujimoto, J. G., and Ippen, E. P., 1984, *Chem. Phys. Lett.*, **112**, 195–199.
[178] de Boeji, W. P., Pshenichnikov, M. S., and Wiersma, D. A., 1996, *J. phys. Chem.*, **100**, 11806–11823.
[179] Joo, T., Jia, T., and Fleming, G. R., 1995, *J. chem. Phys.*, **102**, 4063–4068.
[180] Joo, T., Jia, Y., Yu, J. Y., Lang, M. J., and Fleming, G. R., 1996, *J. chem. Phys.*, **104**, 6089–6108.
[181] Larsen, D. S., Ohta, K., and Fleming, G. R., 1999, *J. chem. Phys.*, **111**, 8970–8979.
[182] Everitt, K. F., and Skinner, J. L., 2001, *J. chem. Phys.*, **114**, 1326–1335.
[183] Sanders, J. K. M., and Hunter, B. K., 1994, *Modern NMR Spectroscopy*, 2nd edn (Oxford: Oxford University Press).
[184] Friebolin, H., 1998, *Basic One and Two Dimensional NMR Spectroscopy*, 3rd edn (Weinheim: Wiley-VCH).
[185] Rahman, A., 1989, *One and Two Dimensional NMR Spectroscopy* (Amsterdam: Elsevier).
[186] Orlowski, T. E., and Zewail, A. H., 1979, *J. chem. Phys.*, **70**, 1390–1426.
[187] Warren, W., and Zewail, A. H., 1983, *J. chem. Phys.*, **78**, 2279–2297.
[188] Hamm, P., Lim, M., and Hochstrasser, R. M., 1998, *J. phys. Chem.* B, **102**, 6123–6138.
[189] Tokmakoff, A., and Fayer, M. D., 1995, *Acc. chem. Res.*, **28**, 437–445.
[190] Rector, K. D., Zimdars, D., and Fayer, M. D., 1998, *J. chem. Phys.*, **109**, 5455–5465.
[191] Khalil, M., Demirdoven, N., Golonzka, O., Fecko, C. J., and Tokmakoff, A., 2000, *J. phys. Chem.* A, **104**, 5711–5715.
[192] Asplund, M. C., Lim, M., and Hochstrasser, R. M., 2000, *Chem. Phys. Lett.*, **323**, 269–277.
[193] Golonzka, O., Demirdoven, N., Khalil, M., and Tokmakoff, A., 2000, *Chem. Phys.*, **113**, 9893–9896.
[194] Khalil, M., and Tokmakoff, A., 2001, *Chem. Phys.*, **266**, 213–230.
[195] Tokmakoff, A., 2000, *J. phys. Chem.* A, **104**, 4247–4255.
[196] LaBuda, M. J., and Wright, J. C., 1998, *Chem. Phys. Lett.*, **290**, 29–35.
[197] Prior, Y., Bogdan, A. R., Dagenais, M., and Bloembergen, N., 1981, *Phys. Rev. Lett.*, **46**, 111–114.
[198] Carlson, R. J., and Wright, J. C., 1987, *Chem. Phys. Lett.*, **140**, 101–107.
[199] Levenson, M. D., and Bloembergen, N., 1974, *J. chem. Phys.*, **60**, 1323–1327.
[200] Levenson, M. D., and Bloembergen, N., 1974, *Phys. Rev.* B, **10**, 4447–4463.
[201] Murdoch, K. M., Condon, N. J., Zhao, W., Besemann, D. M., Meyer, K. A., and Wright, J. C., 2001, *Chem. Phys. Lett.*, **335**, 349.
[202] Meyer, K. A., and Wright, J. C., 2001, *Anal. Chem.*, **73**, 5020–5025.
[203] Ulness, D. J., Kirkwood, J. C., and Albrecht, A. C., 1998, *J. chem. Phys.*, **108**, 3897–3902.
[204] Tominaga, K., and Yoshihara, K., 1995, *Phys. Rev. Lett.*, **74**, 3061–3064.
[205] Steffen, T., Fourkas, J. T., and Duppen, K., 1996, *J. chem. Phys.*, **105**, 7364–7382.
[206] Steffen, T., and Duppen, K., 1997, *Chem. Phys. Lett.*, **27**, 47–54.
[207] Steffen, T., and Duppen, K., 1997, *J. chem. Phys.*, **106**, 3854–3864.
[208] Jansen, T. I. C., Snijders, J. G., and Duppen, K., 2000, *J. chem. Phys.*, **113**, 307.
[209] Tannor, D. J., and Rice, S. A., 1985, *J. chem. Phys.*, **83**, 5013–5018.

[210] Tannor, D. J., and Rice, S. A., 1988, *Adv. chem. Phys.*, **70**, 441–523.
[211] Judson, R. S., and Rabitz, H., 1992, *Phys. Rev. Lett.*, **68**, 1500–1503.
[212] Rabitz, H., de Vivie, R., Motzkus, M., and Kompa, K., 2000, *Science*, **288**, 824–828.
[213] Levis, R. J., Menkir, G. M., and Rabitz, H., 2001, *Science*, **292**, 709–713.
[214] Brown, E. J., Pastirk, I., Grimberg, B. I., Lozovoy, V. V., and Dantus, M., 1999, *J. chem. Phys.*, **111**, 3779–3782.
[215] Pinkas, I., Knopp, G., and Prior, Y., 2001, *J. chem. Phys.*, **115**, 236–244.
[216] Kotting, C., Diau, E. W.-G., Baldwin, J. E., and Zewail, A. H., 2001, *J. phys. Chem.* A, **105**, 1677–1682.
[217] Zewail, A. H., 2000, *J. phys. Chem.* A, **104**, 5660–5694.
[218] Zadoyan, R., Kohen, D., Lidar, D. A., and Apkarian, V. A., 2001, *Chem. Phys.*, **266**, 323–351.
[219] Schmitt, M., Knopp, G., Materny, A., and Kiefer, W., 1998, *J. phys. Chem.* A, **102**, 4059–4065.
[220] Materny, A., Chen, T., Vierheilig, A., and Kiefer, W., 2001, *J. Raman Spectrosc.*, **32**, 424–445.
[221] Treado, P. J., and Morris, J. D., 1994, *Appl. Spectrosc. Rev.*, **29**, 1–38.
[222] Schaeberle, M. D., Morris, H. R., Turner, J. F., and Treado, P. J., 1999, *Anal. Chem.*, **71**, 175A–181A.
[223] Volkmer, A., Cheng, J. X., and Xie, X. S., 2001, *Phys. Rev. Lett.*, **87**, 3901–3904.
[224] Duncan, M. D., Reintjes, J., and Manuccia, T. J., 1982, *Opt. Lett.*, **7**, 350–352.
[225] Sanchez, E. J., Novotny, L., and Xie, X. S., 1999, *Phys. Rev. Lett.*, **82**, 4014–4017.